Optimisation of High Yield Steel Coil Processing Characteristics

By

Benjamin Valentine

Submitted to Swansea University in fulfilment of the requirements for the Degree of Master of Science by Research

Faculty of Science and Engineering

Swansea University

Swansea University
Prifysgol Abertawe

June 2021

Abstract

Ribbed steel for the reinforcement of concrete has a characteristic high yield strength of at least 500 N/mm^2, bonds well to concrete, and is ductile. Reinforcing steel is produced at *Celsa Steel UK* in coils approximately 1.5 km in length, which are post processed by customers to create reinforcement structures used in construction projects. Post processing involves straightening and bending to make complex shapes, so consistent steel properties are required for high rates of production. Variations in the properties of a two-tonne coil can be caused during the manufacturing process and effect post processing as customers' machines need frequent adjustments to shape the steel into the correct dimensions. When the coil needs too much adjustment, the coil is scrapped. This thesis identifies and evaluates the key properties effecting reinforcing steel post processing, then discusses the manufacturing processes that could be improved to better control the consistency of these properties.

Through analysis of *Celsa Steel UK*'s historical data on yield strength in coils, it was found that sections of steel on the external layers of coils have up to 95 MPa greater yield strength than steel in the core of the coil. Increased cooling rate on the outside of the coil, compared to the core, is suggested to cause this variation.

Scanning electron microscopy techniques were used to compare grain size, microstructure, composition, and texture between steel samples collected from customers of *Celsa Steel UK*. Samples that were rejected by customers were compared with samples that behaved consistently. Microstructure and composition were relatively consistent between all samples while grain size varied between 3 µm and 5 µm. This grain size variation is likely to be related to varying cooling rates. Texture was relatively randomised in all samples, and many showed a slight preference in the <110> orientation, indicating a weak rolling texture.

As there were no significant differences in the above microstructural properties, an FEA Ansys model was constructed to investigate the effect of cross-sectional consistency on the bending behaviour during customer post processing. Simulations of bending a 12mm reinforcing steel bar with 0.8mm variation in perpendicular cross-sectional diameters showed 1.46 mm out of plane deflection, 100 mm from bend. For a 500 mm by 500 mm square, this out of plane behaviour would deform the shape by 73 mm perpendicular to the intended plane, similar to that seen by customers.

Acknowledgements

I would like to thank M2A for giving me the opportunity to study and research for this qualification and the teaching and support they have given me throughout. I would also like to thank my tutor Dr Mark Coleman for supporting me throughout my research, guiding my progress, and training me on the required equipment.

I would also like to thank *Celsa Steel UK* for letting me work on this project, meet with various specialists, and visit their steel factory in Cardiff. I would like to thank Express Reinforcements for allowing me to visit their processing site in Neath. I would like to thank Stuart Thomas at *Celsa Steel UK* for his guidance and experience. Finally, I would like to thank Scott Kennedy and Kevin Lloyd for providing support as well as supplying samples and historical technical reports.

Declaration

This work has not previously been accepted in substance for any degree and is not being concurrently submitted in candidature for any degree.

Signed Benjamin Valentine .... (candidate)

Date 27/09/2021

STATEMENT 1

This thesis is the result of my own investigations, except where otherwise stated.

Other sources are acknowledged by footnotes giving explicit references. A bibliography is appended.

Signed Benjamin Valentine .... (candidate)

Date 27/09/2021

STATEMENT 2

I hereby give consent for my thesis, if accepted, to be available for photocopying and for inter-library loan, and for the title and summary to be made available to outside organisations.

Signed Benjamin Valentine .... (candidate)

Date 27/09/2021

Contents

List of Figures

List of tables

List of Equations

List of Abbreviations

BCC – Body centred cubic

BCT – Body centred tetragonal

BSD - Backscatter diffraction

C - Cross section sample

CSPD – Cross sectional phase distribution

EBSD - Electron backscatter diffraction

ECD - equivalent circle diameter

EDS - Energy dispersive spectroscopy

FCC – Face centred cubic

FEA - Finite element analysis

L - Longitudinal sample

MAD - Mean angular deviation

SE - Secondary Electron

SEM - Scanning electron microscopy

Chapter 1 Introduction

Reinforcing steel, also known as rebar, is used to reinforce concrete structures by increasing the structures' tensile strength. Plain concrete is strong in compression but weak in tension, so combining it with high-tensile strength steel reduces crack formation in the concrete under tensile loads. *Celsa Steel UK* produce a reinforcing steel product named Celsamax and in 8, 10-, 12-, 16-, and 20-mm diameters as both straight lengths and coils. This project focuses on processing issues experienced with the 12 mm diameter product which is produced in coils approximately 1.5 km in length, since this is the most common Celsamax product. Celsamax has a circular core with longitudinal and transverse ribs around this core which improve adhesion to the concrete.

To reinforce structures, processor companies process rebar coils by straightening, bending, and cutting to create shapes that fit the geometry of the structure, such as steel cages, grids, and squares. This processing currently incurs various inconsistencies that increase scrap and production time. Common inconsistencies which have been reported include: the force required to straighten the coil, the amount of coil which is pulled through by drive rollers, and deflection out of the plane intended during deformation (these are described in more detail in chapter 2.3). Adjustments must be made when these characteristics change and often coils which would be processed simultaneously, must be processed individually if they behave differently. This increases production time for customers and coils which require too much adjustment are returned to *Celsa Steel UK*, increasing *Celsa Steel UK*'s costs. Celsa estimate that five percent of the Celsamax they produce is currently scrapped, either by themselves or processor companies, due to processing issues.

1.1 Aims and Objectives

The aim of this thesis is to identify the key parameters that cause post processing inconsistencies for customers. Customers have reported differences in properties along the length of a single coil and between different coils. Chapter 3 investigates the mechanical properties along the length of a single coil. Chapter 4 explores the microstructural differences between samples from rejected coils compared to a nominal coil. Chapter 5 explores the use of a model to simulate the sensitivity of cross-sectional accuracy specifically to the out of plane bending phenomena experienced by customers. By identifying properties in reinforcing steel bar that are influential to customer processing behaviour, the manufacturing stages responsible for variations seen in these properties are suggested and potential improvements are discussed.

Chapter 2 Literature Review

2.1 Steels

Steel is the most widely used material for infrastructure and construction. In 2018, 1,808 million tonnes of crude steel were produced globally and 7.3 million tonnes of this was from the United Kingdom [1]. It is so commonly used because of its unique range of mechanical properties. Steel can be strong, ductile, highly formable, magnetic and a strong conductor of heat and electricity. The raw materials are abundant, and it is relatively cheap to produce, form and process. There are over 3500 grades of steel which all have unique properties, giving steel a wide variety of uses and applications as grades are suitable for different requirements [2].

Steel is an alloy of iron and carbon in which the carbon content is between 0.008 and 2.14%, other alloying materials of various quantities are added to create specific steel grades [3]. Iron is an allotropic element which means it has more than one crystalline form its atoms can be arranged in [4], according to free electron theory [5]. At room temperature, pure iron is a ferrite phase, which has a body-centred cubic lattice (BCC). A BCC has part of one atom in each corner and one in the centre of a cube, as shown in figure 2.2. When heated above 912°C, ferrite undergoes a polymorphic transformation and becomes austenite, a face-centred cubic lattice (FCC). In an FCC unit cell, there is part of an atom in each corner and in the centre of each face, illustrated in figure 2.2. Heating austenite to 1394°C causes the FCC to convert back into a BCC called δ-ferrite which melts when it reaches 1538°C [3]. These phases are indicated by the left side of the iron-iron carbide phase diagram in figure 2.1, where iron is 100% of the composition.

Figure 2.1 shows up to 6.70 wt% C along the x-axis, this composition is iron carbide (Fe_3C), or cementite, at room temperature. Since carbon atoms are 1/30 the size of iron atoms, they fit within iron crystallographic unit cells as an interstitial element [4]. The number of Carbon atoms that can form a solid solution before the iron is saturated depends on the crystal structure. Cementite forms when the solubility limit of Carbon in Ferrite is exceeded, and the temperature is below the Austenitizing temperature.

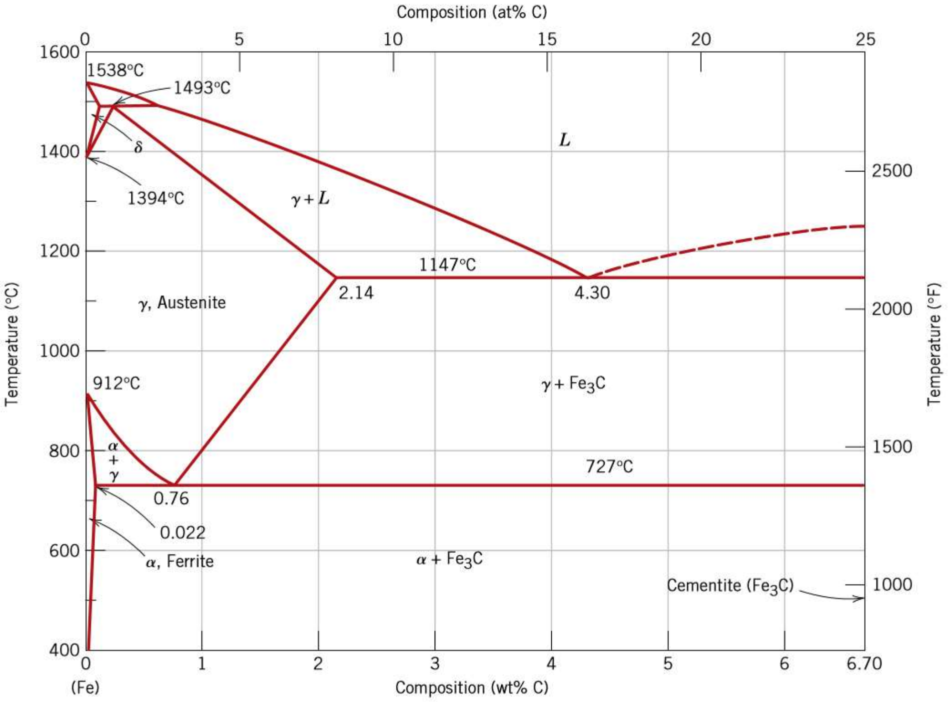

Figure 2.1 Iron - carbon phase diagram (4). Each line represents a phase change which involves a rearrangement of the iron crystal structure.

For an iron-carbon alloy of eutectoid composition (0.76 wt% C), when temperature falls below the eutectoid temperature, the austenite phase transforms into alternating layers (lamellae) of ferrite and cementite phases. This is because the composition of the austenite (0.76 wt% C) is different to ferrite (0.022 wt% C) and cementite (6.70 wt% C) and carbon must be redistributed by diffusion. The transformation begins with the nucleation of either a ferrite or cementite phase. Carbon atoms diffuse away from ferrite regions creating an excess of carbon in neighbouring areas which form cementite. The opposite occurs in cementite regions, carbon atoms diffuse into these areas, leaving the surrounding layers with 0.022 wt% C to transform into ferrite. This diffusion creates layers oriented in the same direction within each grain and this alternating pattern is called pearlite [3,5].

A hypoeutectoid alloy contains between 0.022 and 0.76 wt% C. Cooling an alloy of this composition to just above the eutectoid temperature causes ferrite to form mainly around the austenite grain boundaries. This ferrite has 0.022 wt% C so excess carbon is diffused into the austenite. Ferrite continues to form until the carbon content in the remaining austenite reaches the eutectoid composition, 0.76 wt% C. As temperature drops below the eutectoid temperature, this remaining austenite transforms into pearlite [3].

Hypereutectoid alloys are iron-carbon alloys with between 0.76 and 2.14 wt% C. As these cool below the eutectoid temperature, proeutectoid cementite forms around initial austenite grain boundaries, drawing carbon atoms until the carbon content in the remaining austenite falls to 0.76 wt% C and transforms into pearlite [3].

The microstructures discussed so far all require diffusion. If the steel has insufficient cooling time for diffuse-controlled processes, it transforms to martensite, sometimes with a small percentage of retained austenite [6]. The transformation to martensite involves a spontaneous deformation [7]; nucleation across a grain can occur faster than the speed of sound [6]. Martensite grows across austenite grains and as temperature continues to fall, the remaining austenite is converted into martensite. As the FCC austenite is transformed, it undergoes a polymorphic transformation to a body-centred tetragonal (BCT) martensite. This is a BCC that has been elongated along one of its dimensions [8]. Carbon atoms in rapidly cooled grains remain interstitial elements in martensite as they do not have time to diffuse out of the crystal structure to form cementite. These carbon atoms move to one of the octahedral sites (sublattices) in the ferrite, causing a distortion which converts the BCC into a BCT [9]. So, steel martensite is a supersaturated solid solution of carbon in iron. This strained lattice resists deformation, increasing the steel's strength, a key property for reinforcing steel. The unit cells of ferrite, austenite, and martensite steel are shown in figure 2.2.

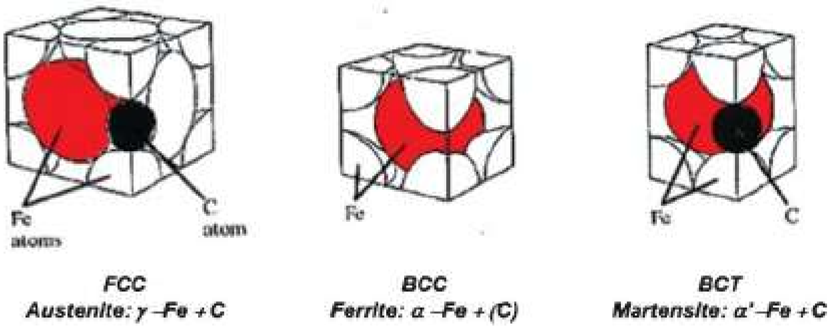

Figure 2.2 Unit Cell Crystallographic Structures of Austenite (Left), Ferrite (middle) and Martensite (right) with the position of a carbon atom shown. In the ferrite phase, only 0.022 wt% C is soluble [8].

2.2 Reinforcing Steel

Reinforcing Steel (rebar) is used in the construction industry for reinforcing concrete structures. It is used in a concrete matrix to provide strength. While concrete is strong in compression, steel is strong in both compression and tension, so it enables structures to resist larger bending and deformation forces than concrete alone [10]. Due to the increased strength, rebar allows more complex shapes and taller structures that need less support material. Ductility is also increased in comparison to non-reinforced concrete. This means structures give visible signs of failure prior to complete failure, which is an important safety feature that allows time for evacuation or repair work before a structure could collapse.

A key design requirement of rebar is high yield strength to resist deformation and provide support to the structure. The British Standard for steel for reinforcement of concrete is BS4449 and it states that the minimum acceptable yield strength is 500 MPa [11]. Another important requirement is ductility. Rebar is often bent into various shapes to be used in different concrete forms and so requires ductility to bend without cracking. BS4449 specifies the tensile to yield strength ratio for different grades of reinforcing steel, these ratios range from 1.05 to 1.35 [12]. Further properties which are specified for rebar include fatigue strength, recyclability, corrosion resistance when submerged in concrete, formability, bond to concrete and uniform properties for accurate processing [13–15].

Reinforcing steel is usually a High Strength Low Alloyed (HSLA) steel as this is relatively low-cost and can provide the required strength [16]. These can contain alloying elements with a combined concentration of up to 10 wt% and are ductile, formable and machinable [3]. HSLA steels are also more resistant to corrosion than plain carbon steels. Dual phase steel is a high strength steel that contains a ductile ferrite core and a hard martensite outer shell which usually makes up about 20% of the volume [13]. This gives the steel both the required strength and ductility properties. The graph produced by Stewart et al. shown in Figure 2.3, illustrates the difference between strength and ductility of ferrite and martensite [17]. Martensite has much greater yield strength and UTS, but less ductility, compared to ferrite. By combining specific fractions of each phase, desired properties can be achieved. This microstructure is normally produced through heat treatment. Steel can be heated to the intercritical region, where nucleation transforms some of the ferrite into austenite. Next, rapid cooling occurs and does not allow time for diffusion led phase transformations, so the austenite transforms into martensite, instead of ferrite. Rapid cooling is achieved by quenching the outer surface of the steel, so martensite forms at the edge while the core cools more slowly and produces a mixture of ferrite and pearlite [14].

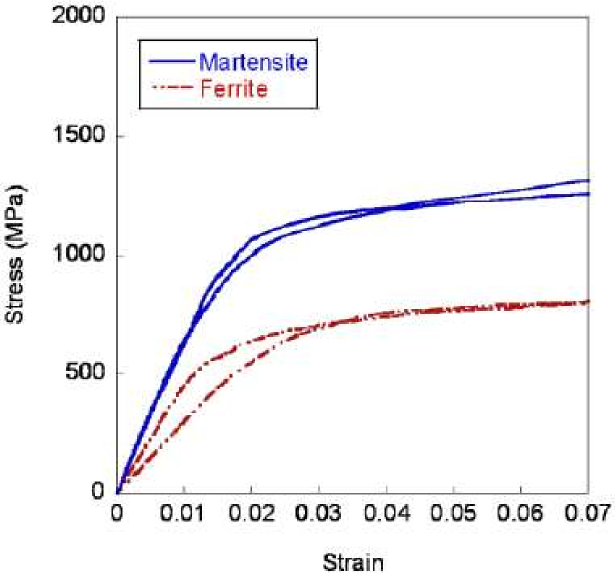

Figure 2.3 Graph showing stress-strain curves for two samples of Martensite and Ferrite produced by Stewart et al. (17). The martensite samples have approximately twice the yield strength and UTS of the ferrite samples.

The core of rebar is usually a mixture of pearlite and ferrite, the volume fraction of each phase depends on carbon content. This proportion of ferrite and pearlite in the core can also affect the properties since both phases have different strength values. Figure 2.4 shows the work of Iacoveillo et al. in producing a stress-strain plot for different fractions of ferrite and pearlite in ductile cast iron [18]. It shows pearlite with a yield stress of approximately 750 MPa, which is more than double the yield stress of ferrite, 350 MPa, and combinations of the two phases give strength values between these two values.

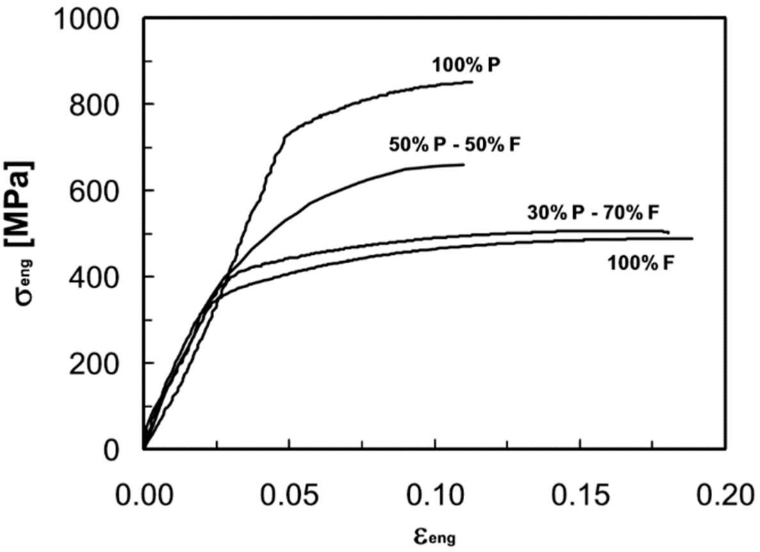

Figure 2.4 Graph showing the influence of ferrite and pearlite phase fraction on tensile test results for a study by Iacoveillo et al. (18). Increasing the proportion of pearlite increased the tensile strength for the steel in the study.

Most reinforcing steel is produced in either a large coil or straight sections which require bending by the customer to produce specific shapes for buildings such as grids and squares. Bending can lead to cracking since the steel is high strength and the ribbed surface acts as a stress raiser. To avoid this, bends have a minimum radius depending on diameter, specified in BS4449 [11]. Factors that affect the risk of cracking include strain ageing and temperature, since embrittlement occurs when temperature decreases. Therefore, bending should not occur at a temperature below the ductile to brittle transition temperature. Kabir et al. found that a 0.27 wt% C rebar which was quenched and self-tempered had a ductile to brittle transition temperature of 5°C [19]. Since Celsamax is a quenched and self-tempered rebar with 0.24 wt% C, it is likely to have a similar transition temperature. The major factors that affect bending performance are the mechanical characteristics and the bar profile. Consistent bar shape is required for consistent bending performance [12].

The surface of modern reinforcing steel bar produced by *Celsa Steel UK*, shown in figure 2.4, contains four longitudinal straight ribs which are connected by diagonal transverse ribs [20]. The main purpose of the ribs is to create a secure bond with concrete. Rib height from the core is specified as well as the bar diameter in multiple directions. These measurements are specified to ensure the profile is uniform and the required bending force is the same in every direction.

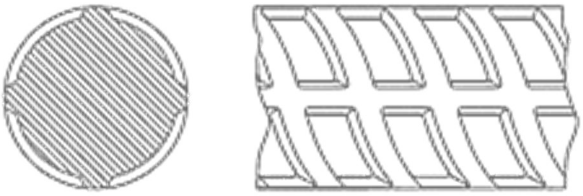

Figure 2.5 Diagram of the cross-section (left) and longitude (right) planes of Celsamax rebar (19). Four longitudinal ribs can be seen around the cross section and three of these are visible in the longitude plane, in a horizontal direction at the top, middle, and bottom. Transverse ribs are diagonal across the longitudinal surface.

2.3 Applications of Reinforcing Steel

Reinforcing Steel is used to increase the strength of concrete structures. The steel is processed by bending, straightening, and welding to create shapes that fit a specific structure. Processing is completed by machines operated by factory workers. Automatic link benders (ALBs) are used to straighten, bend, and cut reinforcing steel coils to create individual shapes. These shapes can be programmed to be automatically measured, bent, and cut.

There are a variety of machines designed for processing rebar, this project focuses on the widely used Automatic Link Bender (ALB), shown in figure 2.6. One or two (twin strand) steel coils can be loaded onto reels and drawn through the machine by a pair of toothed drive rollers. The bar is then straightened under eight high-pressure, smooth rollers before extending passed a bending pin to the required length. The bending pin rotates by a specified angle to create a bend before returning to its original position. Then, the bar is either pulled through further to be bent again, or a shearing blade cuts off the bent section to create a finished part. This can create most two-dimensional shapes which can then be welded together to create larger structures.

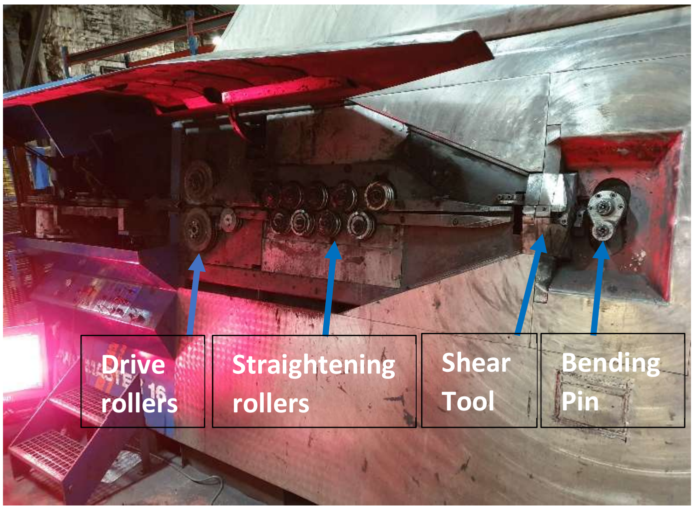

Figure 2.6 ALB machine with the cover raised, showing the drive roller pair, a set of straightening rollers, bending pin, and shearing tool. Rebar enters the machine from the left and the finished product will drop to the right of the image after shearing.

An operator is required to set up new coils, monitor operation and calibrate processing machines. The machine must be calibrated because the steel does not always perform consistently so adjustments must be made to the roller pressure, amount of compensation for spring back, and distance the steel is drawn through the rollers. There are several limitations and issues in the operation of ALBs which may be caused by variations in the steel coil. These include out of plane bending, differences between lengths in twin strand parts, and lengths which under- or over- straighten.

Out of plane bending refers to a bending case where a bar bent in an XY plane deforms in the Z axis, as shown in figure 2.7. This creates a part that is not flat, and the effect is compounded if multiple bends are made that all exhibit this effect. This part may require manual bending to flatten the part or could be deemed unusable. Production is slowed down as operators try to reduce the out of plane effect, and waste increases as unsatisfactory parts must be scrapped. The problem can occur throughout a whole coil or just a section of it. The cause of out of plane bending is unknown and has not been thoroughly researched. Operators and manufacturers have predicted various possible causes which relate to either the processing of the steel coil or variations in the steel properties.

Figure 2.7 Image of an In-plane (Left) and Out-of-plane (right) Rebar Structure. Both parts should be identical flat squares but the out of plane part bends upwards and is unusable. This is an extreme example and out of plane deformation is not usually this significant.

A common issue experienced with twin strand processing machines is differences in behaviour between the two strands. Twin strand processing feeds two coils through a processing machine simultaneously to produce two parts at once, doubling the production rate. Differences are sometimes experienced between these two coils which causes the pair of parts produced together to have different dimensions. Most frequently, one coil produces longer lengths than the other when they are pulled through by the drive rollers, as shown in figure 2.8. This means one coil produces parts with larger dimensions than the other. If the difference in dimensions is too large, one or both parts must be scrapped. Often, processors remove one of the coils from the machine when this occurs, thus halving the production rate. The cause of differences in twin strand processing are not well understood. Possible causes could be due to differences in the contact and slip with the drive rollers due to differences in dimensions or mechanical properties between the two coils.

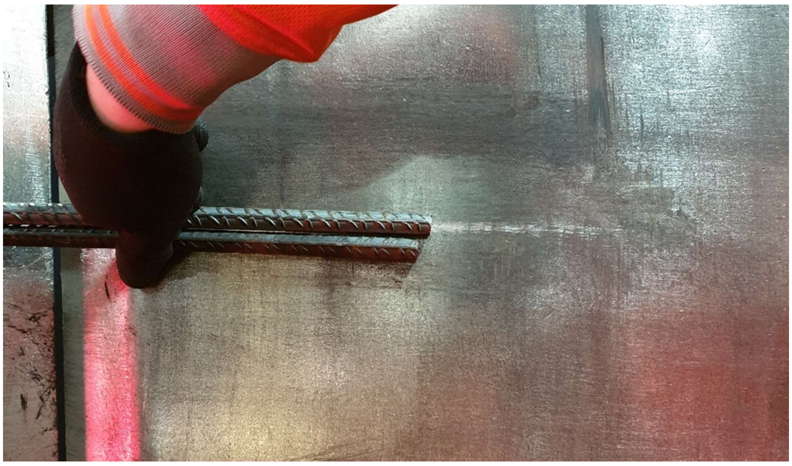

Figure 2.8 Example of a common twin strand issue where one coil is pulled through the ALB drive rollers further than the other coil. Here the difference is approximately 10 mm, but greater differences occur and the difference increases as the bars are pulled through further. This produces two parts with different dimensions, one of which will not meet the design specification.

Further issues are experienced when straightening rebar. The rebar will often over- or under-straighten, as the rebar retains some of the curvature from its coil. This can be compensated for by adjusting the pressure exerted by the straightening rollers. The main challenge is if there are differences in the roller pressure required by two coils being processed in twin strand, as shown in figure 2.9, they will not both be straightened simultaneously. In this case, the coils must be processed individually, thus doubling the production time.

Figure 2.9 Differences in straightening of rebar during twin strand ALB processing. Both rebar coils are under straightened and need adjustment to produce straight lengths. However, one coil is less straight than the other so they each require a different amount of force to straighten and cannot be processed simultaneously.

Consistent steel coil processing relies on maintaining certain variables independent of the coil properties. Variables which are considered important to control are temperature, tension in the steel, roller pressure and machine setup. Since steel becomes more brittle at low temperatures, rebar should not processed below the ductile to brittle transition temperature. Processing occurs at ambient air temperature, but rebar could fracture if deformed in cold weather conditions, close to 0°C. Tension is applied to the steel since the two tonne coil resists being unwound and the drive rollers provide a force to overcome this. The tension could influence the response to straightening and bending as steel that is already under tension will plastically deform more easily. The amount of tension can vary depending on how the coil has been positioned and how much steel is left on the coil. Towards the end of the coil, there is much less resistance to movement and thus, less tension. Additionally, roller pressure effects straightening behaviour. Too little pressure does not straighten the bar enough, too much causes the bar to curve in the opposite direction. Roller pressure can often be adjusted by operators if straightening and bending is not working as expected but this is not necessarily the correct solution. It is possible that other errors made during the setup of an ALB machine are the cause of inconsistent results.

2.3.1 Possible causes of processing Issues

Variations in steel coil properties that may cause adverse bending include the dimensions, mechanical properties, microstructure, and chemical composition. These properties have previously been studied by *Celsa Steel UK* for their product, Celsamax B500C Reinforcing steel, but the properties' influence on bending behaviour is not well understood.

Dimensional variation can include difference in thickness, which changes the amount of force required to straighten or achieve a specific bend angle. Also, the cross section can be elliptical, rather than circular, and this could cause the bar to bend in the thinnest orientation rather than in the bend plane.

The mechanical properties of the steel directly influence bending and the force required to deform the steel. Variations in the heat treatment process lead to differences in mechanical properties along a reinforcing coil, which could cause processing behaviour to change in different sections of the coil. Microstructure and chemical composition influence the mechanical properties so changes in these will also effect bending. These variations could be between different casting batches, or inconsistencies within a coil through uncontrolled variables in manufacturing.

A variation in reinforcing steel microstructure that has been previously researched is the martensite layer. If quenchant flow is not consistent and even around the bar, it could cause the layer of martensite to be thicker in certain areas than others. Pantazopoulos et al. identified presence of a non-circular ferrite – pearlite core in a rebar sample which had prematurely failed during fatigue testing [21]. The quenched edge region of the sample varied in thickness between 0.9 – 1.0 mm, making the core non-circular. The non-circular core was not attributed to the fatigue failure, but it could influence bending behaviour. The thinner areas of quenched region would make certain orientations softer and could cause bending to occur preferentially in the directions where the bar is softer.

Twist in the steel coil created during rolling is another potential cause of out of plane bending and misshaped structures, such as figure 2.10. During coiling, the steel bar is wrapped around a spool at approximately 450 – 600°C. This can be visible in finished coils as the coil layers are not all in the same orientation. If a twisted section is bent during processing, it may cause the bent end to move in the direction of twist, creating an out of plane bend. Twist could be caused by a change in force required to bend the bar around the spool. If twist does cause out of plane bending, the causes of the twist would need to be identified. These are likely to be similar to the other proposed causes of out of plane bending. Like out of plane bending, more easily deformed areas will bend preferentially so the bar may rotate until softer sections face inwards during coiling.

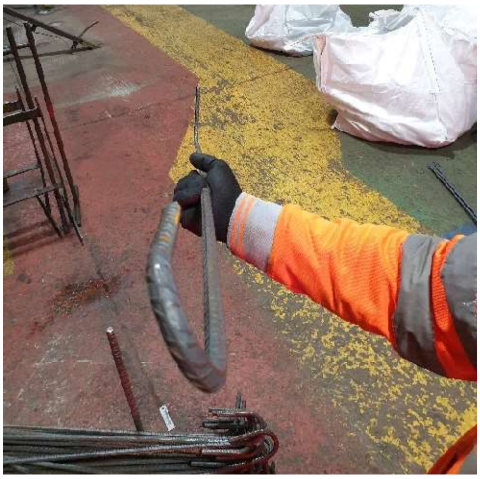

Figure 2.10 Image of a Twisted Rebar Part produced by Express Reinforcements. Twist is visible as the bends at either end are in different orientations, the near end is twisted to the left while the far end is twisted to the right. The twist could have existed in the bar prior to bending or it may have occurred during bending.

2.4 Microstructure of reinforcing Steel

2.4.1 Reinforcing Steel Grains

Within a grain, the arrangement of atoms is nearly identical. In contrast, the arrangements of atoms in separate grains of the same phase are also close to identical, but they are orientated differently. The grain boundary is a narrow space where adjoining grains are not aligned. These boundaries affect the material properties by impeding dislocations.

Grain boundaries can be either high- or low-angle boundaries. A low angle boundary is between two adjoining grains with misorientation that is small enough to allow dislocations to slip across the boundary. A high angle boundary is between adjoining grains with an abrupt change in orientation which is large enough to stop or restrict dislocation movement [22].

A fine grain material is harder and stronger than one with coarse grains since it has more grain boundaries to impede dislocation growth, The Hall-Petch relation, shown in Eq.2.1, gives the yield strength according to grain size for many materials [3].

$$\sigma_y = \sigma_0 + k_y d^{-\frac{1}{2}} \qquad \text{Eq.2.1}$$

In this expression, σ_y is the yield strength, d is the average grain diameter, σ_0 is the lattice friction stress, which is the yield stress for a single crystal of the material with no grain boundaries, and k_y is a constant specific to the material. The Hall-Petch relationship is accurate for metals with a grain size between 1 µm and 1 mm. Grain size can be regulated by altering the rate of solidification, addition of grain-refining elements and thermomechanical processing.

Modern rebar is generally made using the quench and self-temper process described in the CARES guide to reinforcing steels [12]. This involves rapidly cooling the surface of the steel with water to form martensite, then removing the water to allow retained heat from the cover to conduct out to the surface, tempering the newly formed martensite. Quenched and self-tempered rebar contains ferrite and pearlite grains in a circular core region, surrounded by a layer of tempered martensite grains. Pantazopoulos et al. identified acicular ferrite and pearlite grains in the core and tempered martensite grains in the edge of B500C rebar [21]. The presence of MnS inclusions was also verified by EDS analysis of the B500C steel [21].

2.4.2 Martensite

Martensite is a very hard steel crystalline structure which forms during rapid cooling of austenite due to quenching. The transformation is diffusionless since it occurs too quickly for carbon to diffuse out of the crystal structure in large enough quantities to form ferrite or pearlite. Since the carbon atoms are retained, the BCC structure deforms into a highly strained BCT structure that is supersaturated with carbon. The deformation of the crystal structure produces many dislocations, which are the main cause for the high strength of martensite.

Martensite forms either as thin plates or laths to minimise the strain energy due to deformation [9]. Laths have a thin needle shape, less than one micron thick. Each lath has a specific crystallographic direction, neighbouring laths are separated by a low boundary angle with misorientation less than five degrees [6,23]. These closely orientated laths form in packets, which are assumed to be the effective grain size [24]. Lath crystals are very fine whereas plate crystals are much larger with large amounts of retained austenite. Lath martensite forms when the carbon content is less than 0.6 wt% [25]. Since BS4449:2005 specifies 0.24 wt% carbon in the reinforcing steel product, lath martensite is expected to form during quenching [11].

Martensite has a start temperature (M_s) where it begins to form and a specific temperature where martensite finishes forming (M_f) although this does not always mean the steel is pure martensite, some retained austenite can remain after temperature falls below M_f. A lower M_s value reduces the volume fraction of martensite (V_M) that can be produced. Increasing carbon content lowers M_s, and hence causes lower V_M. The relationship between M_s temperatures and carbon content on the iron-carbon phase diagram are shown in Figure 2.11. Figure 2.11 also shows the ranges of carbon content which form the two martensite morphologies, lath, and plate [26]. Since there is no diffusion during martensite formation|, the chemical composition of the martensite is identical to that of the prior austenite. The carbon content depends on the nominal content of the base steel [13].

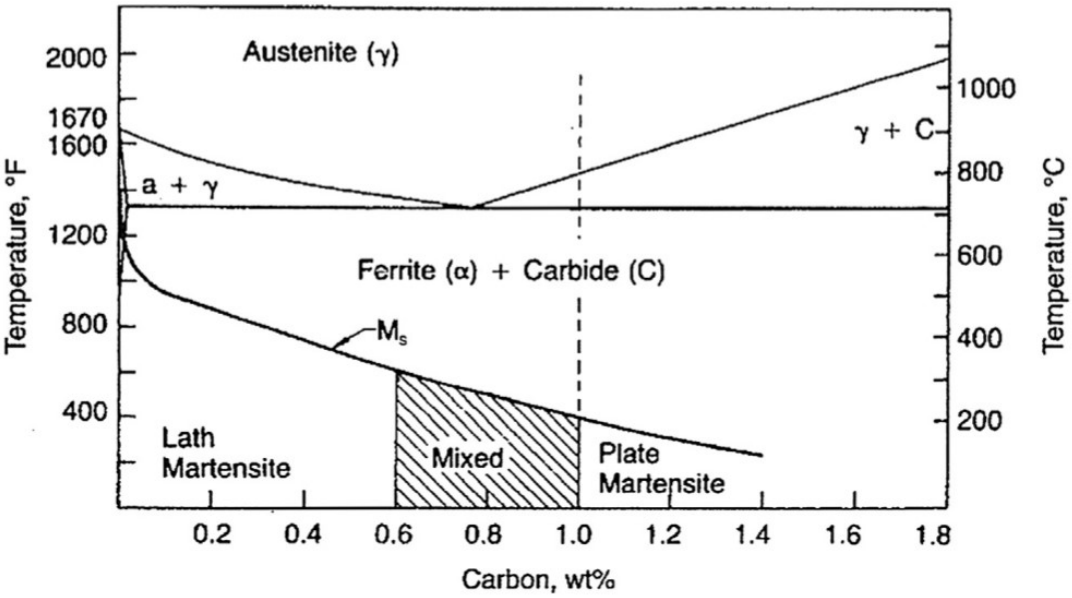

Figure 2.11 Ms temperatures as a function of austenite carbon content, superimposed on the iron-carbon phase diagram (25). Lath martensite forms for steel with carbon content between 0 – 0.6 wt%.

2.4.3 Texture

Crystallographic orientation of a material refers to the orientation in which a crystallographic structure is aligned. In a polycrystalline material, a grain contains a crystallographic structure in one direction. While neighbouring grains of the same phase contain the same crystal structure in a different orientation. In many materials, there are preferred orientations in which a large proportion of grains are aligned. These are caused during crystallization from austenite and subsequently through thermomechanical processes [27]. This preferred orientation is also known as texture. A random distribution of grain orientations with no preferred orientation is known as a randomised texture. The Miller index, illustrated in figure 2.12, is a notation system for describing planes in a crystal lattice [28]. The orientation of these planes in relation to the rolling, transverse, or normal direction of a material is used to describe texture. Texture can significantly affect many physical, mechanical, and electrical properties and can cause anisotropic properties, where a property has different values in different directions of the material. Therefore, texture is a key factor for achieving the desired properties for rebar.

Every stage in the process of producing steel affects the texture, including the composition, rolling and heat treatment. Certain textures are created through deformation. During rolling, grains elongate in the direction of rolling and the [110] orientation, illustrated in figure 2.12, aligns with the rolling direction. Vlad and Bunge, 1981, showed that for dual phase ferrite-martensite steel that is formed by hot rolling prior to quenching, such as the rebar in this study, a wide variety of textures can develop due to compositional effects and thermo-mechanical processes acting in combination [29].

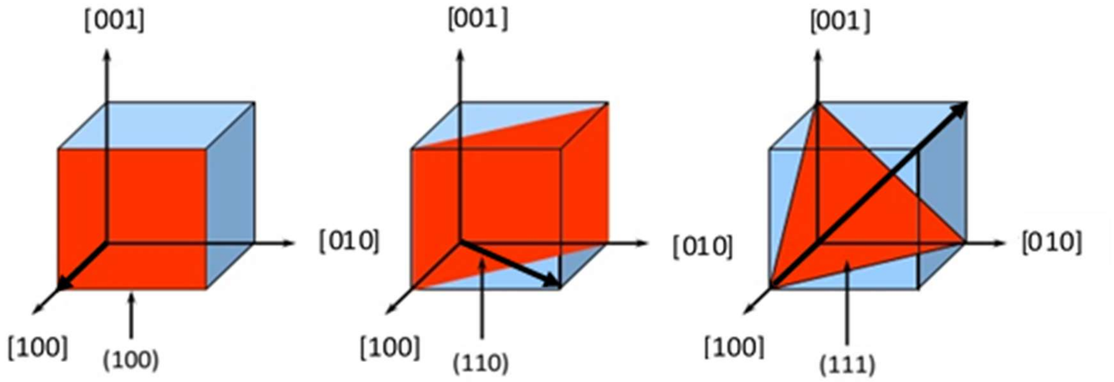

Figure 2.12 Miller indices used to describe crystallographic orientation. Three common planes are shown in red (A) [100] plane, (B) [110] plane, (C) [111] plane [28].

2.4.4 Solid Solution Strengthening

Solid Solution Strengthening involves dissolving alloying elements as a solid solution to increase the strength of a metal. These elements can either occupy interstitial or substitutional sites in the metal's lattice structure. A substitutional atom occupies a space in the lattice that would otherwise contain an atom of the base metal whereas interstitial atoms are positioned in spaces that are normally unoccupied [22]. Interstitial atoms can be swept along dislocations to form greater concentrations of these atoms at dislocations. Whether an element occupies an interstitial or substitutional space depends on its properties according to the Hume-Rothery Rules which are shown below [3]:

1. Atomic size factor. If the difference between the host and alloying atoms size is less than ±15% then it may occupy as a substitutional. If the difference in size is greater, it will be interstitial.
2. Crystal structure. For substitutional solid solubility, an atom must have the same crystal structure as the host element.
3. Electronegativity factor. The solute and solvent should have similar electronegativity for maximum solubility.
4. Valences. A metal of higher valency has greater likelihood of being dissolved by another metal.

The atom of the alloying element distorts the crystal structure and creates a localised strain on the lattice. If the alloy atom is larger, the strain field is compressive and if the alloy atom is smaller, its strain field is tensile. These localised strains are greater when the atom size difference is greater, and a greater concentration of solute atoms leads to a larger strengthening effect. The lattice strain creates a barrier to dislocation movement, and this is how solid solution can strengthen a metal. Greater stress applied to the material is required to force a dislocation to move against a strain field, thus yield strength is greater. As shown in figure 2.13, Carbon and nitrogen are the most powerful strengthening elements because they have a small size and occupy interstitial sites in iron [22]. The other elements included in figure 2.13 are 15% of the size of an iron atom, so they are substitutional and have less effect on yield strength. It can also be seen that increasing the content of these alloys increases the strengthening effect.

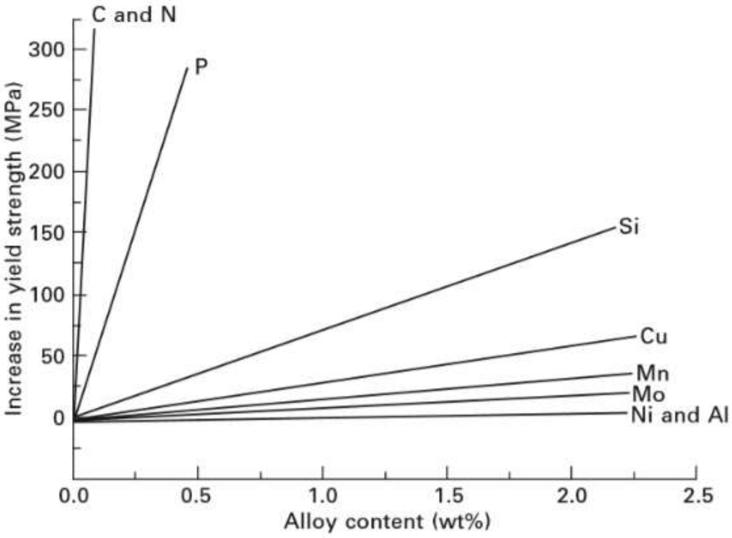

Element	Atomic size (pm)	Size difference (%)
Iron	126	
Carbon (C)	77	–39
Nitrogen (N)	65	–48
Phosphorus (P)	107	–15
Silicon (Si)	111	–12
Manganese (Mn)	127	+1
Molybdenum (Mo)	139	+10
Aluminium (Al)	143	+9
Copper (Cu)	128	+2
Nickel (Ni)	124	–2

Figure 2.13 Effect of various alloying elements on the yield strength of iron by solid solution strengthening, the element's atomic sizes, and their size relative to iron [22]*. The actual effect on yield strength depends on processing parameters and other conditions.*

2.5 Reinforcing Steel composition

Reinforcing steel is generally a low carbon steel with small amounts of alloying elements to achieve the required properties at a low production cost. Recycled steel is the main material that *Celsa Steel UK* use in the production of reinforcing steel and consequently, the quantities of alloying elements in the product can vary. Using scrap steel in steelmaking creates challenges for creating a consistent composition. The source of the scrap is unknown and can contain a myriad of alloying elements and inclusions which were intended for the requirements of the previous use. When the scrap is recycled, these elements are considered residual, or tramp elements, since they haven't been deliberately added to the new steel being produced. Therefore, the composition is monitored and adjusted, when necessary, by adding iron or other materials to refine the steel.

The British standard for reinforcing steel, BS 4449:2005, states the maximum quantities that are accepted in reinforcing steel, as shown in table 2.1. Cast analysis is the composition of the steel melt as it is cast, whereas product analysis refers to the composition of the final product, after rolling and heat treatment. If any of these quantities are exceeded, then the reinforcing steel does not conform to the British standard.

BS4449:2005	Carbon	Sulphur	Phosphorus	Nitrogen	Copper	Carbon Equivalent
Cast Analysis	0.22	0.05	0.05	0.012	0.8	0.5
Product Analysis	0.24	0.055	0.055	0.014	0.85	0.52

Table 2.1 Chemical composition of reinforcing steel alloying elements (maximum percentage by mass) defined by BS4449:2005 [11].

The carbon equivalent component is calculated from the quantities of certain other elements. These elements are less significant but if the accumulation of them exceeds the specified limit, then steel performance may not meet the requirements and thus it does not meet the British Standards. The formula for calculating carbon equivalent is shown is Eq.2.2, where C_{eq} is the carbon equivalent, and the remaining characters are element symbols which represent the mass fraction of the element as a percentage. Since Cr, Mo and V are divided by the lowest number, five, they are the most heavily weighted. This is because they are expected to have the most adverse effect on the properties of the steel for a given quantity, hence smaller quantities can be tolerated.

$$C_{eq} = C + \frac{Mn}{6} + \frac{Cr+Mo+V}{5} + \frac{Ni+Cu}{15} \qquad \text{Eq.2.2}$$

Various elements are added to steel either for microalloying purposes to produce desired properties, or unintentionally, though residuals in the scrap, coke, or ore. Since all the elements in a composition effect the steel's properties, predicting the properties of a composition is very complex and most compositions are developed experimentally. Micro alloyed steel has slightly improved properties than mild steel due to the addition of small amounts of alloying elements (0.05 to 0.15%) which in small quantities, do not greatly add to the cost. Common microalloying elements include Vanadium, Chromium, Niobium and Molybdenum. On the other hand, inclusions are impurities that are not metallically bonded to the metal lattice. Instead, inclusions are particles surrounded by the lattice.

Non-metallic inclusions (NMIs) have an important role in processes involving ductility, fracture, fatigue, and corrosion, such as rolling and bending reinforcing bar. The effect of NMIs depends on the type, size, and distribution. In recent decades, the steelmaking industry has made process improvements to better control inclusion volume fraction, size and composition which has led to more consistent formation of inclusions with desirable properties [30].

There are various possible effects that NMIs can have on steel properties. The effect of NMIs depends on some of the inclusion's properties such as the plasticity as a function of temperature and the coefficient of thermal expansion. Inclusions that are plastic at the working temperature will deform when the steel is worked. They become elongated along the major working direction, and this creates shape anisotropy in the inclusions so any steel properties that are influenced by NMIs will be anisotropic. On the other hand, plastic deformation of a matrix containing hard inclusions will typically cause the inclusions to break and redistribute.

The effect of NMIs on steelmaking processes, such as rolling and bending, can vary depending on the type of inclusion. NMIs have ionic, covalent, or mixed bonding behaviour. This means they are usually brittle at room temperature and are not strongly bonded to the metallic matrix. Their weak bond to the matrix can create voids and separation when the matrix is deformed [30].

2.5.1 Carbon

Steel contains up to two wt % carbon which improves its strength and hardness compared to pure iron. Carbon is the most common and least expensive alloying element added to steel. It is added to steel through the process of carburizing. Carburizing involves heating iron in the presence of a material containing carbon. The amount of carbon diffusion into the steel depends on the temperature and amount of time for the process.

Carbon in steel has three forms: solid solution, grain boundary segregation, and carbides [31]. The types that form depends on the manufacturing process, for example quenching causes carbon atoms to remain in solid solution. Table 2.1 shows that the carbon content limit of the final reinforcing product is 0.24 wt%, which is classed as a low carbon steel [11].

2.5.2 Nitrogen

Nitrogen is considered the most difficult residual element to control in the EAF. High nitrogen contents can cause many detrimental factors including irregular mechanical properties and poor cold forming ability in hot-rolled steel and heat affected zones (HAZ). Scrap steel typically contains 30 – 100 ppm nitrogen and the maximum nitrogen content in reinforcing steel is 140 ppm so removing nitrogen is not usually an issue for reinforcing steel [11,32].

In addition to being a residual element, nitrogen can also be absorbed into solution when the surface of the steel melt is exposed to an atmosphere containing nitrogen. In an EAF, the arcs ionise the atmosphere and dissociates nitrogen from the atmosphere into atomic or ionic nitrogen which promotes absorption into the melt. A cover of slag over the melt minimises this reaction by forming a protective layer between the melt and gaseous nitrogen. Also, a closed furnace operation and diluting the nitrogen in the furnace atmosphere reduces nitrogen absorption rates. Carbon monoxide is generated in the steel melt from the reaction between iron oxide and carbon. This carbon monoxide dilutes the nitrogen in the surrounding atmosphere, lowering nitrogen absorption rates [32].

2.5.3 Copper

Copper is a scrap residual element and can seriously affect the quality of the steel produced. Copper can have a detrimental effect known as hot shortness. The addition of copper can increase brittleness in the temperature range 1000-1300°C which leads to surface cracks appearing during casting or hot rolling [33]. Copper also reduces fatigue strength and impact resistance of steel [34].

Flat products require residual elements to be minimised to achieve soft, deformable sheets with a high-quality surface finish. Long products on the other hand, can often be more flexible but the level of copper content and other residual element content must be consistent for accurate rolling operations.

To minimise the copper content in steel, it is limited and monitored in the scrap feed. Since copper has a lower affinity to oxygen than it has to steel, it is not removed from a steel melt through oxidising [35]. Various other methods exist for removing copper but involve extra processing stages so monitoring of the scrap input is often the easiest method of control. The copper content in steel scrap is controlled and reduced by blending the scrap with other low-copper iron sources such as other scrap sources, direct reduced iron, or hot metal. Charge balance models and residual model back calculation models can be used to monitor the input feed and achieve copper levels at tap below 0.1% [32].

The BS4449:2005 maximum acceptable limit for copper content in reinforcing steel is 0.85 wt% [11]. The EU-27 Steel Scrap Specification limits copper to 0.25 wt% for shredded scrap and 0.45 wt% for high residual scrap [36]. Therefore, by careful selection of scrap sources, copper content can be kept below the 0.85 wt% limit.

2.5.4 Phosphorus

Phosphorus in steel can increase inter-granular cracking and poor mechanical properties. An EAF process can reduce phosphor content to 0.015 wt%. This is low enough for reinforcing bar since the specified content is 0.05 wt% [11,32]. Phosphorus is removed through basic, oxidising conditions, low temperature and good mixing between the slag and melt. Most of the phosphorous content in direct reduced iron is in oxide form and favours entering the slag rather than the melt. So, phosphorous content of reduced iron does not have a significant influence on the reinforcing steel properties since most of it is removed.

2.5.5 Sulphur

Iron can occur naturally as a sulphide ore (FeS). To use the iron in this ore to make steel it must be separated from the sulphur. Coke and auxiliary reductants can also contain sulphur as sulphides and are often the main source of sulphur in steel [37]. The bulk of the sulphur in coke is transferred to the slag and a small amount exits as gas through chemical reactions during the combustion of coke. However, some sulphur remains in the metal.

Sulphur dissolves in liquid iron but the solubility of sulphur falls as steel solidifies. Therefore, sulphur in the steel is liberated from solution in the form of iron sulphide (FeS). This forms a eutectic with the neighbouring iron. This Fe-FeS eutectic weaken the bonding between grains and causes a large increase in brittleness at the hot rolling temperature, known as hot shortness. For this reason, Sulphur is regarded as an impurity that needs to be reduced in reinforcing steel [38].

Carbon in coke is a common reducing agent but this is not suitable for sulphur since carbon sulphide (CS) is unstable. Certain metals with higher affinity to sulphur, compared to iron, can be added to form sulphides preferentially to iron sulphide. The metals react with any iron sulphide in the steel to produce a metal sulphide and pure iron. For example, manganese reacts with iron sulphide to produce manganese sulphide and iron, as shown in Eq.2.3. Manganese sulphide is relatively soluble in the slag so can be used to transfer the sulphur from hot metal to slag.

$$FeS + Mn \rightarrow Fe + MnS \qquad \text{Eq. 2.3}$$

2.5.6 Manganese Sulphide

The most common sulphide precipitating during solidification is manganese sulphide (MnS). Manganese is added to the steel to suppress the precipitation of FeS by preferentially forming MnS instead. Some of the MnS transfers to the slag but some remains in the steel. MnS particles can be desirable because they are ductile, enhance machinability and can be used to control grain size in the austenite to ferrite transformation. However, there are also detrimental effects of MnS such as reduced strength and anisotropic properties. The effect of MnS inclusions depends on many factors such as the steel composition, the manufacturing processes, and the type of inclusions that form.

Simms and Dahle created the original classification of MnS inclusions in steels [39]. They characterised MnS inclusions into type I, II and III. The oxygen content controls the MnS morphology and which type of inclusions are formed. Aluminium and silicon are the main deoxidisers that effect the MnS formation.

Type I is spherical and randomly distributed throughout the structure [39]. It often forms a duplex structure with silicates and is common when silicon has been used as a deoxidizing agent. Type I inclusions generally give the steel high ductility.

Type II has a dendritic structure, distributed as chain-like formations or thin precipitates on the grain boundaries [39]. This often forms when steel is deoxidized with traces of aluminium (0.01 – 0.03 wt%) and it causes extremely low ductility in steel.

Type III are irregular in shape and randomly distributed in grain boundaries [39]. This is found when steel is deoxidised with an excess of aluminium (≥0.04 wt%) and it gives an improvement in ductility from the values associated with type II.

You et al. developed a comprehensive model to simulate manganese sulphide formation during solidification of steel and calibrated this with experimental results [40]. After fitting the parameters to the experimental results, the model showed that decreasing cooling rate increased the inclusion size and reduced the total number of inclusions. Also, increasing sulphur content increased the inclusion size while the total number of inclusions remained relatively constant.

The processing methods used also effect the characteristics of MnS inclusions that form, particularly rolling which elongates the MnS inclusions. Type I MnS is much harder than the other types and during rolling it deforms to a 'lozenge' shape. Any silicates at the inclusion usually deform more than MnS so appear at the tips of the lozenge shape. Type II and III inclusions elongate much more than type I during rolling and become long, thin shapes known as stringers. Type II are found in clusters, rather than isolated inclusions [39]. Elongated inclusions in the rolling direction can create anisotropic properties. Results from Wu et al. show greater elongation prior to fracture in the rolling direction, in which inclusions are elongated, compared to the transverse direction but found little directional variation in tensile strength for hot rolled steel [41].

The importance of MnS inclusions on the processing characteristics of reinforcing steel bar is likely to depend on their consistency. Research has shown the presence of MnS inclusions in rebar, but the type, size, and proportion are not well reported [21]. If their size, type, or proportion is inconsistent, this could be a cause of some of the common processing inconsistencies. On the other hand, if they are found to be consistent, they are unlikely to be the cause of any irregular processing.

2.6 Reinforcing Steel Production

2.6.1 Blast Furnace

The blast furnace is traditionally the main process for ironmaking and is currently responsible for approximately 70% of global crude steel production [1]. Molten metal of consistent quality is produced by a blast furnace, and this can either be cast or further treated in a basic oxygen furnace (BOF) to produce steel. Usually, a BOF uses 75% iron from a blast furnace and 25% steel scrap [37].

To obtain metallic iron, iron ore is reduced using a reducing agent and thermal energy. The iron ore is reduced by rising carbon monoxide, which produces metallic iron and carbon dioxide as shown in Eq. 2.4. The carbon dioxide is instantaneously reacted with coke to form more carbon monoxide. reduced iron absorbs carbon from the coke (carburises) and simultaneously melts. Molten metal collects at the bottom with a slag floating above it and both are tapped at fixed intervals. Products of the blast furnace are carbon-saturated iron, slag, top gas, and flue dust. Four components make up about 96% of the slag, these are SiO_2, CaO, MgO, and Al_2O_3 [37]. The minor components are MnO, TiO, KO, NaO, S, and P [42]. Figure 2.14 shows a diagram of a typical blast furnace [43].

$$Fe_2O_3 + 3CO \rightarrow 2Fe + 3CO_2 \qquad \text{Eq. 2.4}$$

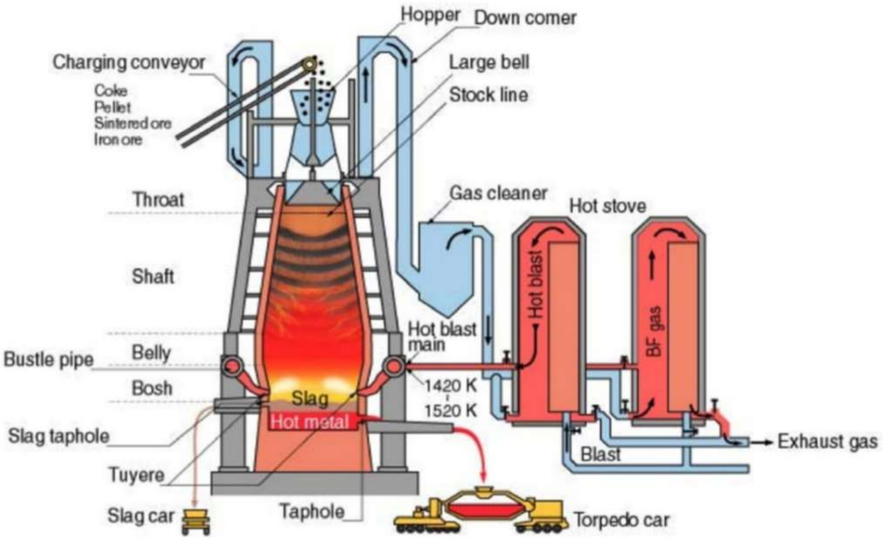

Figure 2.14 Diagram of the major components of a Blast Furnace. Iron ore, slag formers, and coke are fed into the furnace at the top in alternating layers. Carbon-saturated iron is tapped at the bottom of the furnace and a layer of slag is tapped above this [43].

2.6.2 Basic Oxygen Furnace

To make steel from the iron produced in a blast furnace, a BOF is used. Depending on the pre-treatment, 75 to 95 percent of the metallic charge is hot metal from a blast furnace and the rest is steel scrap [44]. Some alloying elements are included in the charge to meet steel specifications.

The BOF uses an oxidation process to remove oxidizable elements from hot metal and scrap and move them to the slag. Oxygen and a highly basic alkaline material are used, hence the name basic oxygen furnace. A mixture of oxygen, calcium oxide (CaO), and burnt dolomite is blown into the molten steel through a lance at high enough pressure. Oxygen is blown into the melt to oxidise elements such as carbon, silicon, and phosphorus.

2.6.3 Electric Arc Furnace

Reinforcing bar in the UK is mainly produced and refined in an Electric Arc Furnace (EAF), primarily from scrap steel. Melting scrap requires less than 30% of the energy required in iron ore reduction, which is the method of steel production in a blast furnace [45]. The refined steel is cast in billets which are processed further in stages such as hot rolling, quenching and hot spooling to produce reinforced steel coils.

The EAF, as illustrated in Figure 2.15, begins by charging, this is preparing and placing scrap metal in the furnace. There are three types of scrap the EAF is charged with; obsolete scrap such as appliances that no longer have use, Industrial scrap produced through steel processing and internal scrap such as metal produced that did not meet quality requirements. Large and small scrap pieces are arranged to melt everything at a similar rate and avoid vaporising small parts. Electricity is conducted through graphite electrodes to create an arc which melts the metal. As the current passes through the metal, resistance in the steel generates large amounts of heat and the electrodes can reach 3000°C [46]. This heat melts the steel very quickly, so cycle time is usually less than an hour [46].

Some refining can be done in the EAF. The graphite electrodes are consumed, adding carbon to the molten steel [47]. Oxygen can be added to aid removal of impurities such as sulphur, aluminium, manganese and phosphorous, which oxidise at this stage. Oxidising creates slag which floats to the surface of the melt. This slag contains most of the impurities and provides insulation to reduce heat loss from the top of the melt, while also limiting radiation damage on the furnace walls. De-slagging is required to remove the impurities from the steel. The EAF is tilted, and the slag is poured out through the slag door. Finally, the furnace is tapped, the tap hole opens, and the furnace is tilted to pour the steel into a ladle.

The EAF is a very important process as it has key advantages compared to the Blast Oxygen Furnace (BOF). These include the ability to reuse scrap steel, fewer emissions are released, and less energy is required [48].

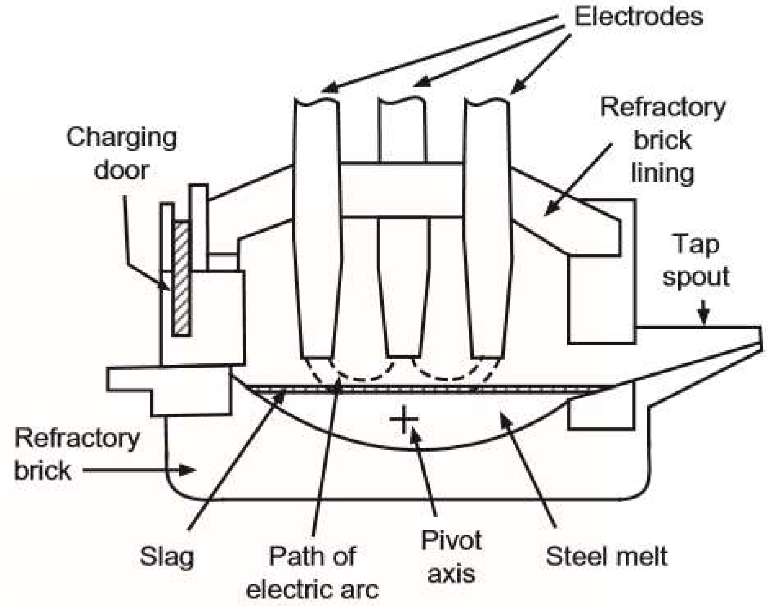

Figure 2.15 Diagram of a typical EAF. Material is loaded through the charging door; then electrical current is passed through the electrodes into the charge to generate up to 3000° [46].

2.6.4 Comparison of the Blast Furnace and EAF Processes

Some key differences between the blast furnace and the EAF process routes are the input materials, energy required, emissions, efficiency, and steel quality. Figure 2.16 shows the typical process routes of steel production using either a blast furnace or an EAF. Steel produced either from a blast furnace and BOF or an EAF is made from iron ore or scrap steel and uses coal and limestone. The blast furnace and BOF are both used in the same process route to create steel, so these processes are combined in this comparison with the EAF. Likewise, the EAF process route considers the reduction and steel refining processes, as these stages are only required for the EAF.

The quality of steel produced in an EAF can be less predictable than steel produced in a blast furnace and BOF. The main material used in the EAF is scrap steel. Steel can be recycled with almost zero loss of mass or quality, and this requires less energy than iron ore reduction. On the other hand, the main source of iron in the bast furnace process is iron ore which must be mined. Mining requires more resources than scrap collection and iron ore is a finite resource. Both feed sources contain impurities, iron ore usually contains oxides, sulphur and elements that naturally occur in iron ores, whereas scrap can contain any element that was alloyed with the steel in its previous use, and contaminants such as paint and other metals. Since scrap steel is collected from an array of different sources, the exact composition and contaminants can vary greatly. Residuals in the scrap such as tin, copper and nickel do not oxidise when the steel is heated so could be left in the final product and cause undesirable properties. This increases the difficulty for producing an accurate composition of steel by the EAF process. However, EAF steelmaking technology has improved in recent years and high-quality steels are capable of being produced.

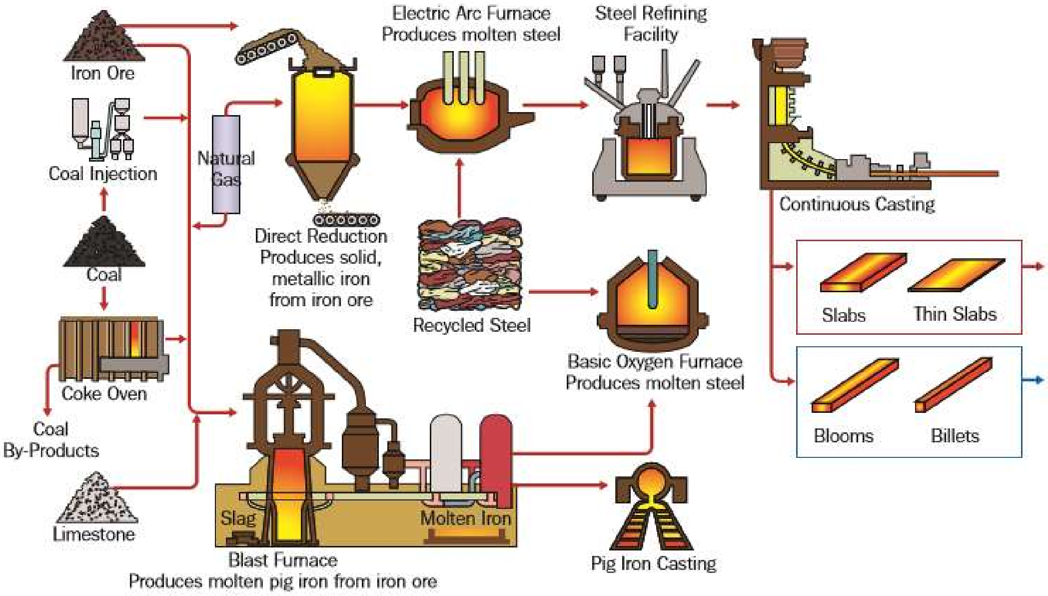

Figure 2.16 Ironmaking and steelmaking process flow diagram [45]. *The major ironmaking process routes are blast furnace ad BOF or EAF. Both routes require additional processes such as refining and casting.*

The environmental effects of EAF processes are much more sustainable than the blast furnace – BOF process and there are less health risks. A study by Li et al. calculated that the amount of CO_2 emission of crude steel is approximately 1149.7 kg/tonne from the blast furnace – BOF and only 46.6 kg/tonne for the EAF [49]. Blast furnaces require coke for heat, reduction, and carburizing. The coke plants which create coke have multiple environmental and health issues in addition to those associated with the combustion of the coke. Coke is a fossil fuel and releases CO_2 when it is used for reduction and combustion which contributes to greenhouse gas emissions. Long term exposure to coke oven emissions can cause multiple health problems including increased risk of cancer [50].

Alternatives to coke in blast furnaces and techniques to reduce the amount of coke required are being used and researched. Alternative sources of carbon include biochar, which is a wood-based product, and waste tyres [51–53]. Tyres and plastics could also substitute for coke and coal as fuel. According to Devashayam et al, the carbon footprint could be reduced by approximately 30% by using waste plastics compared to other carbon sources, and energy consumption could be reduced [54]. Plastics have a higher hydrogen content than coke, and this hydrogen acts as a reductant in addition to carbon monoxide. Hydrogen has higher diffusion rate which increases the reaction rate and efficiency. Therefore, process temperature could be reduced by 100-200°C, further reducing the energy required [54]. Blending plastic with coke has also been shown to reduce content of sulphur in the reduced metal compared to pure coke, with 0.00368 wt% sulphur being achieved [53]. However, research into these carbon alternatives is limited and pilot scale trials would need to be completed before a new material or method could be implemented. These alternatives also release carbon so still have similar negative environmental effects.

The source of heat for the EAF process is electricity, whereas a blast furnace and BOF uses coke combustion. If the electricity is produced by renewable sources, this vastly reduces the amount of CO_2 emissions. Li et al. estimated that 33% of the total carbon sources in EAF steelmaking are from fossil fuels while almost all the carbon used in blast furnace – BOF production is from fossil fuels [49]. The EAF process also uses coal as a reducing agent and for carburizing. To remove the need for coal in an EAF process, alternatives to fossil fuels are currently being developed for reduction and carburising agents. For iron reduction, direct reduction using hydrogen created by renewable energy sources is an alternative which some manufacturers are currently considering replacing coke ovens with [55]. Hydrogen and iron oxides produce H_2O instead of CO_2 which makes eliminating CO_2 theoretically possible. The alternative sources of carbon that are considered for blast furnaces could also be used with the EAF.

2.6.5 Rolling

Once refined, steel melt is cast to produce solid steel in the desired shape. Many processes utilise continuous casting for production capacity. Steel can be cast into rectangular billets which are suitable for further rolling to create products that cannot be easily cast, such as long bars.

To produce reinforcing steel, billets are reheated and hot rolled into long circular bars before the final set of rollers imprint the rib pattern which is characteristic of reinforcing steel. Rolling is completed in stages to gradually reduce the diameter and change the shape of billets. Steel can either be rolled hot or cold and the rolling temperature effects the final properties of the steel.

Hot rolling involves rolling steel that is above the recrystallization temperature. Generally, this temperature is 850 – 1200 °C, where the steel is in the austenite phase [56]. To achieve the required temperature, the billet is either heated in a furnace prior to rolling or steel is rolled directly from a continuous casting process. Large deformations are possible with less passes and less wear on rollers compared to cold rolling since the hot metal is more ductile. Hot rolling breaks the grain boundaries and forms a new, equiaxed microstructure with strong grain boundaries and smaller average grain size. This technique improves strength, ductility, and formability. The surface quality can be worse than cold rolled steel because the hot surface is oxidised by air, which produces large amounts of scale and can lead to pitting corrosion. However, quenching shortly after the hot rolling process reduces the time that the steel is hot enough for scale to form.

Cold rolling is a rolling process where the metal is below the recrystallization temperature so existing grains are elongated. This increases yield strength and hardness by introducing defects which harden the microstructure, preventing further slip. This effect is called work hardening. Another advantage of cold rolling is better dimensional tolerances as the surface does not oxidise. Since steel at room temperature is less malleable, cold rolling requires more force and is more expensive.

Reinforcing steel bar is generally hot rolled since the quench cooling is completed once the bar geometry is created. By heating prior to rolling, less energy is required for the rolling process and the steel is the correct temperature for quenching. After quenching, the steel would be too hard and brittle to be rolled effectively.

Rolling is the most significant factor effecting dimensional accuracy of the final product because the dimensions of the steel change the most in this stage. Factors affecting accuracy of rolling can include the distance of the roller gap, feed rate, roller wear, steel and roller alignment and temperature distribution in the steel. The distance between rollers, feed rate and roller wear can be measured and predicted relatively accurately and planned maintenance such as replacing rollers prior to significant wear is implemented to improve accuracy. Temperature is made homogenous by heating the billets for sufficient time prior to rolling. On the other hand, the alignment of steel with the grooved rollers can constantly vary during rolling and is difficult to monitor and control.

Roller wear changes the geometry of the rollers and changes the dimensions of the rolled material if not accounted for. Flat rolls are used to create flat sheets while grooved rolls create other profiles, such as reinforcing bar. Grooved rollers are more complex to produce and maintain, and they wear significantly more than flat rolls due to their diversity in temperature, pressure, and stress fields. There are various mechanisms of wear during rolling, including abrasion, thermal fatigue, corrosion, slip and adherence of work material to the roll surface.

Non-uniform wear is recognised as a major detriment to section rolling but this can be controlled through roll pass design and statistical analysis [57]. Rolling loads and stress distributions should be designed to ensure stable and uniform wear of finishing rolls. Roll pass design can be improved to reduce the wear on rolls and increase life of rollers. Through a new roll pass design, Osadchii et al. was able to extend roller life by a factor of about 3.5 in a tube rolling mill [58]. Similarly, Pooyutovskii et al. improved the product quality and roll life by 1.3 times through roll pass design in a piercing mill [59].

A study by Spuzic et al. reviewed wear of hot rolling mills and key aspects of controlling roll wear [57]. It states that the main requirements of rollers differ at various stages of the rolling line. The initial stages of the rolling process require heat shock resistance and material strength most. Whereas, at later stages, resistance to abrasive wear becomes the most important necessity. Spuzic also showed through scratch testing that abrasive wear differs depending on whether the specimens are under tension or compression. Steel material under tensile stress showed a decreased resistance to abrasive wear. The study also reviewed models for wear and found that these mainly focused on the simpler case of flat rolling, rather than grooved rollers.

Alignment between steel bar and rollers can be difficult to control. The impact of alignment is less influential for flat rolled sheet but can be more important for steel bar such as reinforcing bar. If a steel bar travelling between sets of grooved rollers is not aligned with the centre of a set of rollers, it will not create the desired profile. Rolling guides are designed to direct the feed material at the entry and exit of rollers. Roller guides can be used to reduce the friction caused by the guides. These guides can require continuous adjustment to keep a changing feed aligned so dynamic models for lateral steering control of a pivoted entry guide have been developed and validated [60]. To steer the strip¸ constrained model predictive control has been designed which uses reference signal jumps and feedforward to adjust the output prior to the input being raised.

2.6.6 Quenching

Quenching is the rapid cooling of a metal to obtain certain desired properties, such as increased strength and hardness. The quenchant is the medium used to extract heat from the part, this can be liquid, solid or gas. To achieve high strength and toughness of steel with low alloying elements, a rapid quench rate can be used to convert Austenite to Martensite. When hot steel contacts a liquid quenchant, there are normally three stages of quenching. These are: vapour stage, boiling stage, and convection stage [61].

Often, optimal properties are obtained at the expense of high residual stresses or high distortion. So, the optimum quench rate is one where the property requirements are just met, and residual stresses are minimised. To achieve the conversion of Austenite to Martensite, the quench rate must be fast enough to avoid the formation of upper transformation products like Bainite and Pearlite. The critical quench rate is dependent on the steel composition. For a thick component, the surface cools more rapidly than the centre. This means that the surface could cool at the critical cooling rate and fully harden, while the centre cools more slowly, forming a pearlitic or Bainitic microstructure.

In reinforcing bar steel production, quenching occurs after hot rolling. The rolled bar passes through quench boxes which spray water quenchant around the bar. Since the steel is already heated to the austenite zone for rolling, it does not require further heating prior to quenching. The spray causes the outer surface to cool faster than the critical quench rate, so martensite grains form. However, the core cools more slowly and does not form martensite. Instead, a ferrite and pearlite microstructure develop. This produces a dual phase steel which has a softer more ductile core, with a layer of harder martensite around the edge.

Increasing the ability of steel to through-harden can be achieved by increasing the proportion of alloying elements in the steel. Manganese, chromium, and Molybdenum can all increase the hardenability of the steel by reducing the critical cooling rate for Martensite transformation. Increasing the carbon content, while increasing alloying content, can also lower the martensite start transformation temperature. Alloying elements can be expensive and may increase the carbon equivalent value, which can increase cracking distortion. A sufficient quenchant rate must be used that will achieve martensite transformation but is slow enough to avoid cracking and distortion.

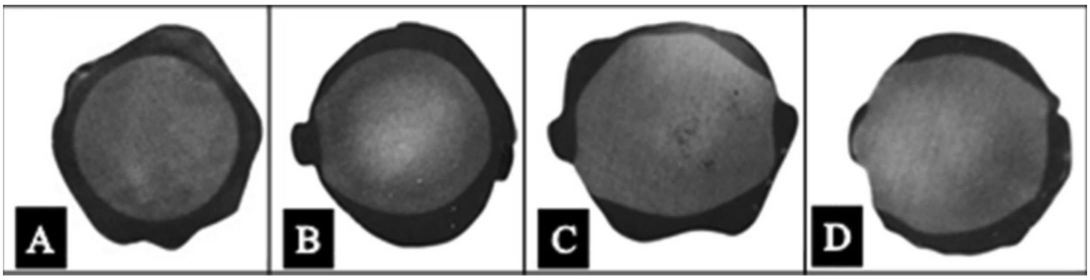

Figure 2.17 Examples of different types of inadequate CSPD in quenched rebar [15]. *Sample A is relatively uniform and concentric, whereas the others have large changes in martensite thickness around their cross sections.*

To produce uniform reinforcing steel with consistent processing behaviour, the layer of martensite should be consistent around the circumference of reinforcing bar. If there is a greater volume on one side of the bar than the other, it will have different hardness properties on each side and bending will require a different force depending on the orientation of the bar. From the samples studied from various producers, Nair and Pillai found inadequate cross-sectional phase distribution (CSPD) with many samples having a discontinuous or non-uniform martensite phase. Inadequate cross sections examined in the study are shown in figure 2.17 [15]. The non-uniform martensite layer is likely to be caused by the quenchant flowing unevenly around the bar so that certain sections are cooled more than others. The study used macro etching to give evidence of both even and uneven martensite layers and focused on the corrosion effects of uneven martensite in concrete [15]. However, the effect of uneven martensite on bending, tensile and coiling properties, or a solution for avoiding this manufacturing error was not investigated.

2.6.8 Coiling

Once reinforcing bar has been rolled to its final dimensions, it is often spooled into large coils for transportation. These coils are transported to customers who process the coils to produce individual reinforcing shapes for use in concrete structures. Flat products are usually coiled as well, these have a single row and multiple layers. On the other hand, coiling of bars involves multiple rows on each layer, as shown in figure 2.18. Both coils involve wrapping the steel around a mandrel, which is then removed so the coil can be moved and left to cool down to room temperature. To coil rebar, the lead end is gripped by the coiling machine and pulled around the first layers, after which it is released, and the coil continues to wrap around the mandrel as it rotates. Since the processes are similar, some research for flat coils can be applied to the bar coiling process.

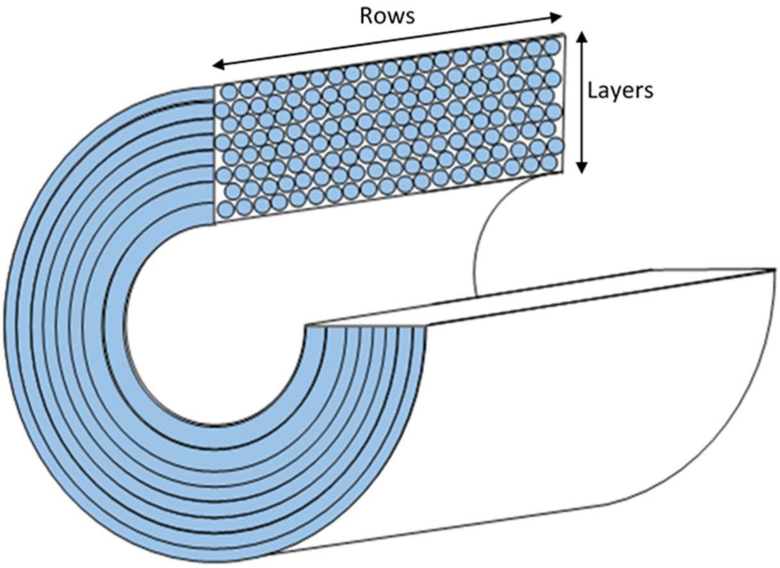

Figure 2.18 Cross section illustration of a rebar coil showing the layers and rows. A two-tonne coil of 12 mm diameter rebar contains 13 layers.

Reinforcing metal is coiled almost immediately after the quenching processes, at approximately 450 – 600 °C. This temperature allows the steel to deform more easily so compact coils can be produced. Once coiled, the steel self-tempers as retained heat in the core of the bar disperses into the edge areas and tempers the martensite grains.

Coiling can have a significant effect on the steel properties, especially on the subsequent cooling and self-tempering. Various research has been done to characterise the heterogeneities of coil cooling. Jacolot et al. used thermal imaging and finite element modelling to show the coil cooling process and predict the final microstructure and mechanical properties [62]. The results showed that the coil does not cool at a consistent rate, instead certain areas cool faster than others. Steel that cools faster allows less time for grain growth, so these areas have smaller grains and smaller pearlite spacing. Therefore, inconsistencies exist in the steel's properties. The pearlite spacing, tensile strength, and Niobium hardening were calculated along a coil using a thermal model for three positions across the strip. The results for pearlite lamellar spacing are shown in figure 2.19. The axis is the centreline of the coil, the edge is an outer edge, and the quarter position is halfway between the edge and axis. Since the coil is symmetrical, only half needs to be calculated. This model showed small pearlite spacing of approximately 150 µm at the start and end of the coil. A clear trend of increasing pearlite spacing towards the middle of the coil exists for the axis and quarter positions. This effect is greater for the central axis, which reaches approximately 320 µm while the quarter axis reaches

260 µm approximately. This influenced the calculated yield and tensile strength, which both decreased in strength at the middle of the coil length by 35 - 40 MPa (1).

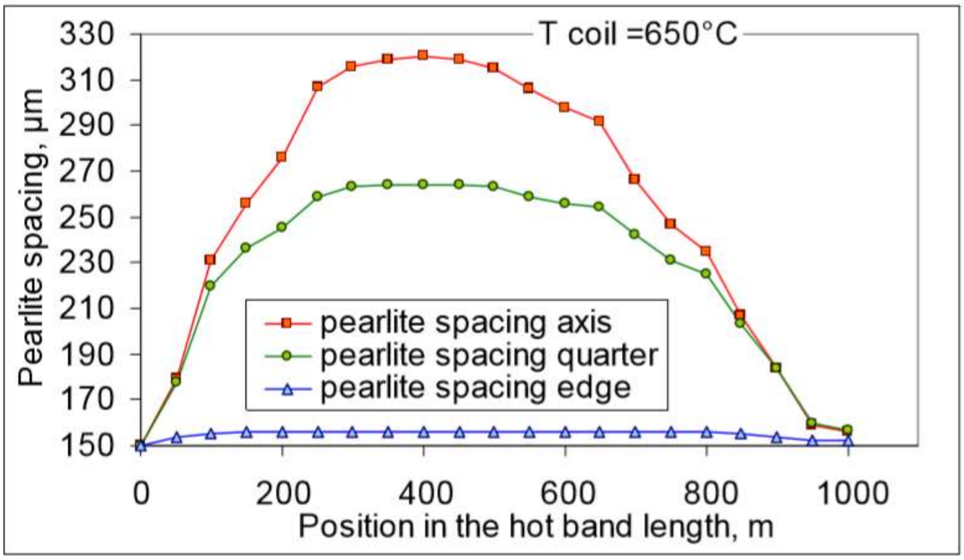

Figure 2.19 Pearlite spacing for the axis, quarter, and edge positions along a 1000 m long steel coil (61). Axis is along the centreline of the coil, edge is one of the coil edges, and quarter is a line halfway between the centre and edge. Pearlite spacing increases away from the edge.

The model is for a coil of flat sheet steel so the effect on reinforcing bar may be different, and a specific model should be created. This could involve challenges to calculate heat transfer coefficient between rows, in addition to between layers. Another limitation of the model is that it does not involve any interaction between phase transformation and thermal path. For steels that are coiled before phase transformations are completed, the transformations during cooling would affect the thermal evolution.

Buessler et al. modelled coil cooling to show the difference in precipitation of Niobium throughout a steel coil which is microalloyed with Niobium [63]. This model coupled thermal models with phase transformation since temperature evolution influences transformation kinetics and similarly, the phase transformations generate heat. Precipitate growth and UTS were studied for three locations in the coil: an inner layer close to the mandrel, a middle layer, and an outer layer. The middle layer cooled most slowly, after one hour of cooling its temperature was approximately 120°C greater than the temperature of the inner and outer layers. The results showed that sections of coil that cool faster have smaller interlamellar spacings in pearlite and a lower fraction of precipitates. The reduced cooling time allows less precipitation and the precipitates that do form have smaller radii. According to the parameterisation, smaller volume fraction and smaller radii of precipitates reduces UTS as shown in table 2.2 [63]. However, precipitation hardening is not the only way that cooling rates can affect steel properties, for example grain size is usually smaller for faster cooling rates and this could increase UTS. The effect of different cooling rates depends on the phase and composition of the steel.

Position	Fraction of Niobium Precipitates (ppm)	Radius of Niobium Precipitates (nm)	UTS (MPa)
Outer	185	1.1	488
Middle	395	1.5	496
Inner	118	0.8	477

Table 2.2 Results of the calculations for fraction and radius of Niobium precipitates after cooling at three positions of the coil and the resulting UTS, adapted from Buessler et al. [63]. *The inner position is in contact with the mandrel that the sheet was wrapped around, the outer position is exposed to ambient air, and the middle position is surrounded by neighbouring layers of steel.*

After one hour of cooling, the inner position was hotter than the outer position. In table 2.2, the inner position has a greater reduction in fraction and radius of precipitates and lower UTS than the outer position. Since the mandrel that the coil is wrapped around is only in contact with the inside, this suggests the mandrel cools the steel more quickly than air cools the outer layer. Therefore, to control cooling throughout the coil, thermal transfer through the ambient air, mandrel and the steel need to be understood.

S-J Park et al. have precisely modelled radial thermal conductivity between coil layers to assess the homogeneity of different coil cooling methods [64]. Since contact stresses are caused by differential thermal expansion of layers, they change with the temperature field. The thermal conductivity between each layer increases as the contact stress between the layers increases. The calculated equivalent thermal conductivity is a function of strip thickness, surface characteristics and compressive stresses and was shown to correspond well to experimental data. This model was then used with FEA to find stress distribution during the coil cooling duration and temperature distribution of both water- and air-cooling procedures. Water spray cooling produced the greater stress gradient although the water was only sprayed from the top face, rather than evenly around the coil. This suggests air cooling creates more even cooling and should lead to more even properties throughout the coil.

The model from S-J Park et al is for a coil of flat strip metal with different composition and processing conditions to reinforcing bar so the model would need adjusting to be applied to thermal conductivity of reinforcing bar. The contact area between layers is much smaller for round reinforcing bar because the round profile allows air between the layers. Therefore, the thermal coefficient is likely to be lower. The axial thermal conductivity would also be less since there are multiple rows with small contact area in each layer. Separate models and experimental measurement would be required to calculate the equivalent thermal conductivity values for reinforcing bar, and these must account for the convection through air voids in addition to conduction through contact areas. Additionally, rebar produced by *Celsa Steel UK* is not micro-alloyed with Niobium so the precipitation hardening, which was shown to increase strength when cooling time increased, would not be expected.

Li et al. have investigated the effect of coiling temperature on yield point behaviour for low-carbon steel [31]. Tensile tests showed that coiling temperature had a significant effect on elongation at the yield point. Increasing coiling temperature from 600°C to 750°C reduced the yield strength for this composition. Coiling temperature at 750°C was found to make micron-sized carbides disappear from the grain boundaries and nano-scale carbides appear in the grain interior, thus having the highest solid solution carbon content of the temperatures tested. Figure 2.20 shows the microstructures of the samples from this study when coiled at 600°C, 700°C and 750°C followed by annealing at 740°C. Black particles can be seen at the grain boundaries for 600°C and 700°C coiling temperatures, but these disappear when coiled at 750°C. SEM analysis combined with an energy spectrum proved that these black particles are carbides. The carbides have a pinning effect at the grain boundary, so when the carbides disappear for coiling temperature 750°C, grain size could increase more during annealing. Since this steel was cold rolled and annealed following coiling, the effects will not be the same for reinforcing bar. However, this research does suggest that coiling temperature is likely to have an impact on the steel properties. Similar tests should be undertaken to understand the influence of coiling temperature on reinforcing steel.

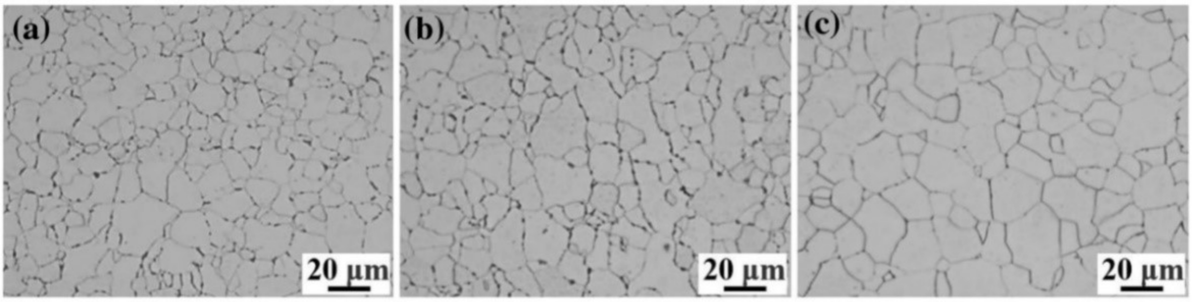

Figure 2.20 Microstructures of samples under different coiling temperatures, all annealed at 740°C. a) 600°C; b) 700°C; c) 750°C [31].

Recently, Haijun Li et al. also modelled cooling for a hot rolled coil of flat sheet steel [65]. The analysis also showed that the inside and outside of the coil cool significantly faster than the middle section of the coil. The inside cooled faster than the outside since the inner layer was in contact with the coiler drum during coiling and, once discharged from the drum, the inner layer was a lower temperature than the outer layer. For the dual phase steel in the study, the high cooling rate reduced the fraction of proeutectoid ferrite and the amount of grain refinement. This gave the inner and outer parts greater strength than the coil middle. The study then proposed a solution to this inconsistency and applied it to an industrial steel process. A U-shaped cooling process was designed to heat the start and end sections of the sheet length more than the body to increase the cooling time of the inner and outer regions once coiled. This was found to improve the longitudinal uniformity and produce closer values of yield strength throughout the coil in the industrial application, as shown in figure 2.21.

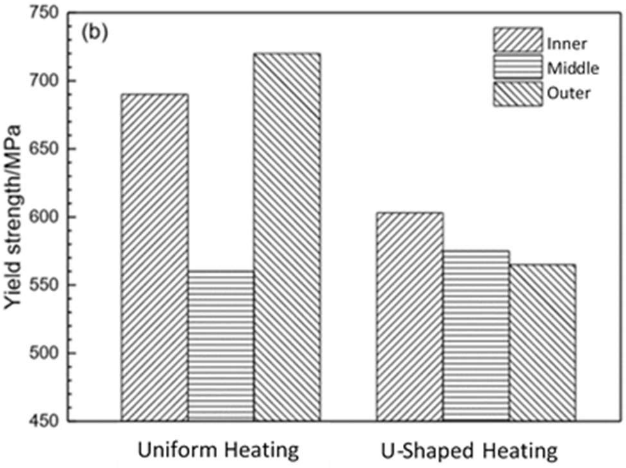

Figure 2.21 The yield strength through a hot-rolled coil, before and after the application of U-shaped cooling [65].

Chashchin et al. assessed other options to control the cooling of coils [66]. The use of a subsequent heat treatment such as annealing was determined to increase production cost by more than 30% and extend the production cycle by a few days for hot-rolled sheet steel. Another method presented is thermostatting. Thermostatting is controlled slow-cooling of the hot-rolled strip coils. The cooling rate in different turns of the coil is equalized and the rate of cooling is determined by its value in the middle turns. A thermostat is a space enclosed by a metal housing that protects the coils inside from convective air fluxes. This slows the cooling rate in the outer layers and increases cooling duration. The sides have a different amount of insulation to the top since the rate of thermal energy loss is different at the sides to the top of a coil. Chashchin applied the use of thermostats to industry and used thermocouples to measure temperature at different points in the coils [67]. The study stated that residence time in the enclosure is only required until structural changes in the steel have stopped. After this, the coil can be further cooled in ambient air conditions. The residence time suggested by this report was 18 - 22h for coils starting from 550 - 600°C, although this depends on the composition, coil dimensions and required level of uniformity. This technique was determined to be relatively productive for the industry case it was applied to.

2.7 Summary

Reinforcing bar is a ribbed steel bar produced in two tonne coils for further processing by customers. The processing forms the bar into various shapes to reinforce specific concrete structures. There are various inconsistencies experienced during processing which can cause the shapes produced to have dimensions outside of tolerance. These shapes must be scrapped, or the processing machines can be adjusted but this reduces production rate. One inconsistency experienced during processing occurs during bending. As the rebar is bent, it occasionally deforms perpendicular to the intended bending plane, as shown in Figure 2.7. Another processing inconsistency is experienced when two coils are processed by the same machine simultaneously. Sometimes, one rebar is drawn through the machine’s drive rollers further than the other, such as the two bars in Figure 2.8, leading to two structures produced with different dimensions. Often, one of these shapes is not within tolerance so must be scrapped and the coils may have to be processed individually, halving the production rate. The causes of the processing inconsistencies are expected to be inconsistency in either mechanical properties, chemical composition, microstructure, or dimensions.

The main stages of reinforcing steel production are steelmaking and refining in the EAF, billet casting, reheating, hot rolling, quenching, coiling, and cooling. An approximate thermal cycle of these stages is shown in figure 2.22. Each stage has unique influences on the rebar properties. The rapid cooling of the edge during quenching creates martensite which is then tempered as heat dissipates from the core region. Since the core cools more slowly, ferrite and pearlite form here. The EAF is the main factor effecting the steel composition since refining and adding additional elements occurs here. Hot rolling deforms a billet into the final ribbed cross section, so it is the most influential stage on the product's final dimensions. Cooling has a major influence on the phases and microstructure that forms since tempering allows grain growth and precipitation.

Research on rolling has shown that inaccuracy can be caused by roller wear, misalignment, and changes in input feed rate. In addition to effecting dimensions, rolling also elongates grains and inclusions at the working temperature and can have a significant effect on texture. These effects mean that rolling could be a cause of the processing issues.

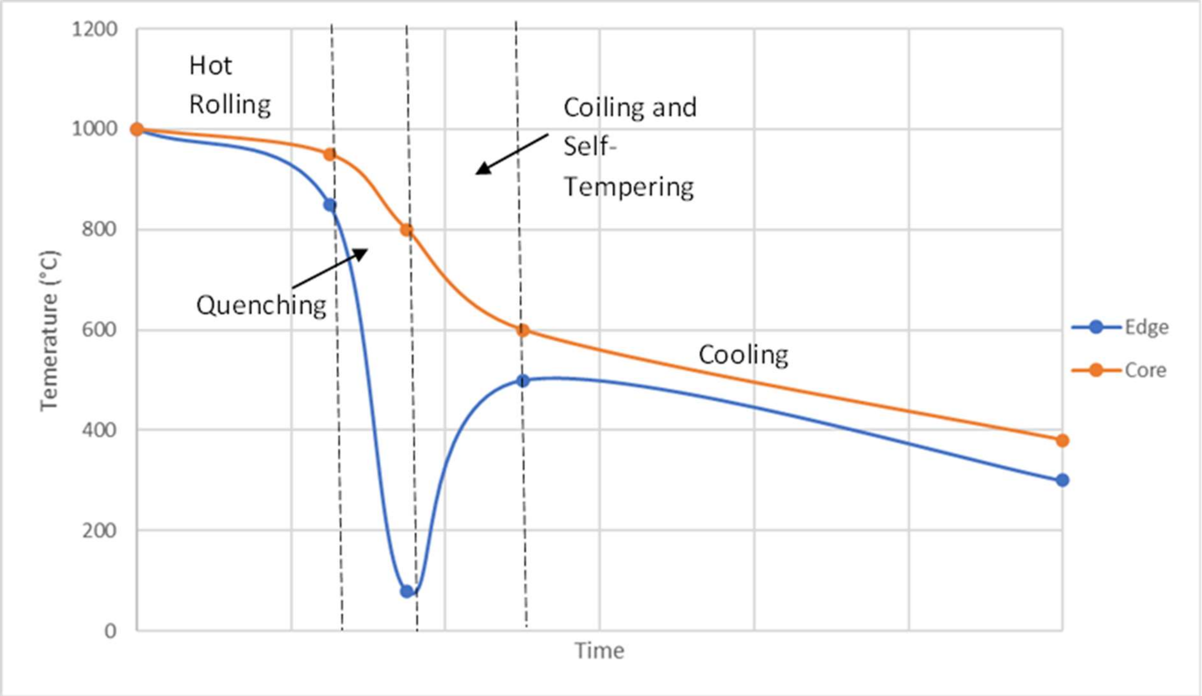

Figure 2.22 Thermal cycle of the quench and self-tempering process used to make Celsamax with approximate temperatures shown for a point at the edge and a point in the core of the rebar. The edge experiences rapid cooling during quenching, then heat from the core dissipates to reheat and temper the edge before the whole bar gradually cools after coiling.

Coil cooling has been thoroughly studied for flat sheet coils, but research on the cooling of rebar coils has not been undertaken. Flat sheet coils have been found to cool more quickly in the outer layers and at the ends than in the middle. This has led to inconsistent mechanical properties, in particular yield strength because cooling rate has a major effect on microstructure evolution. Various methods of controlling coil cooling have been developed such as a thermostat enclosure, differential heating, and adjusting rolling temperature.

Based on the existing research and results seen for flat sheet coils, this study will investigate the relationship between mechanical properties and coil cooling specifically for rebar coils. To investigate properties responsible for processing inconsistencies, the consistency of various properties of rebar will be tested. Properties that will be tested are tensile strength, microstructure, martensite distribution, composition, and dimensions. The effect of dimension inaccuracy on bending behaviour is not well known so this will also be tested. Through testing these properties, the causes of processing inconsistencies should be identified. Using knowledge of the manufacturing process, the identified causes will suggest the stages of manufacture responsible and solutions to the inconsistencies will be discussed.

Chapter 3 Coil Cut Up Testing

3.1 Coil Tensile Reports Supplied by *Celsa Steel UK*

Variations in steel properties occur both between coils and within an individual coil. To investigate the differences that occur within a coil, *Celsa Steel UK* have occasionally selected coils to cut up and measure properties along the length. The properties measured are tensile strength, deformation behaviour and deviation in weight per metre. Tensile strength and deformation behaviour were measured with a uniaxial tensile test with a ZwickRoell universal tensile machine. Samples of rebar 200 mm long are held at each end in clamp grips and strained until failure. Tensile force is measured as length of extension increases and Young's modulus, ultimate tensile strength and yield strength can be calculated from this recorded data.

Samples of a coil are taken at five heights in the coil. For each height, either eight or thirteen samples are taken, evenly spaced between the inner and outside layer. The number of samples taken at each height depends on when the coil was cut up because *Celsa Steel UK* have changed the preferred number from eight to thirteen over time. The locations of each reading are shown in figure 3.1, for a coil positioned with the flat faces parallel to the ground. The height in the coil is represented by letter, A is the top and E is the bottom, and a number represents the layer in the coil, one is the inner face, and the highest number is the outer face, either eight or thirteen. So, 1A is at the top of the inner layer, whereas E13 is the bottom of the outer layer.

Coils produced by *Celsa Steel UK* are given a coil number and have a cast number to indicate the casting that the steel was produced in. The coil number indicates the year the coil was made, and which factory line was used, since the factory has two lines which simultaneously make rebar. The first two numbers indicate the year of manufacture i.e. 16 means the coil was produced in 2016. Then, there is either a letter E or F which represent the two different factory lines. The remaining numbers are specific to the coil. Coil and cast numbers allow tracking of manufacturing parameters such as the composition, line speed and temperatures at different process stages.

3.2 Data Analysis Procedure

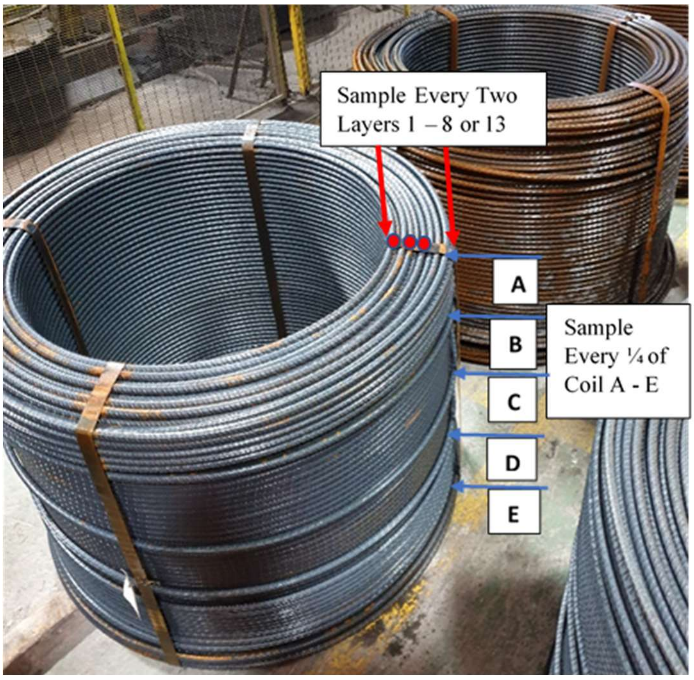

Figure 3.1 Locations of samples taken from a coil during a coil cut up. Letter denotes the height in the coil, A represents the bottom and E is the top, and number refers to the layer, beginning with one at the inner layer. The coils cool in the position shown, detached from the coiling mandrel and with one flat face on the floor.

In this project, the material reports collected from the coil cut ups were analysed and compared to find trends and differences that could be significant to the processing properties of the rebar. By separating the data value to view each of the heights where samples were taken, rather than viewing the samples in the order they would be if the whole coil were straightened, new patterns have been identified which indicate significant variations in the manufacturing process.

Based on the research discussed in section 2.6.8, it is expected that strength variations between different coil positions will be found. This is because the studies in section 2.6.8 show that uneven cooling in coils effects strength as the external faces of the coil cool faster and become stronger than middle sections. The exact effects may be different to those seen in section 2.6.8 since this analysis is for rebar coils, with different composition, which allow more air to flow between layers than coils of flat sheet products and this could improve cooling in the core. In addition, strength differences between coils are expected because customers have reported certain coils requiring less force to deform than others during post processing.

Yield strength and UTS were recorded from the tensile testing for each sample location in the coils. This has previously been used to display strength along a coil. Figure 3.2 shows the graph *Celsa Steel UK* produced by tensile testing along CM096912, a coil of rebar with 12 mm diameter which was produced in 2015. Sample position, in the order the coil was spooled in, is along the X-axis and UTS is the variable on the Y-axis. The graph shows a similar oscillating variation in both the yield strength and ultimate tensile strength (UTS). The strength oscillates between a range of 91 MPa in UTS and 95 MPa in yield strength. There is also a U-shaped trend along the whole bar so, the middle is less strong than the ends by approximately 30MPa. All 12 mm rebar coils which have been cut up and tested show similar trends to the example graph in figure 3.2. However, the reason for this oscillation and variation is not clear from this graph and it was previously considered to be a random variation. Differences in strength properties of this size are currently tolerated, providing the yield strength is always greater than 500 MPa. The tensile strength requirement in BS4449:2005 only specifies that the minimum acceptable yield strength is 500 MPa [11]. So, if yield strength is above the minimum, then any variation does not affect the British standard requirements, although it may impact the quality and ease of processing.

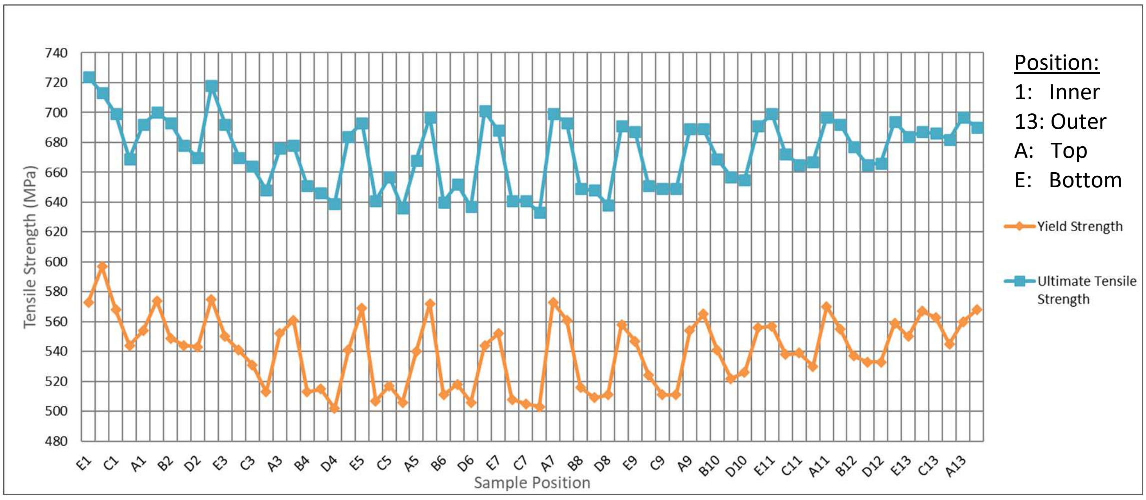

Figure 3.2 Graph showing the tensile strength along CM096912, 12 mm coil produced in 2015. Sample position is in the order the coil was spooled, the left of the X-axis is the inner layer, and the right is the outer layer.

For the objective of finding tolerance issues and the associated stages of manufacture, this study has isolated sections of the data. To determine possible patterns and reasons for the variations, the data has been separated to view the individual heights and layers for comparison between heights. Samples taken at the same height in the coil all have the same letter. The following graph, figure 3.3, shows the UTS for the same coil as in figure 3.2, but with the data points separated into individual heights. Each line represents the UTS through the layers for an individual height. The X-axis shows the layer number where one is the inner layer and 13 is the outer layer. This graph presents relationships between the position of a sample in the coil and its tensile strength more clearly than figure 3.2.

A difference in UTS between layers is evident in figure 3.3. Samples have lower UTS the further away from the surface of the coil they are located. This is evident as middle heights, B, C and D, have the lowest UTS in their middle layers. For example, C7 is the middle layer of the central height and has a UTS value of 641 MPa. The UTS on these three middle heights gradually increases towards the outer layer. In contrast, the top and bottom heights have more constant UTS values which are almost always greater than the middle heights. The top and bottom heights, as well as the inner and outer layers have the greatest UTS. These are all the external sections of the coil; the inner and outer layers and the top face are directly exposed to ambient air, while the bottom face is in contact with the floor.

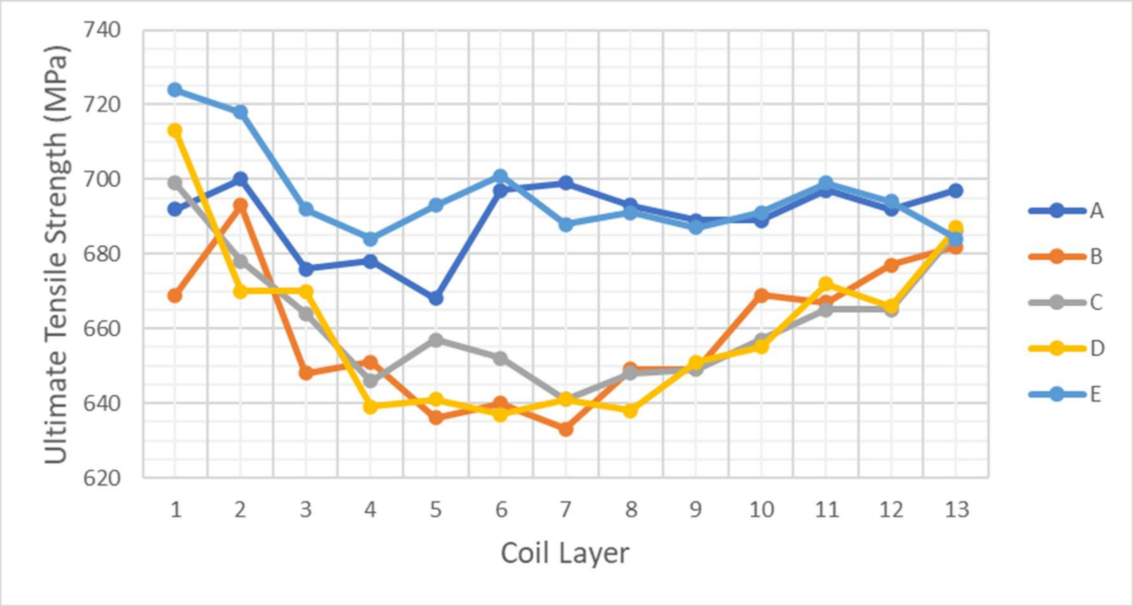

Figure 3.3 Graph showing ultimate tensile strength through a coil for individual heights in CM096912, a 12 mm coil produced in 2015.

BS4449:2005 requires that yield strength must be between 485 and 650 MPa, but there is not a specific requirement for UTS [11]. Therefore, yield strength is a more useful property to investigate. Figures 3.4 – 3.13 show the yield strength along a coil as individual heights for all coils of 12 mm reinforcing bar that have been cut up and tensile tested by *Celsa Steel UK*.

Graphs displaying UTS along coil layers at separate height, such as figure 3.3, present the same trends as the corresponding yield strength graphs for the same coil, which are shown in figures 3.4 – 3.13. While the British Standards requirement for yield strength is 485 – 650 MPa, the target *Celsa Steel UK* aim for is 550 MPa.

3.3 Yield Strength Results

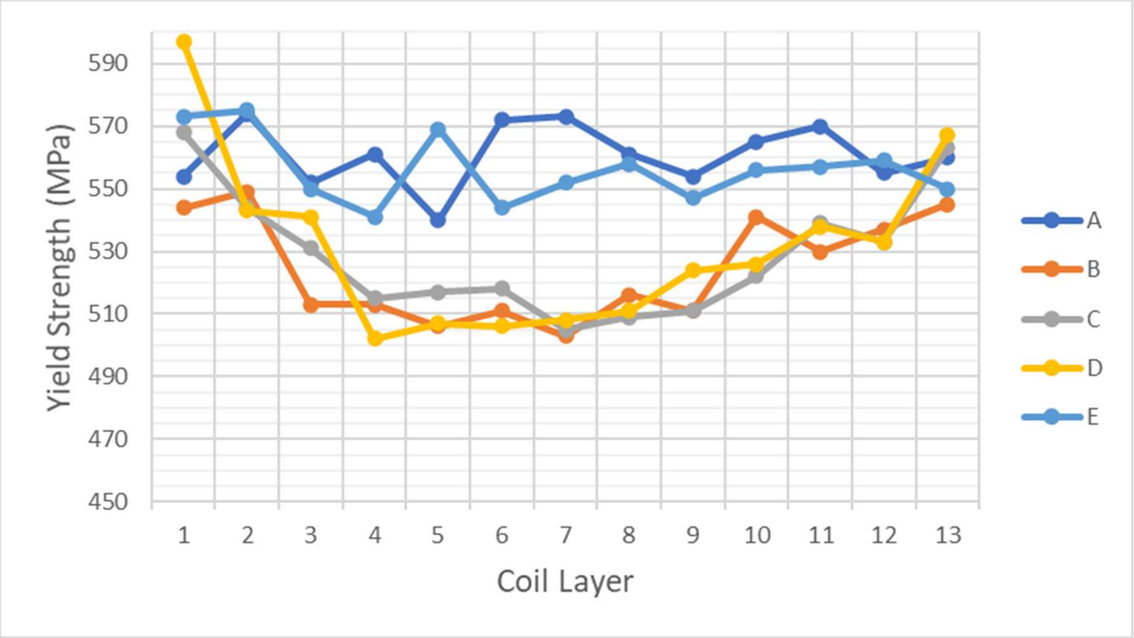

Figure 3.4 Graph showing yield strength through a coil for individual heights in CM096912, a 12 mm coil produced in 2015.

Figure 3.4 shows yield strength through coil layers for each height in the same coil that is shown in figure 3.3. Differences between certain locations of the coil are clearer in this graph. Firstly, samples at heights A and E have greater yield strength than samples in the middle heights. In the middle layer, layer 7, the yield strength at the top and bottom heights, A7 and E7, are 573 and 552 MPa, respectively. Whereas yield strength at the middle height, C7, is 505 MPa, which is 68 and 47 MPa less than each of the end faces, respectively. The second main trend is a U-shape curve in the middle heights in which the outside and inside layers, one and thirteen, have the highest yield strength, and this reduces towards the middle of the coil. The yield stress at C1 and C13 is 568 and 563 MPa respectively, and the middle point, C7, is 503, which is over 60 MPa less than either end. The greatest strength variation is in height D, which varies from 502 MPa in layer four to 597 MPa in layer one. This is a change of 95 MPa, which is 19% of the 500 MPa target. These two trends show that the exterior sections of coil, which are more exposed to air during cooling, have higher yield strength than the interior sections within the coil. The coils cool in the position shown in Figure 3.1, with the mandrel removed and one flat face, the bottom height, in contact with the floor.

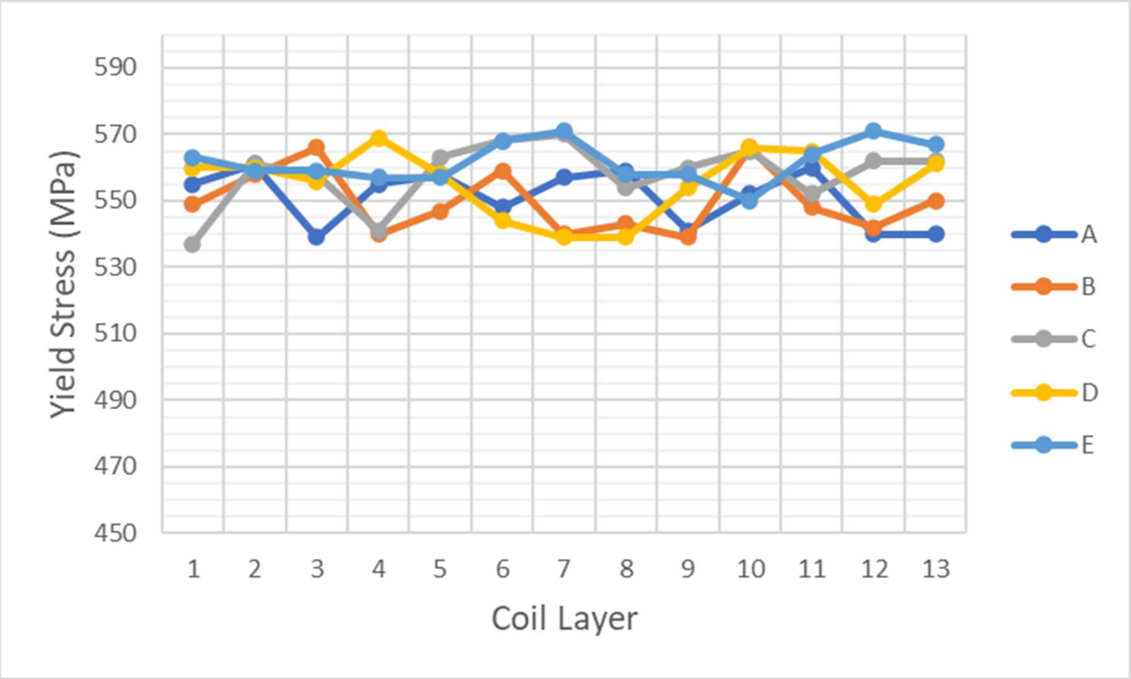

Figure 3.5 Graph showing yield strength through a coil for individual heights in CM098762, a 12 mm coil produced in 2015.

The coil shown in Figure 3.5 is a 12 mm coil produced in 2015, which is the same diameter and year as the coil in figure 3.4, but it does not show the same relationships as figure 3.4. There is less deviation in yield strength values in the figure 3.5 coil, so the tensile strength is more consistent. Yield strength varies from 537 to 571, a range of only 34 MPa. No clear relationship between strength and the height or layer is discernible as the values of strength are randomly distributed. Height D has a small U-shape as layers 6, 7 and 8 are approximately 20 MPa lower but this is not repeated by the other middle heights, B and C.

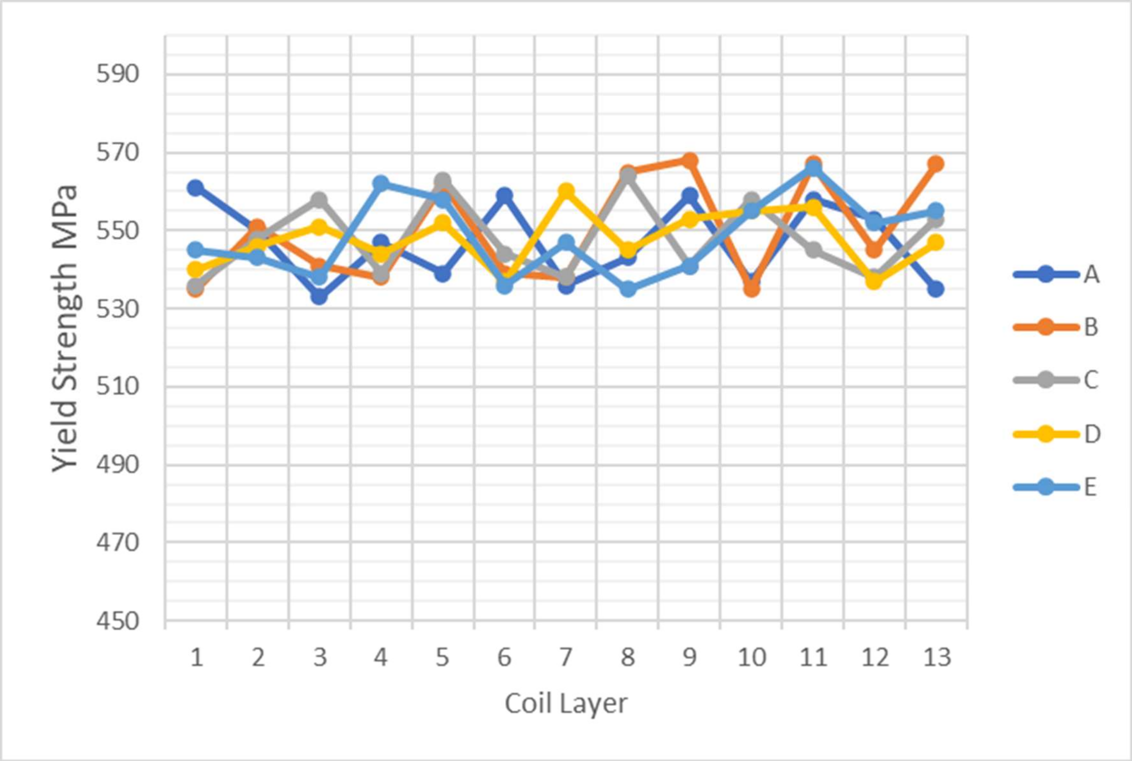

Figure 3.6 Graph showing yield strength through a coil for individual heights in CM097618, a 12 mm coil produced in 2015.

There is no clear trend shown in figure 3.6 because the values of strength between heights are similar and appear to fluctuate randomly. The yield strength is relatively consistent, varying between 533 and 568 MPa, a difference of 35 MPa.

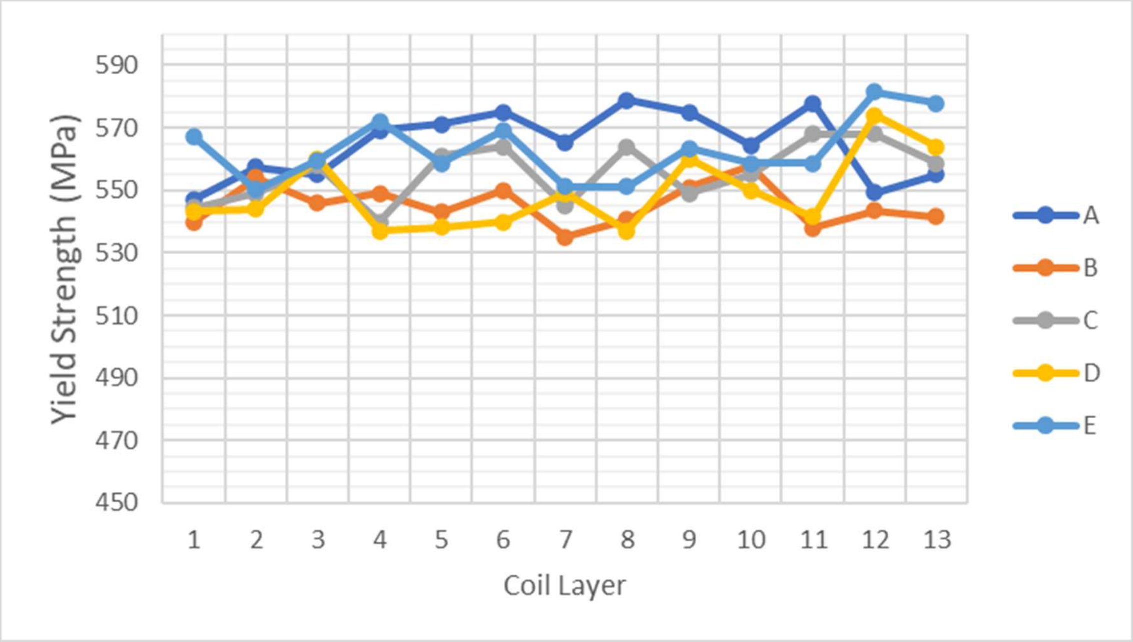

Figure 3.7 Graph showing yield strength through a coil for individual heights in CM097197, a 12 mm coil produced in 2015.

In addition to figures 3.5 and 3.6, there is also no clear trend visible in figure 3.7. The yield strength is less consistent than figures 3.5 and 3.6, as values vary by 47 MPa, from 535 to 582 MPa. There is not a clear difference between strength through the layers at each height. The top and bottom heights have the greatest strength at most layers, but this difference is much smaller than for the coil in figure 3.4.

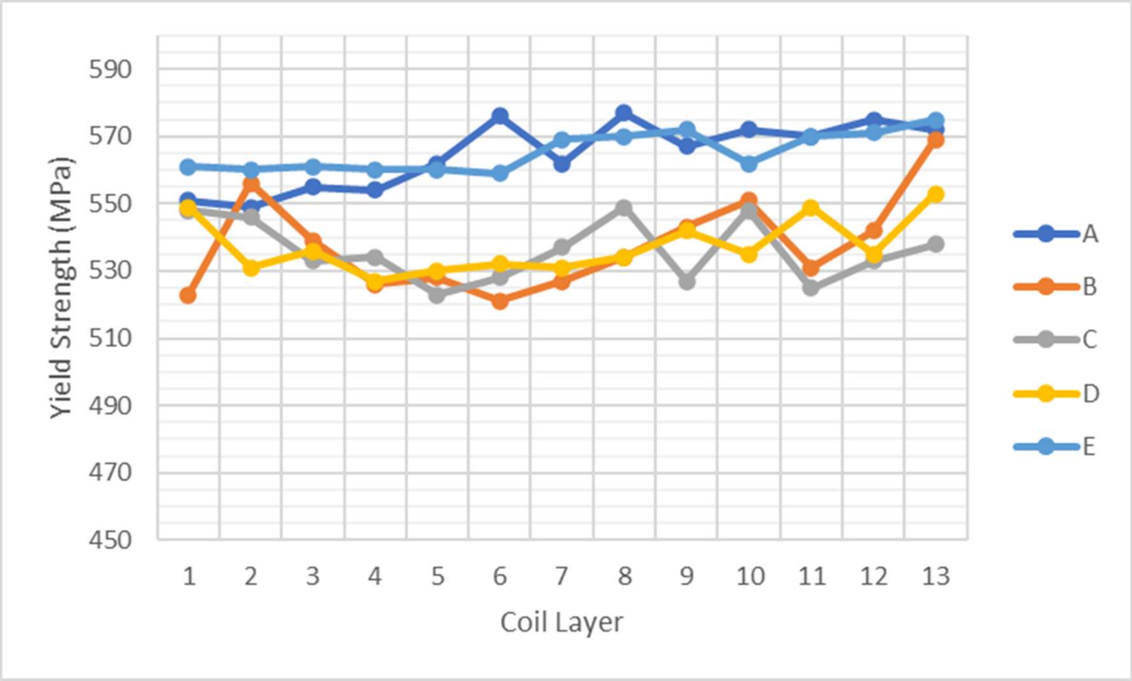

Figure 3.8 Graph showing yield strength through a coil for individual heights in CM105314, a 12 mm coil produced in 2016.

Figure 3.8 shows similar differences between layers as shown in figure 3.4. The top and bottom heights, A and E, are more consistent and greater than the middle layers. Strength values for the top and bottom layers have a range of 28 MPa, between 549 and 577 MPa. On the other hand, the middle heights, B, C and D, have lower yield strength, which is greater at the inner and outer layers than the middle. These middle layers have a larger range of 48 MPa, from 521 to 569 MPa.

Yield strength of many test points for the coil in figure 3.9 fall below the minimum acceptable limit of 485 MPa so this coil would not meet the BS4449: 2005 standards [11]. The top and bottom are stronger and more consistent along all layers. Whereas the middle and quarter heights have greater strength near the inner and outer layers. Strength ranges by only 24 MPa in height A but the middle height has a range of 46 MPa.

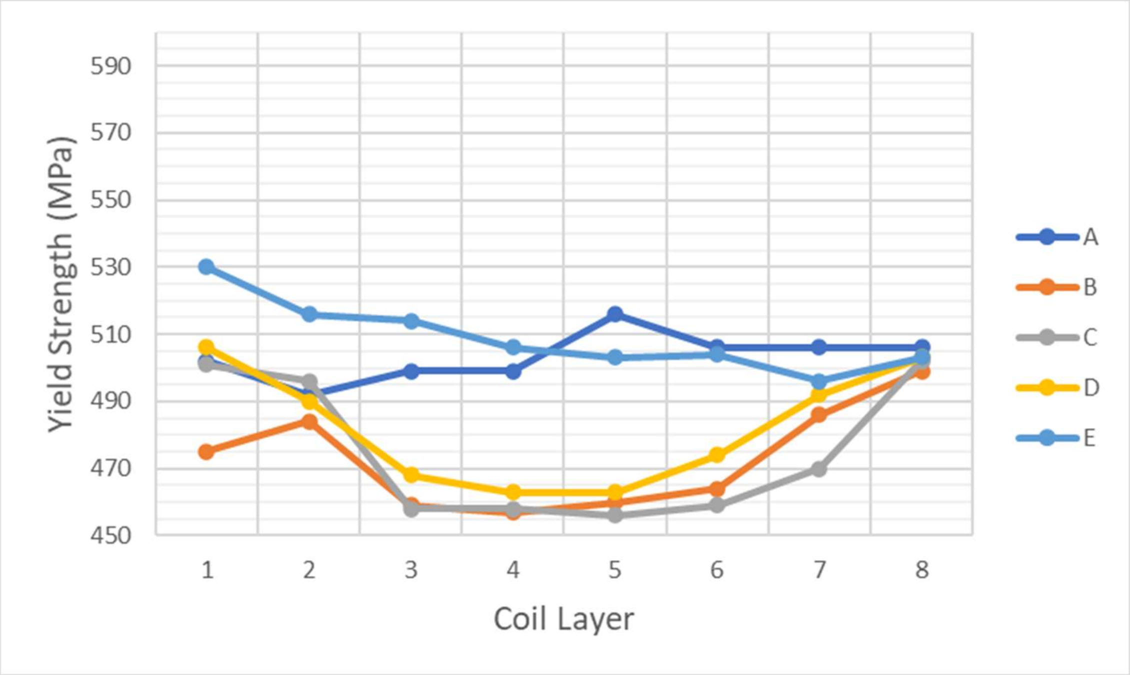

Figure 3.9 Graph showing yield strength through a coil for individual heights in CM094658, a 12 mm coil produced in 2014.

The graph in Figure 3.10 is produced from cast CM096910, on strand 1. The rebar rolling mill has two strands to produce two rebar coils simultaneously from the same billet. The coil in figure 3.11 was produced alongside the coil shown in figure 3.10, it is from the same billet but produced on strand 2. Comparing these two graphs could highlight differences between the two strands which may be causing them to perform differently during customer processing.

The same trends of high strength at the ends, and lower strength in the middle layers of the middle heights are evident in the strand 1 coil from cast CM096910, as shown in Figure 3.10. The top and bottom heights are stronger than the middle, although they are stronger towards the outer layer. Height A increased from 517 MPa to 544 MPa at the outer layer. One recorded point in the middle of the coil, D4, had a yield strength of 482 MPa which is just below the 485 MPa minimum. This may mean some of the coil has to be downgraded or scrapped.

The coil produced from cast CM096910 on strand 2 shows similar trends to the corresponding coil produced on strand 1, shown in figure 3.11. Strength is greater in both the top and bottom heights and the inner and outer layers. Also, the lowest strength is at the same point, D4, and the value here is 475 MPa, which is also below the minimum requirement. The greatest strength is 574 MPa at the top of the inner layer for E1, this is stronger than the greatest value in strand 1. So, there is similarity between the coils, but some values are greater in strand 2 while some are lower. These coils show no clear, consistent difference between the strands.

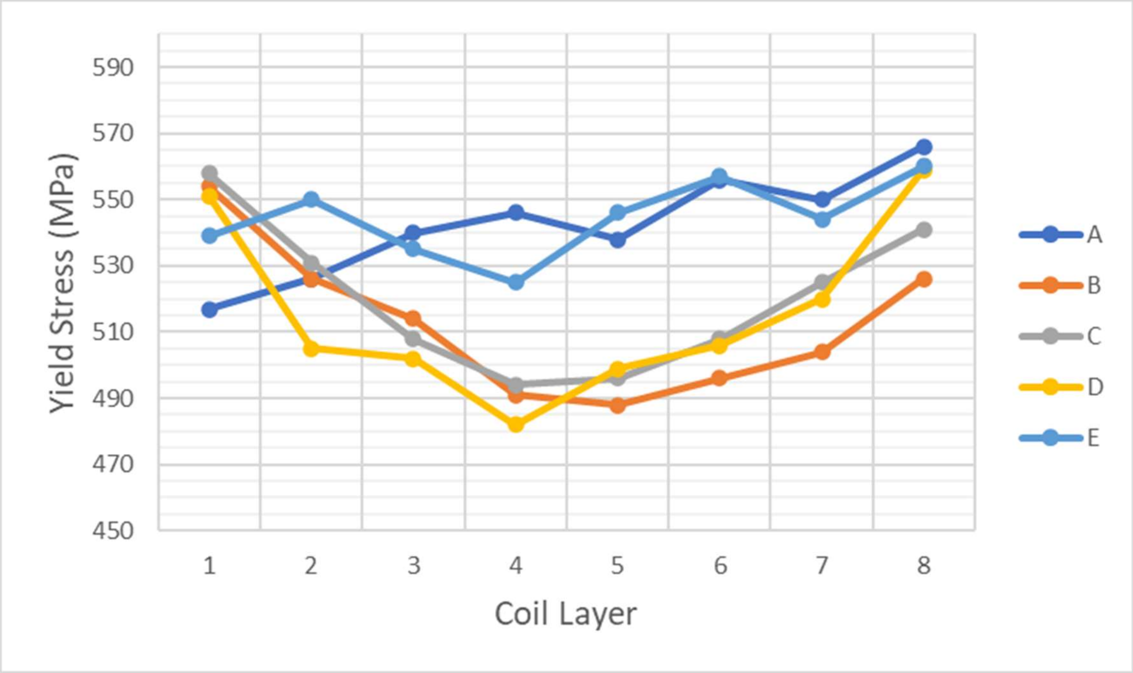

Figure 3.10 Graph showing yield strength through a coil for individual heights in CM096910, coil number 15E1721 Strand 1, a 12 mm coil produced in 2015.

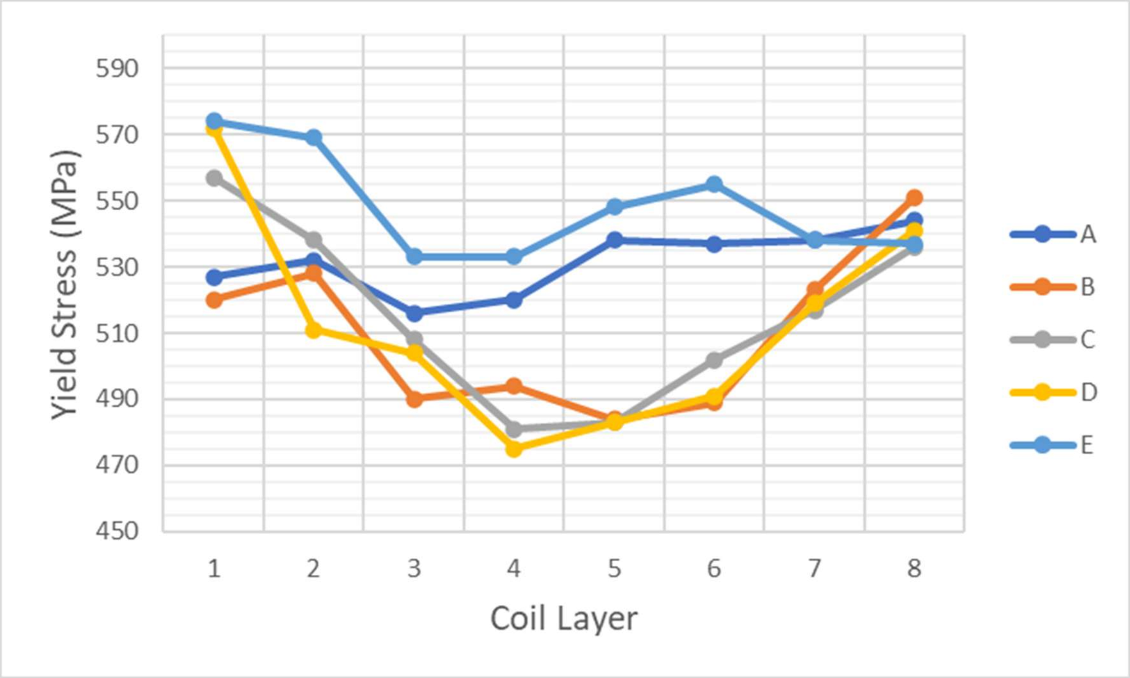

Figure 3.11 Graph showing yield strength through a coil for individual heights in CM096910 coil number 15F088005 Strand 2, a 12 mm coil produced in 2015.

In figure 3.12, the two heights which have greatest yield strength are the top and bottom, except for A1 and A2 which fall below the middle heights. Middle heights also have high strength in the inner and outer layers, close in value to the top and bottom heights, approximately 550 MPa. Strength ranges by 86 MPa, from 494 MPa to 580 MPa. The coil in figure 3.12 is produced on strand 1 from cast CM096395 and the coil shown in figure 3.13 was produced from the same cast on strand 2. Therefore, comparison between these could highlight differences between the strands as most other factors are controlled as strands run simultaneously and have the same line speed and furnace temperature.

Figure 3.13 shows a coil produced from cast CM096395, the same as figure 3.12, but through strand 2. Like many of the other coils, yield strength is greatest at the top and bottom, as well as the inner and outer layers of the middle heights. The middle heights show a U-shape, although there is not much increase from the middle to the inner layers of B and C. Like strand 1, the strand 2 coil also shows a reduction in strength in A1. The coil in strand 2 ranges from 503 to 590 MPa, a range of 87 MPa, which is very similar to that of the strand 1 coil, which is 86 MPa.

Both strands produced coils which vary widely between heights in the inner layer but are more consistent across the heights in the outer layer. This does not match the two coils from CM096910 where one coil had a closer range in values in the first layer. Both pairs show similar properties between the strands as they have similar ranges and maximum and minimum strength at similar locations, although there are differences, most significantly in the first layer.

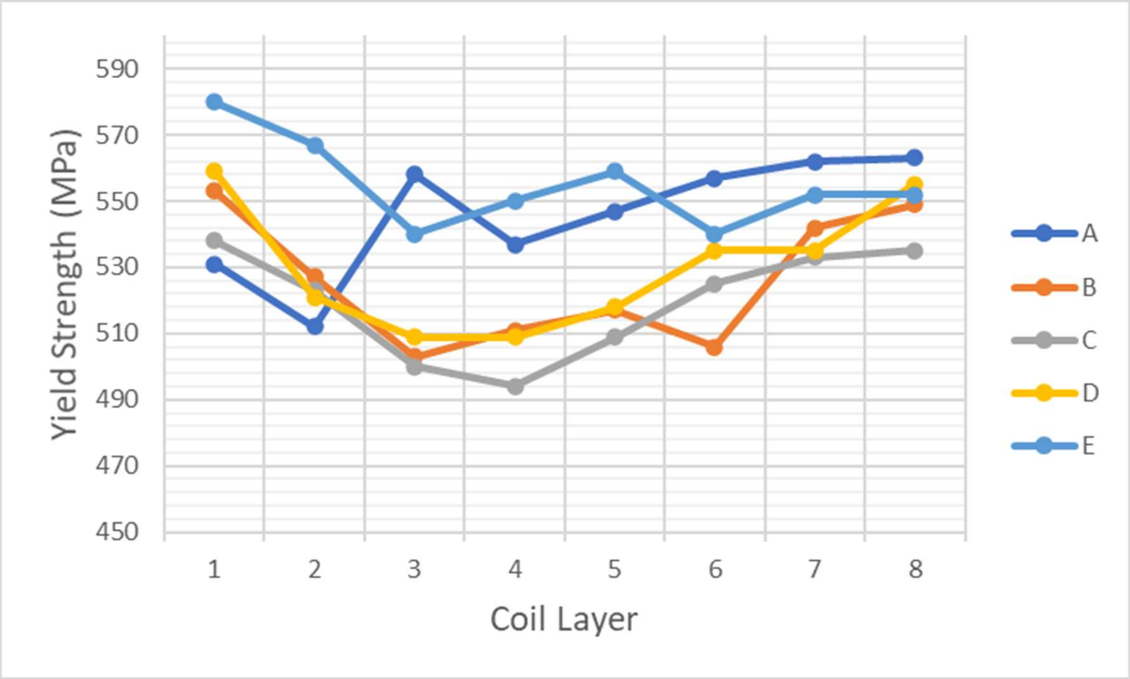

Figure 3.12 Graph showing yield strength through a coil for individual heights in CM096395 14E079731 Strand 1, a 12 mm Coil Produced in 2014.

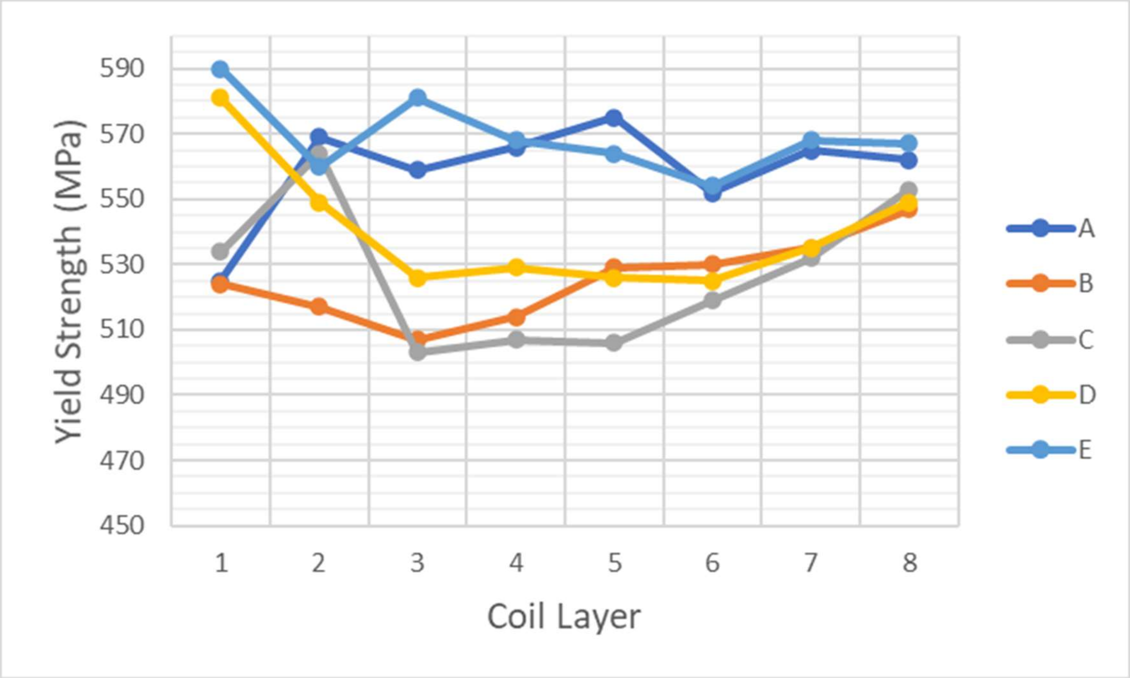

Figure 3.13 Graph showing yield strength through a coil for individual heights in CM096395 14F086018 Strand 2, a 12 mm coil produced in 2014.

To examine the variation between coils, all ten coils from the study are compared in figure 3.14. The CM096912 coil is the coil shown in figures 3.2 - 3.4, this coil has the most defined U-shape and greatest difference between the edge and middle heights of all the coils. Seven of the coils have an oscillating pattern along the bar, corresponding to samples' height in the coil, although the magnitude of variation differs. On the other hand, three coils (figures 3.5 – 3.7) show much less variation and all points are within 533 – 582 MPa.

This graph demonstrates that coil CM094658 has less overall strength than the other coils. The average yield strength for CM094658 is 488.5 MPa and approximately half of the data points are below the 485 MPa minimum. The other coils are much closer in average yield strength, between 527 – 556 MPa, which is much closer to the 550 MPa target *Celsa Steel UK* aim for.

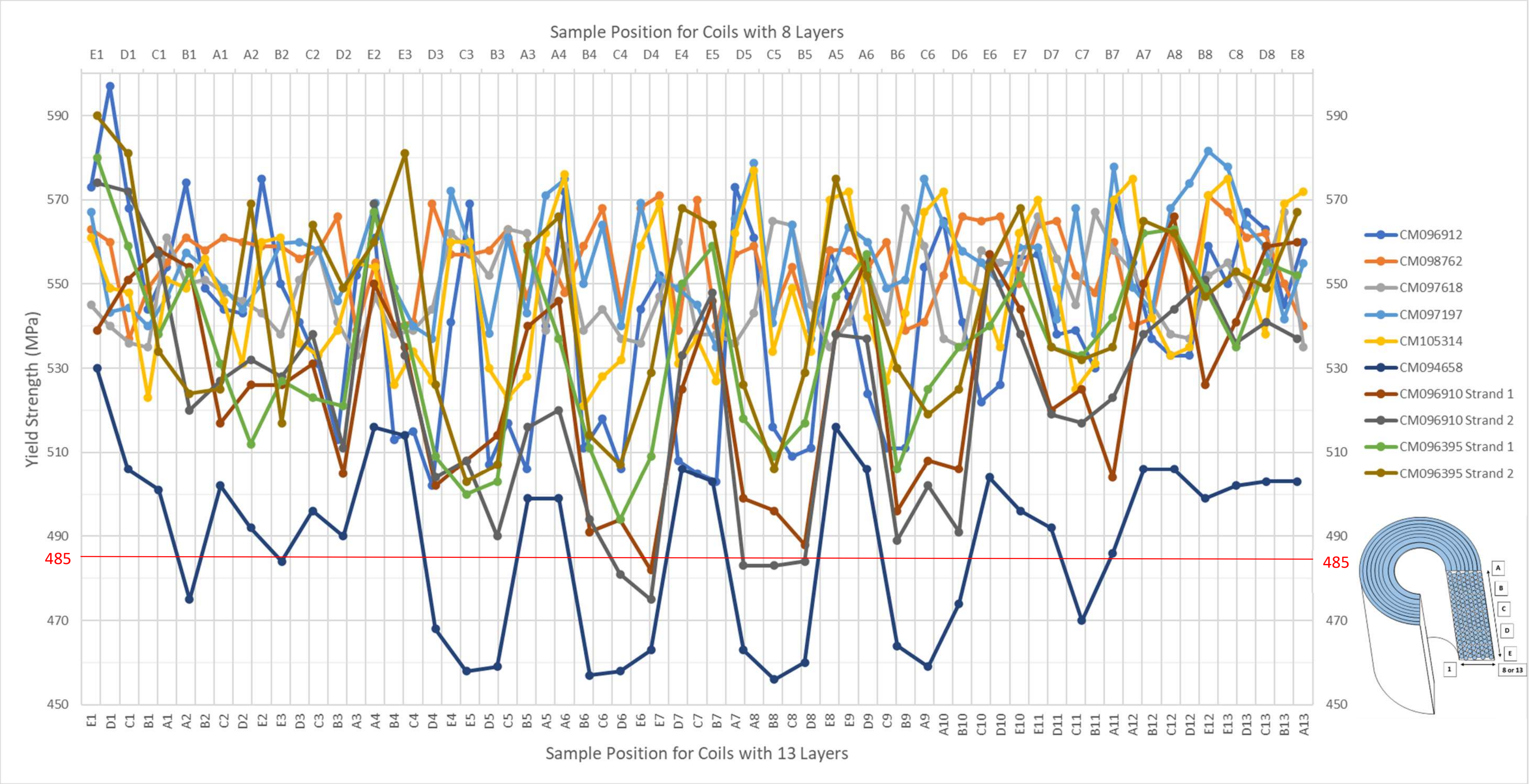

Figure 3.14 Graph comparing yield strength along all 12 mm rebar coil that have been cut up and tensile tested.

3.4 Discussion

3.4.1 Results Analysis

The hypothesis predicted differences in yield strength between coils and within coils since inconsistent processing has been reported by rebar processors both within and between coils, and inconsistent tensile strength is a likely cause of this. Some differences were expected to be random due to inaccuracy of the manufacturing process. The influence of cooling on rebar coils is unknown so strength differences between the core and exterior could not be predicted. However, it has been found that seven out of the ten coils tested have greater strength at the outer sections of the coil than the inner sections. The differences seen between interior and exterior properties are significant to rebar processing characteristics because yield strength within a coil was seen to vary by up to 19 % of the target yield strength. This indicates that the coiling and coil cooling processes have a significant effect on the steel properties as these are the only processes that are influenced by coil position.

Tensile strength in the middle heights changed through the layers. For seven of the ten coils included in the study, the middle heights have lower yield strength in their middle layers than the inner and outer layers. Another trend seen in these seven coils is that the top and bottom heights have consistent yield strength, which is greater than in the middle heights. So, the middle layers in the middle heights showed lowest yield strength, whereas the inner and outer layers at all heights, as well as all layers at the top and bottom heights had the greater yield strength. Strength in the core was lowest and all external faces had the highest yield strength.

Conversely, three coils in the study show a random distribution of strength between all layers and coils. The remaining three out of the ten coils studied show more consistent yield strength and no relationship between layers or height. The closer range of values in these randomly distributed coils shows that they have more consistent tensile properties. Therefore, the process which creates the relationships seen in the seven other coils must not occur for these coils.

Variations were also seen between coils which show the same patterns. Differences in yield strength between coils are evident in figure 3.14, in addition to the variations seen within individual coils. The average yield strength of coils varies by 67 MPa, between 489 and 556 MPa. While many of the coils have different average yield strength values, the coil with cast number CM094658 has significantly lower yield strength than all the other coils. In this coil, 42.5% of the data points measured were below the 485 MPa minimum requirement for BS4449:2005 [11]. Therefore, this would have needed to be scrapped and the process conditions which led to this coil becoming too weak should be identified and avoided.

However, the causes for these changes in overall strength are not known because process settings and conditions are no longer recorded. Variations between coils are likely to be changes to the process conditions and settings. To improve consistency between different coils, the optimum conditions could be better defined, and methods of control could be improved. On the other hand, the variation seen between the coils, except for CM094658, is not likely to affect processing detrimentally since most coils are processed without difficulty and the variations were seen in 70% of the coils studied.

Two pairs of coils are not enough to reliably identify differences between the two strands, but these were the only pairs of cut up report available. These reports are still useful in identifying differences between coils and they match the trends seen in many of the other coils. If better understanding of the effects of the two strands is needed, more cut up reports of coils produced simultaneously could be collected. However, the two pairs seen do not suggest any significant differences in the two process conditions.

3.4.2 Relevant Literature

Changes in cooling at different sections of the coil is a potential cause of lower internal yield strength compared to external sections of coil. The outer sections are likely to have faster cooling rates because they have more exposure to ambient air and are less surrounded by hot steel, creating a greater temperature gradient at the steel surface. On the other hand, the surface of sections in the core of the coil are surrounded by neighbouring layers of hot steel so the temperature gradient is much less, and cooling occurs more slowly. Reduced cooling time gives less time for grain growth to occur and may increase the effect of mechanisms such as grain boundary strengthening and precipitation strengthening. Also, after the rebar has been quenched and coiled, the steel self-tempers as heat from the centre of the diameter transfers to the quenched outer layer which has formed martensite. Greater tempering effect might occur in the middle of the core as this section cools more slowly. This would result in the middle becoming more ductile and further lowering the yield strength. The exact effect of cooling and tempering rates depends on many factors such as initial temperature, composition, and stress conditions. In most cases, faster cooling rate is expected to increase yield strength for a low carbon steel. Therefore, yield strength is expected to increase closer to the exterior of the coil, due to a faster cooling rate at the exterior.

The U-shaped strength relationship seen in the seven coils replicates results found in studies of flat sheet coils. Patel and Wilshire tensile tested a commercially produced Nb-HSLA strip steel coiled produced with a finishing temperature of 865 °C, coiled at 650 °C. Their results found that yield strength was 40 MPa higher at the inner and outermost layers. These stronger coil-ends were found to have finer grain size and increased dislocations and secondary precipitation components, which is evolution of the existing precipitates. Tensile strength across the width of the 1.2 m wide strip coil was also tested for the same finishing and coiling temperature. This is equivalent to the strength variations between heights in a rebar coil and both results concur. Patel and Wilshire found yield strength at the edges was 40 MPa greater than in the middle of the width. According to Patel and Wilshire, the higher strength at extremities of the hot-rolled coil were due to rapid cooling of the inner and outer layers, and the top and bottom edges, during coil cooling which results in finer grain size and fine precipitation. However, this explanation was for a given HSLA composition and which had not fully recrystallised prior to coiling. Rebar produced by *Celsa Steel UK* is coiled at approximately 450 – 600 °C, so less transformation will occur in the microstructure and any effect of coiling on the properties is expected to be less than in the Patel and Wilshire study [68].

Jacolot et al. recorded the temperature across a coil of steel strip as it cools using a thermal imaging camera and showed that the external layers cool faster than the middle layers, with the temperature difference across the coil reaching up to 150° [62].

Jacolot et al. also used finite element modelling to predict the differences in cooling rates and resulting pearlite grain size and niobium precipitation hardening through a coil of flat sheet steel. The model calculates cooling and grain size along the edge, quarter, and middle axis. It shows the edge has consistent grain size whereas the axis a quarter of the width from the edge shows increasing grain size towards the middle of the coil and the middle axis shows even greater increase towards the middle of the coil length [62]. Therefore, this report supports the results of the *Celsa Steel UK* cut up reports. Both reports show consistent strength along the edge (top and bottom heights), whereas the middle height of the coils show a reduction in strength towards the middle layer.

Chashchin studied controlled cooling of high carbon structural steel coils which have structural property differences responsible for 10% of the metal from the coils having to be scrapped. Analysis of experimental data for the high carbon structural steel showed that the temperature difference between inner and outer layers of the coil could reach 150 – 280 °C. By annealing metal samples, Chashchin established the dependence of hardness on the differences in cooling paths shown between the inner and outer turns. The results confirmed the need to improve the process after removal of the coil from cooling, and to develop improved methods of controlling coil cooling to achieve more consistent annealing. However, the sheet coil in this study had a high coiling temperature, 800 – 860 °C, whereas the rebar is wound by *Celsa Steel UK* at approximately 450 – 600 °C. This means cooling is likely to have less impact in the rebar coil than in the study by Chashchin, because phase changes are less likely to occur, and hardening mechanisms will occur less [67] .

Park et al. developed a finite element model for the equivalent thermal conductivity of layered steel strips and validated the calculated results with experimental data. This model showed that external regions of the coil had lower temperature after one hour of cooling than internal regions. This supports the theory that the coil does not cool uniformly. However, this model is for a steel strip coil, not a rebar coil. Equivalent thermal conductivity between layers of rebar in a coil, both in the axial and radial direction, would need to be developed to apply this model to rebar coil cooling [64].

The theory of cooling differences relating to coil position appears to be a suitable explanation for strength inconsistency but does have limitations. It explains the cause of both trends, both the differences between layers and between heights. However, three of the ten coils studied showed no difference between exterior and interior sections as all sections were within a closer range of strength values than in the seven other coils. Differential cooling may not explain the reason for differences between separate coils. The reason for the three coils having consistent yield strength is not known and could support the differential cooling theory or contradict it.

An alternative possible cause for greater strength at the start and end of the coil is that the bar is under tension as it is pulled through the product line. This could make the bar thinner in the middle or work hardening could increase strength of sections under greater tension. For example, at the start of coiling, the bar is pulled around the coil. Once enough turns are created, the bar is released and continues to wrap around the spool without the need for guidance. Tension could be greater during the initial pulling stage and reduce once the guidance is released. However, this tension could increase or decrease the rebar’s strength, depending on steel temperature and composition when undergoing the tension and the magnitude of the effect is unknown. Furthermore, this theory does not explain the consistent strength in top and bottom heights, it only attempts to explain the strength development between inner, middle and outer layers seen in the middle heights.

During production, when the steel bar is quenched, a second quench box initiates flow of water quenchant after the first 200 m of a coil has passed. This is required to account for the cooling effect the first layers of steel experiences when it encounters the colder metal surface of the spooling machine. The rest of the steel does not experience this increased cooling effect so requires more cooling from quenchant to have the same cooling path. There are potential limitations and errors caused by this second quench technique which may cause some of the strength discrepancies seen as it is a complex process that must operate at fast production rates with precise timing. If the second quench starts too early, a section of steel will experience both the cooling effect of the second quench and the cold spool surface. If it starts too late, then a section will not experience either of the cooling mechanisms so may cool more slowly and be weaker. Also, the cooling effect of the spool will have a smaller effect on the on the layers immediately after the first layer, so the quench box should start with a tapered flow rate as the spool cooling tapers off. Achieving the required flow rate would be very challenging to complete accurately. For example, in figure 3.4, D1 has a higher yield strength and UTS than the other points close to it, this could be because the spool was not an even temperature, or the second quench began here before the spool cooling effect had reduced.

3.4.3 Potential Manufacturing Solutions

Models and studies suggest that different processing parameters can affect the homogeneity of coil properties, including tensile strength. Influential processing parameters include rolling and finishing temperatures. Patel and Wiltshire found that for Nb HSLA steel strip coils, a finish rolling temperature close to, but above the austenite to ferrite transformation temperature with a coiling temperature of 600 °C improved consistency both along the coil length and across its width, and this coiling temperature increased yield strength [68] . Differences in parameters such as these could be the cause of the more consistent coils that has been seen in three of the *Celsa Steel UK* coils in this study. These parameters could be investigated to find optimum conditions for homogenous coil properties.

Chaschin has shown that thermostatting reduces the temperature gradient between the outer and inner layers of a structural steel strip coil, equalizes cooling rate and yields uniform hardness, within permissible limits, over the whole strip length. Thermostatting is the term used to describe controlled slow cooling of hot-rolled strip in coils. Experimental and analytical results are used in the study to demonstrate the effect of thermostatting. The rate of cooling is determined by the value of the middle turns and remains a relatively high productivity method of hot rolling. Since the high temperature stage is regarded as the most significant to structural changes, the thermostatting process can be used for this stage and the coils can be removed from the thermostat for the low temperature stage of cooling to minimise cooling duration. Although this study uses a different chemistry and product, thermostatting is a potential method to improve the heterogeneity within rebar coils [67].

A method of coating the outer surfaces of strip coils with an insulating spray to reduce the heat transfer and emissivity at the coil surfaces has been patented by Chaschin et al. This reduces the cooling rate in the outer sections so that they cool at a closer rate to the rest of the coil and mechanical properties are more consistent. The spray is designed to be applied to coils which are cooled inside a thermostat [69] .

Variable quenching is another potential method to improve heterogeneity of the coils' mechanical properties. A second quench box is currently initiated after the first 200m of a coil which demonstrates the production ability to vary quench flow according to section of the coil. Therefore, the quenchant flow rate could be increased for sections of rebar that will be positioned in the middle of the coil. This increased quench cooling could counteract the reduced cooling rate these sections experience in the middle of the coil. The process could be refined to produce uniform tensile strength throughout the whole coil. This technique would be simpler for flat strip coils as flow rate can be increased towards the middle, then gradually decreased towards the end. However, for a rebar coil with multiple turns per layer, the flow would need to change more frequently to reduce flow on sections that will be at top and bottom heights, as well as the inner and outer layers. This could be very challenging at high production rates. Also, while yield strength could be matched between sections, the microstructure would differ as some sections have more martensite or are self-tempered at different rates. So, other mechanical properties, such as ductility would be inconsistent.

3.4.4 Evaluation

Data from Celsa quality testing has been used to identify relationships between discrepancies in tensile strength in coils. It was found that seven coils show similar patterns in strength relating to coil position. Three coils produced in 2015 were found to have no discernible relationship between tensile strength and coil position. Factory process parameters are no longer retained from 2015 so any conditions which were unique to the three consistent coils and may be key to replicating this consistency cannot be investigated. Further coil cut-up studies should be undertaken, and processing parameters should be recorded to investigate causes for the relationships appearing in certain coils and not in others. Parameters to record include line speed, temperatures at each stage of the process, ambient temperature, and any conditions that are currently measured during production but not recorded.

Relationships between coil position and tensile strength have been proven to exist, but the sample size is not large enough to be able to predict the percentage of coils that are produced with the relationships that have been seen. To increase reliability, further coil tests can be run, and the number of samples taken per coil can be increased.

Manufacturing solutions have been suggested based on literature and theoretical causes of the tensile variation. However, the cause should be identified through further testing before these manufacturing solutions are developed. Experimental testing could then be used to identify optimum factory conditions and the effectiveness of potential process improvements.

3.5 Summary

- Increase in tensile strength towards exterior sections of the coil, both inner and outer layers and bottom and top heights occurs in seven of the ten coils included in the study. This may be the cause of some rebar processing tolerance issues.
- Differences in cooling in different sections of the coil could be a cause of the increase in tensile strength at exterior sections.
- Three of the ten coils studied did not show a relationship between coil position and tensile strength.
- Variations are also seen between different coils as the average yield strength of the ten coils in the study varies between 488 and 556 MPa.

Variations in tensile strength within coils may be a cause of certain tolerance issues that are experienced when post processing Celsamax coils to create reinforcing structures. Changes in tensile properties relating to coil position have been seen within coils through the analysis techniques implemented in this study. Tensile strength is often greater closer to exterior sections of coils included in the study. The largest change in tensile strength found within a coil was 95 MPa. Strength changes of this size are expected to cause rebar processing issues because processing machines will require constant adjustment to produce consistent products when properties vary by this magnitude. For example, rollers are used to straighten rebar as the coil is unravelled and the pressure exerted by these rollers is adjustable. If roller pressure is too low, the rebar retains some curvature from the coil and is not straight enough. Yet if roller pressure is too high, the bar is over-straightened and develops a curve in the opposite direction to the coil curvature. The amount of pressure required may depend on the strength of the rebar. Therefore, if the strength frequently changes by a significant amount, frequent adjustment would be required to produce consistent dimensions. This adjustment slows the rate of processing and can result in coil sections which take too long to process and must be scrapped. Processors have reported scrapping entire two tonne coils that were not financially viable to process because they required too much adjustment. If the change in processing is not detected or the required adjustment is not made, the product will have less accurate dimensions and may exceed dimensional tolerance limits.

The increased strength towards exterior heights, as well as exterior layers, makes strength changes along the bar as the coil is unwound difficult to predict. This can be seen in figure 10 where each coil oscillates at constantly changing amplitudes and frequency. Consequently, a predictive adjustment technique for the processing machines could be challenging to create and would likely increase machine cost and processing time.

To improve consistency of all coils, the process conditions of more consistent coils, such as the three consistent coils in this study, are valuable indicators of optimal production conditions. However, these coils were produced in 2015 and records of production parameters are no longer available for coils produced in this year. Instead, coil cut ups should be continued in the future, with the analysis techniques shown in this study, and process parameters should be recorded and compared to each coil. Any conditions which are unique to coils with more consistent properties could indicate the key parameters to control for higher consistency coils for easy processing.

Chapter 4 Characterisation of Samples

4.1 Experimental Procedure

4.1.1 Material Supplied by *Celsa Steel UK* and Express Reinforcements

Celsa Steel UK and Express Reinforcements, a customer of *Celsa Steel UK*, provided samples of 12 mm diameter reinforcing steel which had been processed and displayed unique properties during processing. Three samples supplied by Express reinforcements and one sample from *Celsa Steel UK* were characterised in this project. A sample of reinforcing steel which had been processed without excessive need for adjustments was used as a control sample in this study. The other two samples from Express Reinforcements performed differently to each other when they were processed together in an ALB machine that can process two coils simultaneously. Finally, the sample from *Celsa Steel UK* had been returned from another customer who reported the coil had frequently twisted when it was bent, producing parts with out of plane bends.

The pair of samples from Express Reinforcements were processed simultaneously on a twin strand ALB machine which can process two bars simultaneously, as described in section 2.3. These two coils were straightened and pulled by drive rollers to a distance where a bend or cut needed to be made. One of the coils would consistently be pulled through the machine further than the other. This would result in one coil producing parts with greater length than the other. This is a common issue Express Reinforcements experience and results in the coils being processed individually, rather than simultaneously, which halves the rate of production.

Celsa Steel UK supplied a sample from a coil which had been processed by another rebar processing company and was reported to frequently twist as it was straightened and processed. Twisting is also a possible cause for out of plane bending which is described in section 2.3. If rebar twists where a bend is made, the bar may deform perpendicular to the bending plane. Twisting and out of plane bending has been reported by multiple rebar processors and has been reported to occur throughout entire coils as well as sections of a coil. It is not known if the sample supplied by *Celsa Steel UK* contains the property causing the twist since it is a small section and twisting may not occur throughout the whole coil. However, the entire coil could not be tested as this would not be feasible for the project and most of the coil was used to produce reinforcement structures. So, the sample provided will be tested to look for the presence of unique properties that are potential causes for twisting and out of plane bending.

Table 4.1 shows the four samples that are characterised in this section. Each sample has a unique cast number to describe the cast batch in the EAF process that the coil was produced from. The cast composition for each coil measured by *Celsa Steel UK* using optical emission spectroscopy is also shown in table 4.1. For this study, each coil is assigned a sample number. Sample five is the coil which performed as expected. Samples six and seven are the pair which were drawn through an ALB machine simultaneously; six would be pulled a shorter distance than seven. Finally, sample eight is the sample from a coil that displayed twisting.

Identification			Celsa Cast Composition (Wt%)																	Mn/S Ratio
Cast Number	Sample Number	Processing Characteristic	C	Mn	Cu	Si	Cr	S	Al	P	Ti	Ni	Pb	Sn	V	B	N	Mo	C Eq	
CM128294	5	Control	0.191	0.873	0.497	0.139	0.166	0.032	0.001	0.031	0.001	0.125	0.003	0.045	0.002	0.0000	0.010	0.018	0.415	27.281
CM130131	6	Twin Strand, Shorter	0.181	0.866	0.365	0.138	0.124	0.028	0.001	0.024	0.001	0.147	0.002	0.029	0.002	0.0002	0.147	0.025	0.390	30.929
CM130134	7	Twin Strand, Longer	0.179	0.858	0.417	0.137	0.130	0.029	0.002	0.024	0.001	0.130	0.002	0.028	0.002	0.0002	0.011	0.020	0.389	29.586
CM128438	8	Twisting	0.181	0.893	0.445	0.150	0.151	0.026	0.001	0.025	0.001	0.108	0.003	0.020	0.002	0.0002	0.108	0.016	0.401	34.346

Table 4.1 Identification numbers for each of the samples characterised in this study and the corresponding composition of each sample when the steel was cast. The compositions were measured by Celsa Steel UK using optical emission spectroscopy.

4.1.2 Sample Preparation

Samples were provided in straightened sections and were cut along their diameter and centrelines to produce two planes for analysis for each sample. The first plane is a cross section, perpendicular to the rolling direction, described by the letter C. This shows a full ring of quenched steel and all four longitudinal ribs around the exterior. Figure 4.1 shows the location and a prepared C sample. The second plane is along the rolling direction, named L as it is the longitudinal section. A longitudinal cut in a line of symmetry creates two even semi cylinder sections, approximately one cm of the interior face of one of these is used for the L sample. Longitudinal samples show quenched steel and any transverse ribs which were cut along the top and bottom edges. The location and a prepared L sample are shown in figure 4.2.

Each sample was mounted in 32 mm diameter conductive Bakelite to grind them safely. These were ground to 1200 grit using decreasing grades of emery paper and then polished using six, three, and one -micron water-based diamond suspension fluid to achieve a surface finish of one micron. Between each stage of grinding, samples were rotated 90° and polished until all the previous scratches were removed. Samples were washed with soap and water and dried with ethanol under a hair dryer between stages to remove particles from the previous grinding paper or polishing suspension. The polished samples were then lightly etched in a fume cupboard using five percent Nital solution for approximately five seconds to create a more visible distinction between grains. Samples were then washed with water again and dried with ethanol under a hand dryer to stop the etching process.

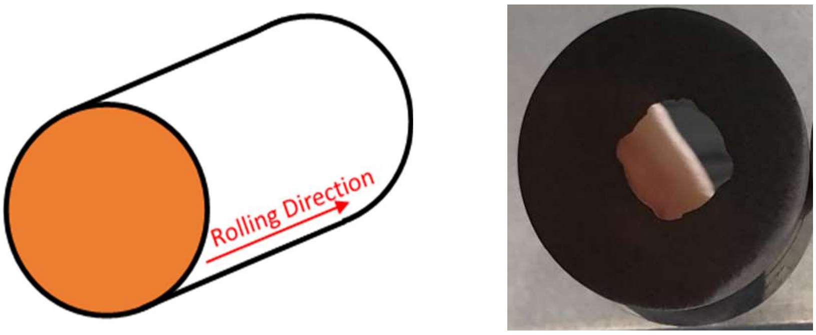

Figure 4.1 Diagram showing the area which is prepared for cross section samples (left) and a polished cross section sample mounted in Bakelite (right). The four longitudinal ribs are visible around the edge of the sample.

Figure 4.2 Diagram highlighting the area which is prepared for longitudinal section samples (left) and a polished longitudinal section sample mounted in Bakelite (right). Transverse ribs are visible along the top and bottom edge of the sample.

4.1.3 Light Microscopy

The optical micrographs produced in this study were obtained using the Carl Zeiss Axio Observer Z1M. Stitched images were acquired at 10X magnification which image an entire sample. This is a brightfield microscope with an inverted construction which reduces need for refocusing on samples which are not level. Focus correction points are also set up to refocus during stitching for sample surfaces which are not flat. Figure 4.4 shows an example of the stitched images produced for a cross section and a longitudinal sample.

The stitched images were then used with ImageJ software to measure dimensions such as diameter, aspect ratio and martensite thickness to evaluate the dimensional accuracy in the samples obtained.

4.1.4 Scanning Electron Microscopy

Electron micrographs in this research were produced using the Carl Zeiss Evo LS25 SEM for higher resolution at higher magnification than optical microscopy. Secondary electron (SE) and Backscattered electron detector (BSD) images were used to measure grain size and inclusions. Energy Dispersive Spectroscopy (EDS) was also used to acquire chemical analysis of the samples, at points and for mapped areas. The potential and current of the electron source were 20.0 KV and 500 pA respectively, working distance is between 9 mm and 11 mm. SE, BSD, and EDS were all used at 1000X magnification at the same locations in the core and quenched edge regions of all the samples. Three locations in the core of each sample were taken for increased reliability of grain and composition measurements. One location was used in the edge since grain measurements were not made for the edge region.

To obtain clear images and maximise count rate, the electron gun was aligned with the aperture and lens though gun shift and tilt, wobbler aperture alignment, and stigmatisms. Since contamination on samples can affect images and interact with the electron beam to result in carbon deposition on the area being imaged, it was highly important to prepare clean samples and wear gloves when handling samples.

BSD images were processed using ImageJ and the mean linear intercept (MLI) method to measure average grain size. A horizontal line of set length was drawn in five locations and a set length vertical line was also drawn in five locations on each core BSD image with 1000X magnification. The number of grain boundaries on each line were counted and divided by the length of the line to find the average length across each grain. All 10 lines were averaged to find a reliable value for the MLI of the image. This was repeated for three images per sample and averaged to give an MLI value for the sample. The equation to calculate MLI of grains on a line is shown in equation 4.1.

$$Mean\ Linear\ Intercept = \frac{Line\ Leng}{Number\ of\ Boundaries} \qquad \text{Equation 4.1}$$

ImageJ was also used in conjunction with BSD images to calculate the average percentage of area that is covered by inclusions. Brightness and contrast are first increased to maximise the contrast between the dark inclusions and slightly lighter grains. Since inclusions are darker than grains and most grain boundaries in BSD images, the threshold can be set to include the inclusions but cut off grain boundaries and other lighter features. A BSD image after this threshold has been applied is shown in figure 4.3 below. The percentage of coloured area is then calculated in ImageJ, and this is the percentage area of inclusions on the image. The percentage area of each sample is averaged from three 1000X magnification images in the sample core.

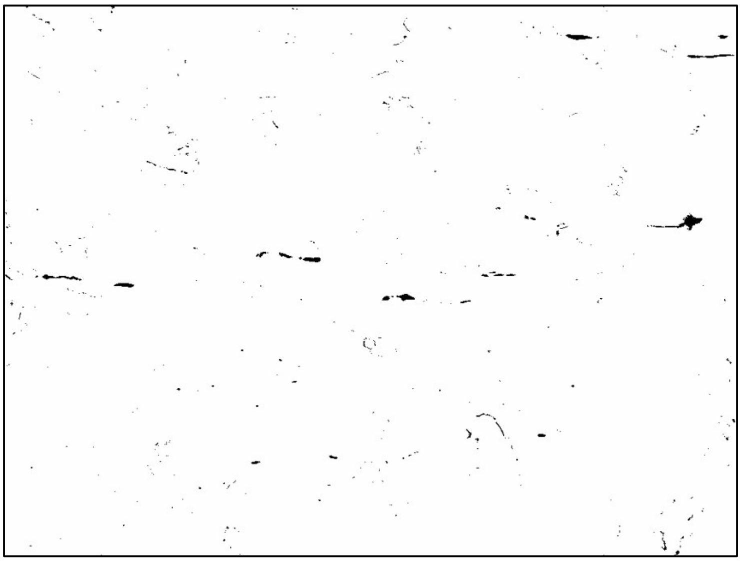

Figure 4.3 BSD image of sample 5L with threshold applied to include only inclusions. Many of the inclusions are elongated in the rolling direction, which is left to right. The inclusion area percentage of this image is 0.4%.

EDS Quantitative analysis identified elements present in both core and edge regions of each sample. After the SEM had been focused and aligned, and SE and BSD micrographs were captured, AztecLive was used to conduct EDS scans of the same area. Carbon is the major component of contamination on sample surfaces so the error for measurement of carbon proportion is much larger than other elements. Therefore, carbon was excluded from the analysis. Maps and specific points were scanned for each site that was imaged with SE and BSD detectors, to find the composition of microstructural features seen. Maps were stopped after acquiring 20 frames. Resolution was 1024, pixel dwell time was 10 µs and frame live time was 8 seconds. So, map acquisition took approximately three minutes. Point ID was stopped after 200,000 counts were reached for each point. Points were selected within grains of various sizes, in dark areas, and any other microstructural features seen [70].

4.1.5 EBSD

Electron back scatter diffraction was performed using an Oxford Instruments C Swift detector with the Carl Zeiss Evo LS25 SEM to provide further microstructural information, including grain size, crystal orientation and presence of dislocations. The interface between quenched and un-quenched steel was scanned so data could be collected for both regions. This interface location is shown by figure 4.4 for both a cross-sectional and longitudinal section.

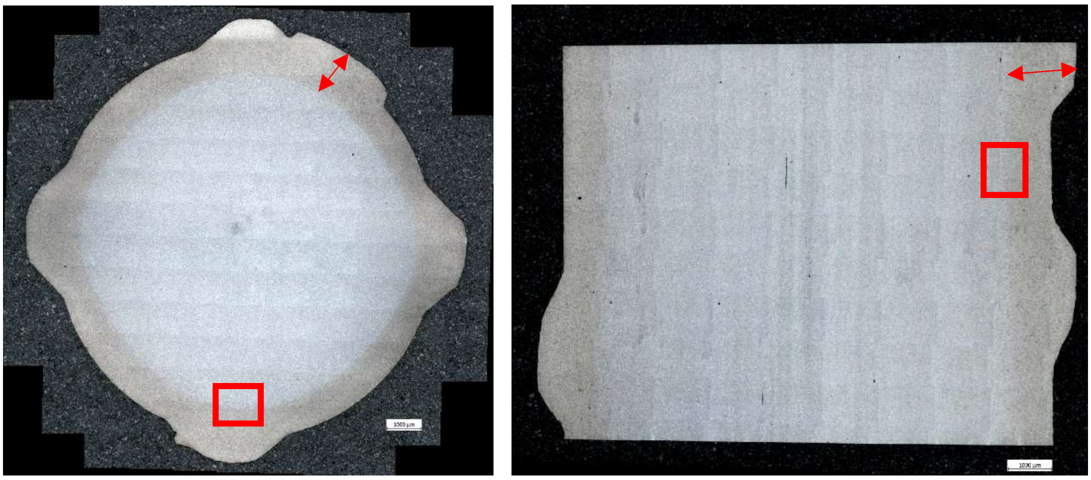

Figure 4.4 Stitched images for a cross section sample (left), and a longitudinal sample (right) mounted in Bakelite. The approximate location of EBSD scans is indicated by a red box. This includes a region of the self-tempered core as well as a region of the quenched edge. The quenched region is darker than the core and indicated in each sample by a red arrow.

Electron backscatter diffraction (EBSD) is a technique that uses an SEM to study crystallographic structures and analyse the crystal orientation, phase, or strain in the material. Prepared polished samples were placed in a vacuum SEM chamber and tilted to 70° from horizontal to increase the contrast in the EBSD pattern and reduce electron charging on the sample surface. Conductive carbon tape around the specimen held the sample in the sample holder and reduced charging and image drift. An electron beam from the pole piece was focused onto the surface of the sample so that the electrons enter the sample and cause some electrons from the sample to scatter. Some of these scattering electrons are incident on the atomic planes at the Bragg angle. A phosphate detector horizontal to the sample captures these backscattering electrons. The layout inside the SEM is shown in figure 4.5 [71].

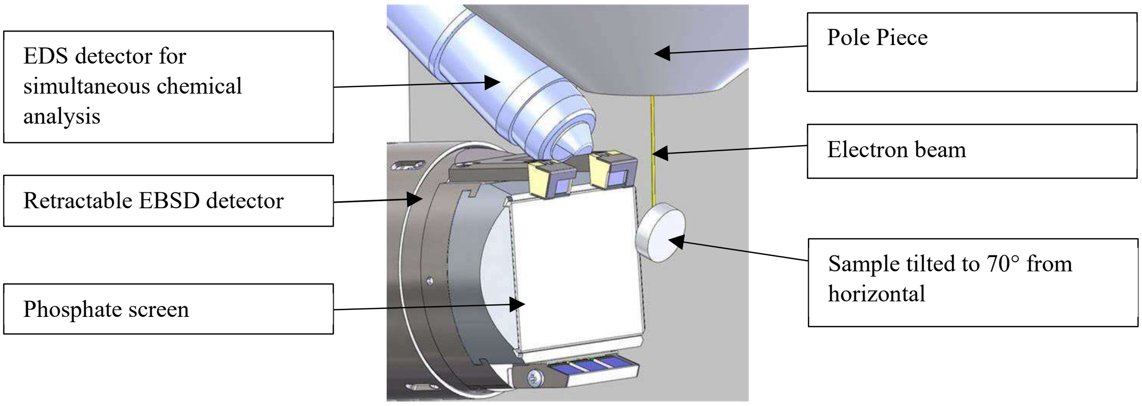

Figure 4.5 SEM chamber setup for EBSD. The sample is tilted 70° from the electron beam and an EBSD detector is inserted horizontal to the sample to detect backscattered electrons [70].

The backscattering electrons may exit at the Bragg angle and diffract to form Kikuchi bands, which are where regions of increased electron intensity intersect the screen and create patterns that correspond to specific lattice crystal planes. Figure 4.6 shows Kikuchi line patterns generated by electrons diffracting off a steel sample. The bands in the diffraction pattern were indexed using the Hough transform. A Hough space converts each line in the diffraction pattern to a unique point. These Hough points are easier to detect computationally than the original bands. Once detected, the band locations indicate the crystal orientation since angles between the bands represent angles between lattice planes. When the angles between at least three bands are known, the lattice orientation can be solved. At least six bands were used to reliably differentiate between most structures in this study.

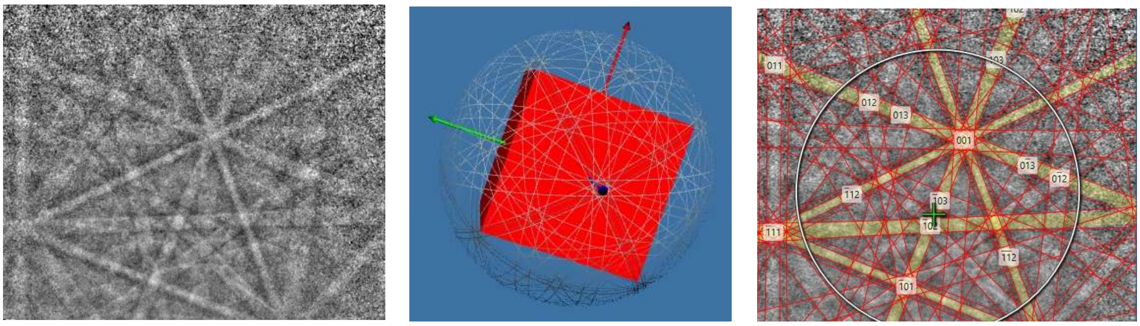

Figure 4.6 Live Kikuchi band pattern of electrons formed by back scattering from a single crystal structure (left), a 3D model of the equivalent orientation of a body centred cubic crystal lattice (middle) and an indexed pattern matched to the Kikuchi pattern (right).

Zeiss SEM software was used to setup the microscope before AZtecLive was used to conduct EBSD scanning and AZtecICE processed the resulting data [70]. Once a sample was loaded in the chamber, a vacuum was created to remove interference. The sample was tilted 70° to increase the contrast in the EBSD pattern and reduce electron charging on the sample surface. To focus on a tilted surface, dynamic focus was applied with a tilt of 70°. Beam current and voltage used were 786 - 1000 pA and 20.00 kV respectively since a high number of electron counts were required and these are the maximum settings at which the SEM would operate. A magnification of 150X gives an image area of approximately 400 X 300 µm. This is a reliable image size for the samples since over 12,000 grains were included in each scan. Images scanned in this study are between 100 and 150 X magnification, which covered areas between 112750 to 766590 μm^2. The area size depended on amount of run time available for the SEM and areas were maximised to increase reliability. However, the smallest image size still included enough grains to give reliable grain analysis. Areas were mapped overnight with a speed of 30 – 120 points per second, depending on the filament condition.

The software used to set up the EBSD scan is AztecLive. For a cross-section sample, the rolling direction (RD) is set to the Z axis, towards the viewer, transverse is the Y axis and normal is the X axis. On the other hand, for longitudinal samples RD is the X direction, transverse is in the Y axis and normal is the Z axis. This means that the cross-section samples are viewed with an Inverse Pole Figure Z (IPF Z) map and longitudinal samples are viewed with IPF X. The number of Kikuchi bands required to differentiate between most orientations is six. Increasing the number of Kikuchi bands will allow differentiation between more closely related orientations but will increase computation time without a significant effect on results since six is enough to identify the predominant steel orientations. The material was set to BCC iron as this is the structure of ferrite and most of the sample.

The step size was 0.25 µm because the MLI values calculated from SEM data were between 3 - 5 µm, therefore this grain size would be capable of identifying all the grains present in the steel to a sufficient accuracy. The minimum grain diameter recorded by AZtecICE was 1.0 µm. Any grains smaller than this are an insignificant proportion of the total sample and hence do not need to be detected. Reducing the minimum grain size further would increase computation time without significantly affecting results.

When testing the image prior to scanning, mean angular deviation (MAD) was below 0.5°. This means the angular resolution between the lattice detected by the EBSD data and the indexed lattice it is matched to is ±0.5°. An orientation boundary is between two orientations that could each vary by one degree from their measured orientation. Therefore, any misorientation less than two degrees is not reliable, so is not recorded.

Working distance between the electron source and the sample site scanned was 15 – 20 mm. Since the sample holder has a diameter of 34 mm, it cannot get closer than 15 mm when tilted 70°. This distance is close enough to get precise data, but electron count rate is lower than if the sample were closer. Hence, scanning takes longer to achieve sufficient quality.

EBSD data was analysed using AztecIce software to give grain size and orientation data. A clean-up was applied to clean the data and reduce the number of un-indexed data points. Firstly, any wild spikes were removed. Next, unindexed points were extrapolated using eight of its nearest neighbouring points, followed by seven and so on until most points were indexed. Clean up was stopped before any features of the raw data were affected. Significant noise reduction was not necessary as most points in the original data were indexed.

Separate subsets are created in the tempered core and quenched regions to analyse these regions individually. Each subset is 24,000 – 219,000 µm² and includes 3,000 – 27,000 grains, depending on the original image size. The smallest subsets include enough grains to produce reliable data. When prolonged SEM access was available, such as over weekends, or greater points per second could be achieved, such as when the filament was replaced, image size was increased to further increase the reliability and number of grains for analysis.

For grain analysis, grain boundaries were defined as a misorientation of greater than 10°. The average grain size was calculated from the equivalent circle diameter (ECD) of each grain. ECD is the diameter of a circle that has the equivalent area to the grain being measured. Grains with ECD less than one µm were removed since the step size was 0.25 µm, so grains this size could not be accurately measured. Any un-indexed points which had not been extrapolated by the clean-up were also removed from the data set. Grain size statistics were gathered in this way for the ferrite and martensite subset of each sample.

Band contrast images were produced to show the map quality and microstructural features. IPF maps with grain boundary lines were also created to visualise texture. IPF Z presents orientation in cross sectional samples where rolling direction is in the Z axis. Whereas IPF X presents orientation in longitudinal samples where rolling direction is in the X axis. Major grain boundaries show misorientations greater than 15° while minor boundaries show misorientations of 5° – 10°. Inverse pole figures were used to describe the texture of the steel, Z for cross sections and X for longitudinal samples. Kernel Average Misorientation (KAM) maps were generated to show local misorientations. The KAM value for each point was calculated from its average misorientation with all surrounding points in a 3 X 3 square that are below 5°. Local misorientations are caused by deformation so a high concentration of misoreintations indicates a region that has experienced deformation and may contain residual strain.

4.1.6 Microhardness Testing

Hardness testing was performed using an Innovatest Nexus 4303 Vickers hardness tester with a load of 5 kgF for a dwell time of 10 seconds. This load is applied at points one millimetre apart along a linear line, starting 0.5 mm from an external edge. For longitudinal samples, these lines are perpendicular to the external, quenched edge, and five lines of hardness tests were completed. In cross sectional samples, each line intercepted at the middle causing the central points to be less than 1 mm apart. This means the first indent could have work hardened the area and affected the subsequent indent results. Therefore, only three lines were used for each cross-sectional sample to limit this effect and the results for the L samples are considered more reliable.

4.2 SEM Results and Analysis

4.2.1 EDS Results and Analysis

The composition of each sample was measured for both the cross and longitudinal sections using EDS sum map analysis. Since the compositions measured by Celsa, shown in Table 4.1, are measurements of a sample from the whole cast, EDS analysis of each sample in this study was conducted to identify the composition at the specific location being studied. The composition of a map was summed to find the mass fractions of each element in the whole map. The average of three core maps was calculated for each sample to better represent the whole material. The average composition and standard deviation of all samples were then calculated from the results.

Sample Composition	Composition (Wt%)								
	Fe	Mn	Cu	Si	Cr	S	Al	P	Mo
5C	98.0	1.0	0.5	0.2	0.2	0.1	0.0	0.1	0.0
5L	97.9	1.0	0.6	0.2	0.2	0.1	0.0	0.0	0.0
6C	98.6	1.0	0.4	0.2	0.2	0.0	0.0	0.0	0.0
6L	98.3	0.9	0.4	0.1	0.1	0.0	0.0	0.0	0.1
7C	98.3	0.9	0.4	0.2	0.1	0.0	0.0	0.0	0.0
7L	98.3	1.0	0.4	0.2	0.1	0.0	0.0	0.0	0.0
8C	98.1	1.0	0.5	0.2	0.2	0.0	0.0	0.0	0.0
8L	98.1	1.0	0.5	0.2	0.2	0.0	0.0	0.0	0.0
Average	98.2	1.0	0.5	0.2	0.2	0.0	0.0	0.0	0.0
Deviation	0.2	0.0	0.1	0.0	0.0	0.0	0.0	0.0	0.0

Table 4.2 Composition results of EDS map sum analysis of all samples. The samples are all low alloy and consistent with each other. The additional elements with greatest mass fraction are manganese and copper.

Table 4.2 shows that the composition measured in each sample is relatively consistent between samples. Standard deviation is less than 0.1 for all elements except Fe and Cu which are 0.2 and 0.1, respectively. Manganese is the additional element with greatest mass fraction while Cu, Si, Cr and S are found in all samples. P and Mo are also seen in sample 5C and 6L, respectively, with 0.1% mass fraction. These could be contaminants on the sample surface as they are very small amounts and not repeated in 5L and 6C.

Material five has slightly higher mass fractions of copper and sulphur than the other materials. Samples 5C and 5L have 0.5 and 0.6 wt% C, respectively and both contain 0.1 wt% S. Another difference between materials is that material seven contains 0.1 wt% Cr whereas all other samples contain 0.2 wt% Cr. Material five showed heterogenous processing characteristics so these changes are unlikely to be detrimental. However, it is possible that the lower values contained in the other samples caused inconsistent processing.

Procces Stage of Analysis	BS4449:2005 Composition Limits (Wt%)					
	Cu	S	P	N	C	Carbon Equivalent
Cast Analysis	0.8	0.05	0.05	0.012	0.22	0.5
Product Analysis	0.85	0.055	0.055	0.014	0.24	0.52

Table 4.3 Composition percentage limits by mass for rebar defined by the British Standards BS4449:2005, which rebar produced by Celsa Steel UK is required to meet [11]*. Cast analysis is measured from the steel as it is cast, product analysis is the composition of the finished rebar coil. The equation for calculating Carbon equivalent is given in equation 2.2.*

The composition limits of BS4449:2005, shown in table 4.3, are close to the mass fractions found through EDS analysis [11]. The British standard gives maximum percentages for certain elements so their actual mass fractions can be less. Elements not specified have more flexibility, although all the elements found through EDS either have specific limits or are included in the equation for carbon equivalent. Some quantities of elements seen in the EDS analysis are greater than the British Standards limits. Sample 5C has 0.1 wt% of Sulphur and Phosphorus and 5L has 0.1 wt% S. However, rounded to one decimal place, the 0.055 wt% limit for Sulphur and Phosphorus is 0.1 wt%. So, accounting for the accuracy of the EDS technique, the amounts seen may be within the acceptable limit.

Copper is a common contaminant of recycled steel, the main source of iron in the *Celsa Steel UK* steelmaking process. The average mass fraction of copper found 0.5 wt% with 0.1 standard deviation. This is below the British standards limit of 0.85 wt% in all samples so copper is sufficiently controlled in the EAF process.

Since carbon is not included in the study, subtracting the maximum carbon limit from the carbon equivalent equation gives a limit for the remaining elements. This new equivalent limit for the final composition is 0.28 wt%. Equivalent calculated from the EDS results was between 0.21 and 0.25 wt% for all samples, which is below this limit.

Identification			Celsa Cast Composition (Wt%)						
Cast	Sample	Processing	Mn	Cu	Si	Cr	S	Al	P	Mo
CM128294	5	Control	0.873	0.497	0.139	0.166	0.032	0.001	0.031	0.018
CM130131	6	Twin Strand, Shorter	0.866	0.365	0.138	0.124	0.028	0.001	0.024	0.025
CM130134	7	Twin Strand, Longer	0.858	0.417	0.137	0.130	0.029	0.002	0.024	0.020
CM128438	8	Twisting	0.893	0.445	0.150	0.151	0.026	0.001	0.025	0.016

Table 4.4 Mass fractions measured by Celsa Steel UK during casting of steel for the four coils tested in this study. The mass fractions shown are for the additional elements that were found during EDS analysis of the samples. The full composition of each cast is shown in table 4.1.

The composition measured by *Celsa Steel UK* during casting for each of the four coils included in this study, shown in table 4.4, have similar values to the results from EDS analysis. The *Celsa Steel UK* measurement is more precise than the EDS readings, but many values are within 0.1 wt% of the corresponding EDS measurements. This includes most of the copper, silicon, chromium, sulphur, aluminium, phosphorus, and molybdenum measurements. Manganese readings are 0.1 wt% greater in most samples for the EDS technique than the results collected by *Celsa Steel UK* for the cast. This may have either been added in a process after casting or be due to a difference in the measurement techniques. Copper has the greatest variation of elements in the *Celsa Steel UK* composition as mass fraction varies by 0.132 wt%, between 0.365 wt% in sample six and 0.497 wt% in sample five.

4.2.2 Microscopy Results and Analysis

In the following figures, SE and BSD micrographs and EDS maps are shown for the four processing characteristics that have been sampled. Each processing characteristic is imaged in the cross sectional and longitudinal planes and both a site in the tempered core and the quenched edge regions are shown.

5C Core

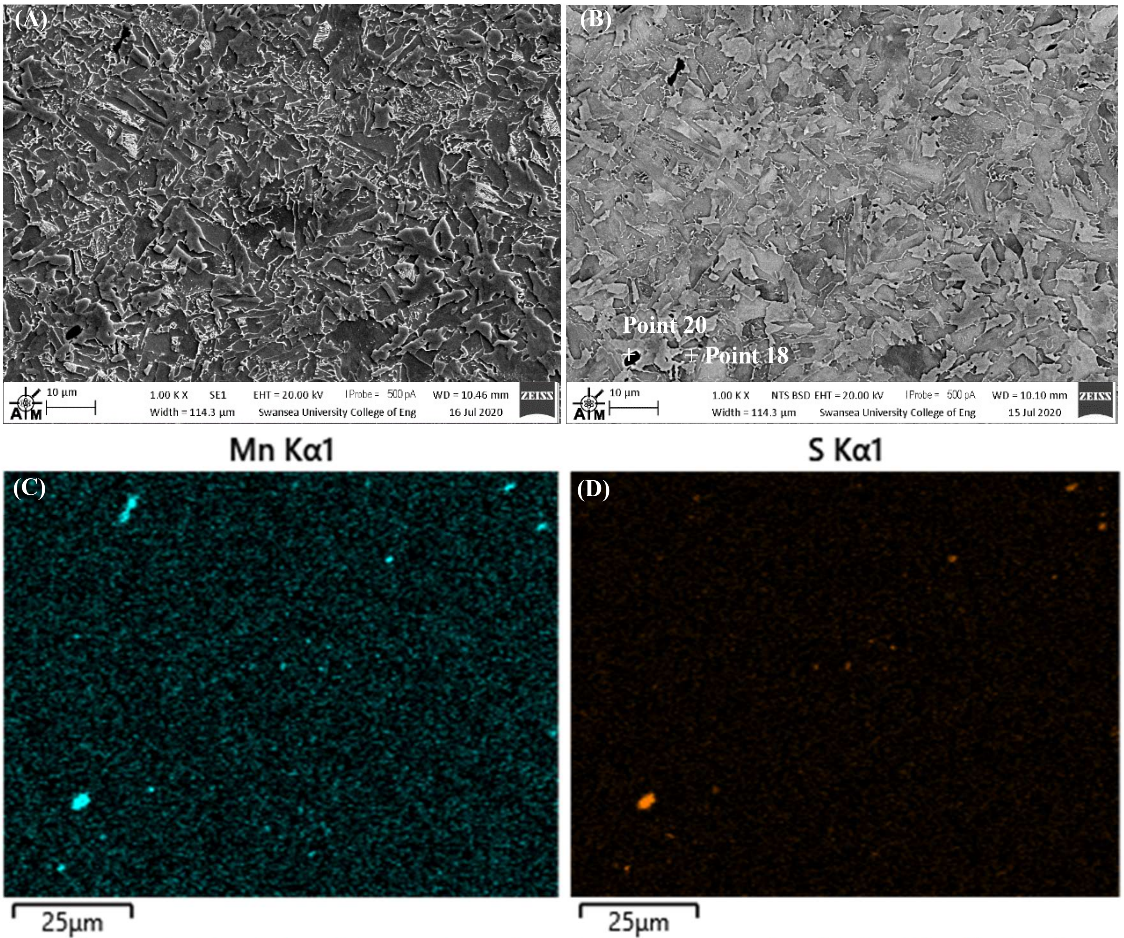

Figure 4.7 Micrographs taken in the self-tempered core of sample 5C using a secondary detector (A) and backscatter detector (B) and EDS images for Manganese (C) and Sulphur (D). Rolling direction is perpendicular to the page.

5C Core Composition	Wt%								
	Fe	Mn	Cu	Si	Cr	S	Al	P	Mo
Map Sum	97.9	1.0	0.5	0.2	0.2	0.1	0.0	0.0	0.0
Point 18	98.1	0.9	0.7	0.0	0.3	0.0	0.0	0.0	0.0
Point 20	10.9	58.2	0.0	0.0	0.0	30.9	0.0	0.0	0.0

Table 4.5 Composition results from EDS analysis of the mapped area, a point in a grain, and a point in an inclusion for the tempered core of sample 5C shown in Figure 4.7.

Micrographs in the core of sample 5C in figure 4.7 show ferrite grains with some lighter pearlite grains visible in image (A). Dark regions visible in (B) appear to be inclusions. The EDS maps (C) and (D) show that the inclusions in (B) contain manganese and sulphur. Table 4.5 shows the EDS composition analysis of the area in figure 4.7. Point 18 is a point within a grain and point 20 is in an inclusion. The ferrite grain composition is close to that of the map, with greater copper and chromium fractions. The inclusion contains 58.2 wt% manganese, 30.9 wt% sulphur and 10.9 wt% iron.

5C Edge

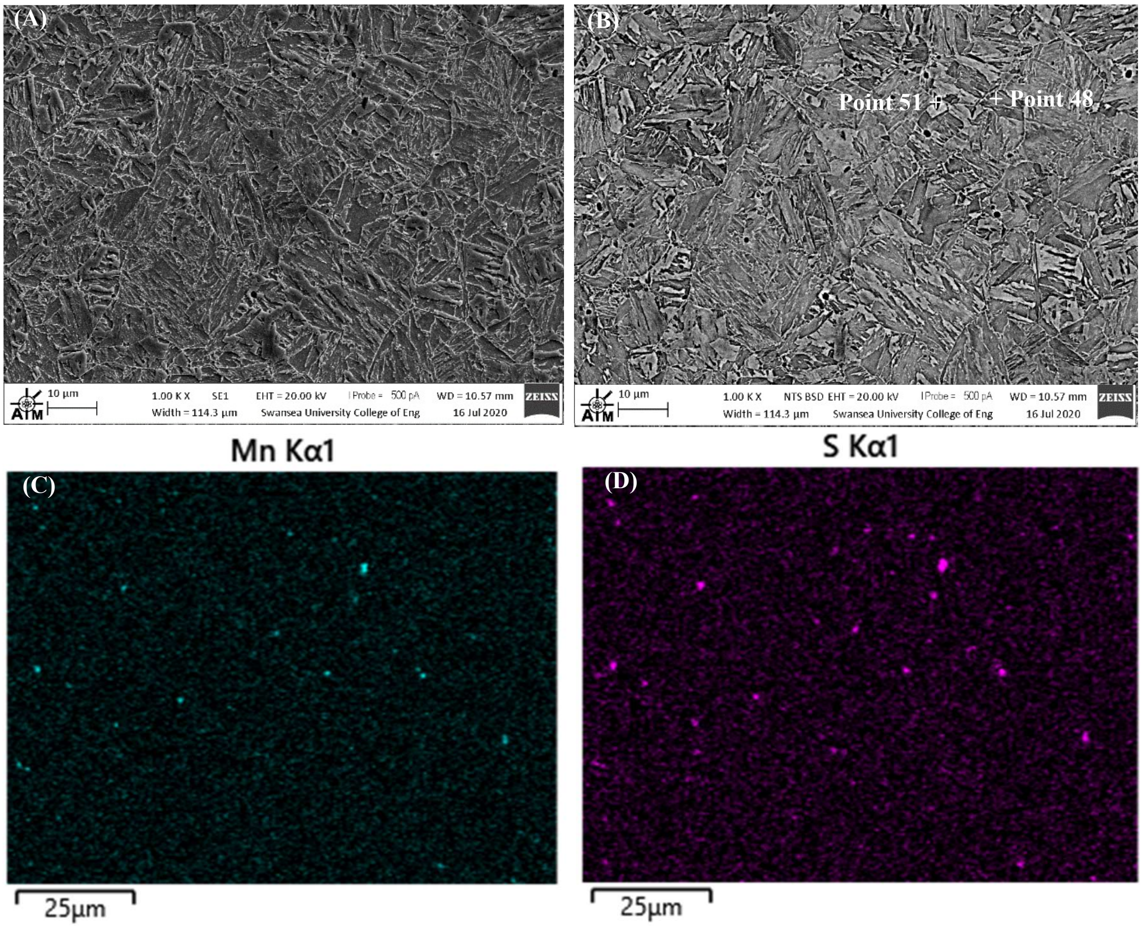

Figure 4.8 Micrographs taken in the quenched edge region of sample 5C using a secondary detector (A) and back scatter detector (B) and EDS images for manganese (C) and Sulphur (D). Rolling direction is perpendicular to the page.

5C Edge Composition	Wt%								
	Fe	Mn	Cu	Si	Cr	S	Al	P	Mo
Map Sum	97.9	1.0	0.6	0.2	0.2	0.1	0.0	0.0	0.0
Point 48	97.9	1.0	0.8	0.0	0.3	0.0	0.0	0.0	0.0
Point 51	43.7	35.0	0.5	0.0	0.3	18.5	0.0	0.0	0.0

Table 4.6 Composition results from EDS analysis of the mapped area, a point in a grain, and a point in an inclusion for the quenched edge region of sample 5C shown in Figure 4.8.

Micrographs and EDS results from the edge region of sample 5L are shown in figure 4.8 and table 4.6. The micrographs show martensite grains and round inclusions. EDS maps show these inclusions contain manganese and sulphur. Point 51 in table 4.6 is in an inclusion and contains more iron than the inclusion point shown in table 4.5. This may be because the point selected is close to the edge of the inclusion. Map sum composition is very similar to the 5C core, with 0.1 wt% more copper.

5L Core

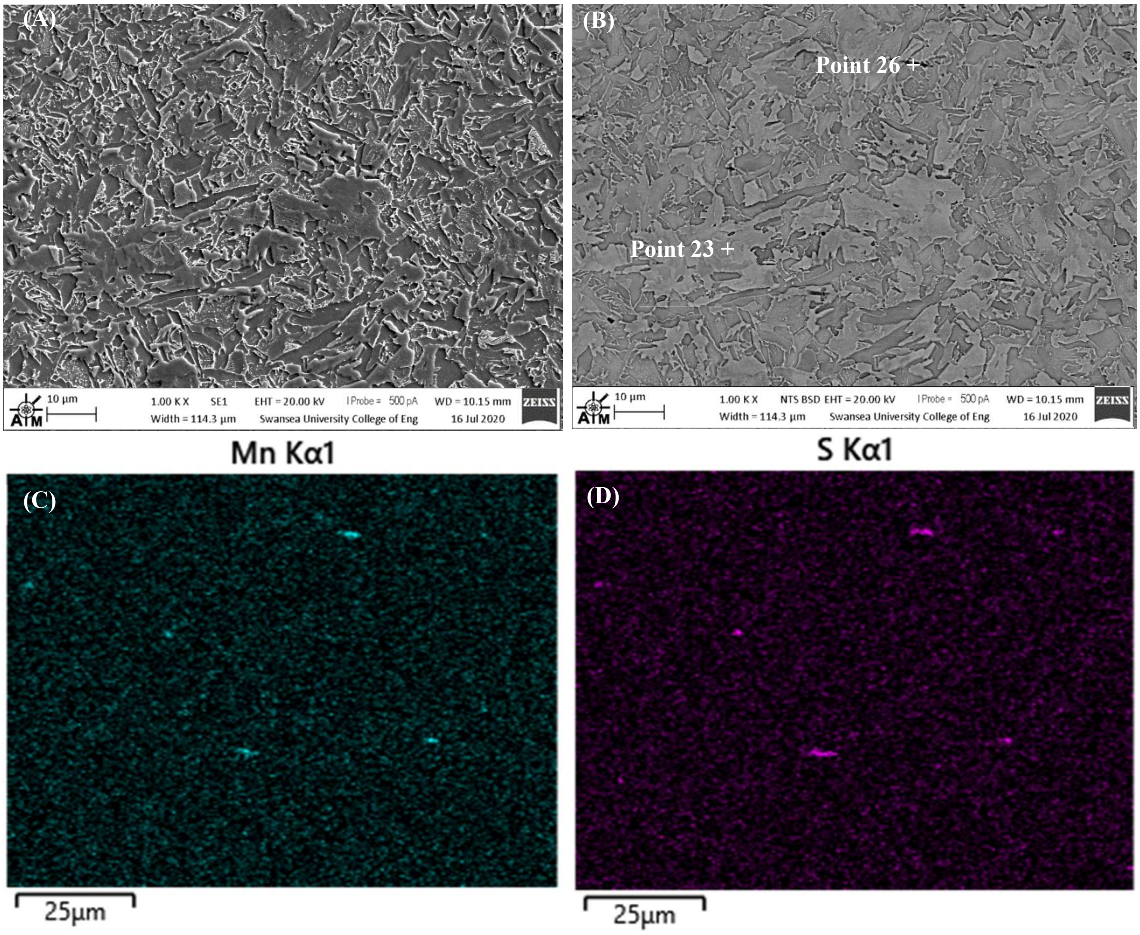

Figure 4.9 Micrographs taken in the self-tempered core of sample 5L using a secondary detector (A) and back scatter detector (B) and EDS images for manganese (C) and Sulphur (D). Rolling direction is left to right and manganese sulphide inclusions elongated in this direction are visible.

5L Core Composition	Wt%								
	Fe	Mn	Cu	Si	Cr	S	Al	P	Mo
Map Sum	98.1	1.0	0.6	0.2	0.2	0.0	0.0	0.0	0.0
Point 23	98.6	0.8	0.0	0.2	0.3	0.0	0.0	0.0	0.0
Point 26	64.0	22.7	0.5	0.0	0.0	12.8	0.0	0.0	0.0

Table 4.7 Composition results from EDS analysis of the mapped area, a point in a grain, and a point in an inclusion for the tempered core of sample 5L shown in Figure 4.9.

The core of the longitudinal plane of sample 5 is shown in figure 4.9 and table 4.7. This plane contains mostly ferrite, some lighter pearlite grains, and elongated inclusions in the rolling direction (left to right). These inclusions are composed of manganese and sulphur. The map sum EDS data is very similar to the 5C data. Unlike 5C, the point within a grain contains only 0.8% manganese and 0 wt% copper, however other points within grains did show copper content. The inclusion point is approximately two thirds iron, and the remaining composition is mostly manganese and sulphur in a 2:1 approximate ratio.

5L Edge

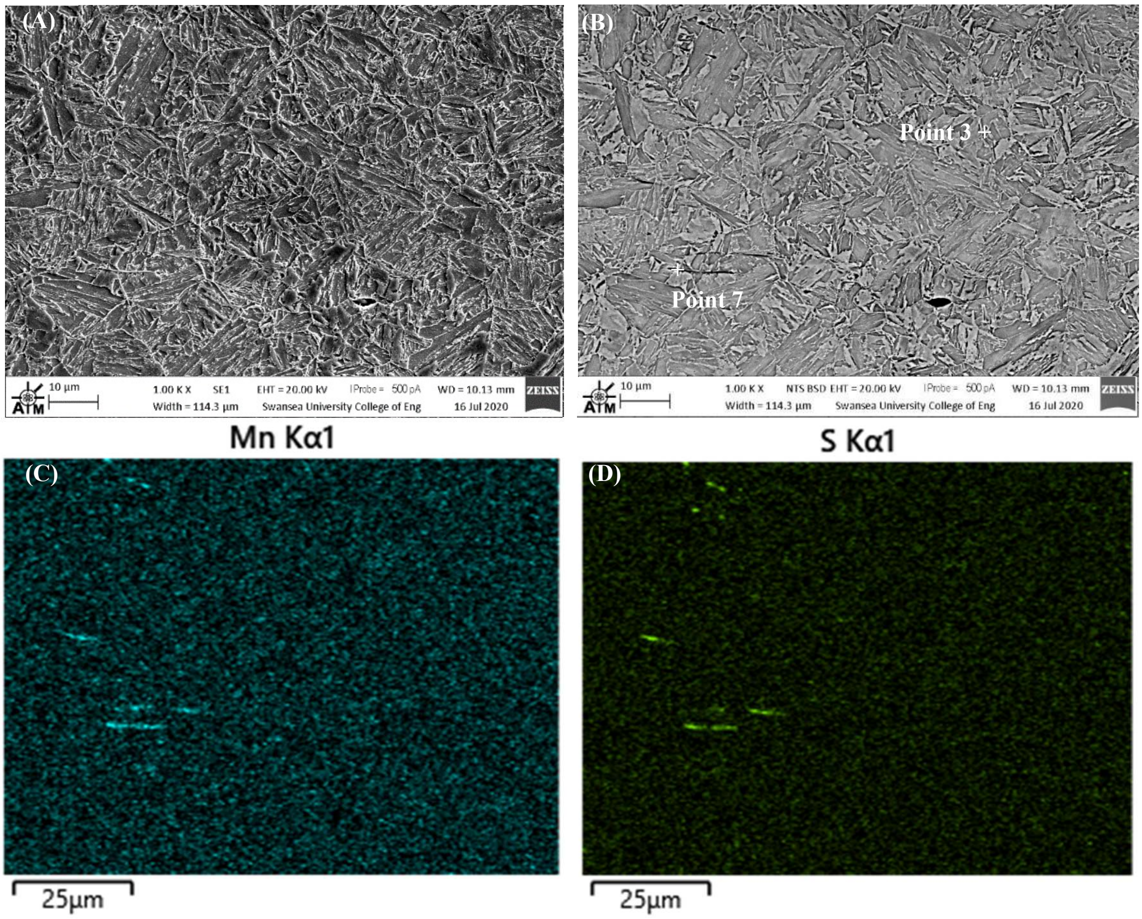

Figure 4.10 Micrographs taken in the quenched edge region of sample 5L using a secondary detector (A) and back scatter detector (B) and EDS images for manganese (C) and Sulphur (D). Rolling direction is from left to right.

5L Edge Composition	Wt%								
	Fe	Mn	Cu	Si	Cr	S	Al	P	Mo
Map Sum	98.0	0.9	0.6	0.2	0.2	0.0	0.0	0.0	0.0
Point 3	98.0	1.0	0.7	0.0	0.2	0.0	0.0	0.0	0.0
Point 7	62.7	23.2	0.4	0.0	0.0	13.7	0.0	0.0	0.0

Table 4.8 Composition results from EDS analysis of the mapped area, a point in a grain, and a point in an inclusion for the quenched edge region of sample 5L shown in Figure 4.10.

Figure 4.10 shows that manganese sulphide inclusions are also elongated in the rolling direction in the edge of sample 5L. Table 4.8 shows similar composition for the map sum, a point within a grain and a point in an inclusion as seen in the other samples. Inclusions that appear in line with each other may be connected as the inclusion may not be a straight line and could move above or below the sample surface so that sections of the inclusion are not visible in this image.

6C Core

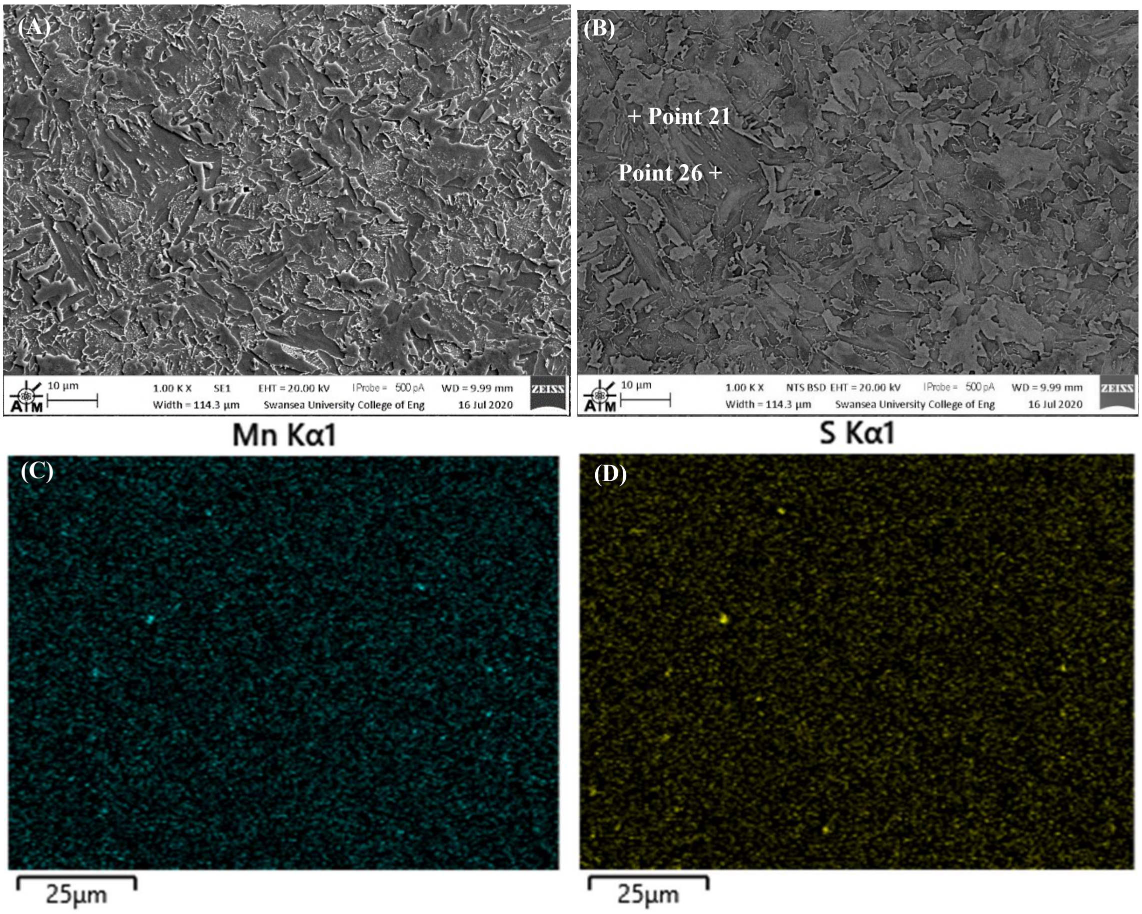

Figure 4.11 Micrographs taken in the self-tempered core of sample 6C using a secondary detector (A) and backscatter detector (B) and EDS images for manganese (C) and Sulphur (D). Rolling direction is perpendicular to the page.

6C Core Composition	Wt%								
	Fe	Mn	Cu	Si	Cr	S	Al	P	Mo
Map Sum	98.7	1.0	0.0	0.2	0.1	0.0	0.0	0.0	0.0
Point 21	99.0	0.7	0.0	0.0	0.2	0.0	0.0	0.0	0.0
Point 26	49.5	32.2	0.7	0.0	0.0	17.7	0.0	0.0	0.0

Table 4.9 Composition results from EDS analysis of the mapped area, a point in a grain, and a point in an inclusion for the tempered core of sample 6C shown in Figure 4.11.

Like the micrographs for sample 5, figure 4.11 shows that the core cross section of sample 6 contains mostly ferrite and some lighter pearlite grains (A) with a small number of circular inclusions (B) which contain manganese and sulphur (C) and (D). Table 4.9 shows that EDS compositions of the map sum and point within a grain (point 21) are very similar to the core of sample 5C. The point in an inclusion for this figure contains lower fractions of manganese and sulphur and more ferrite, this may be because the point selected was not in the centre of the inclusion.

6C Edge

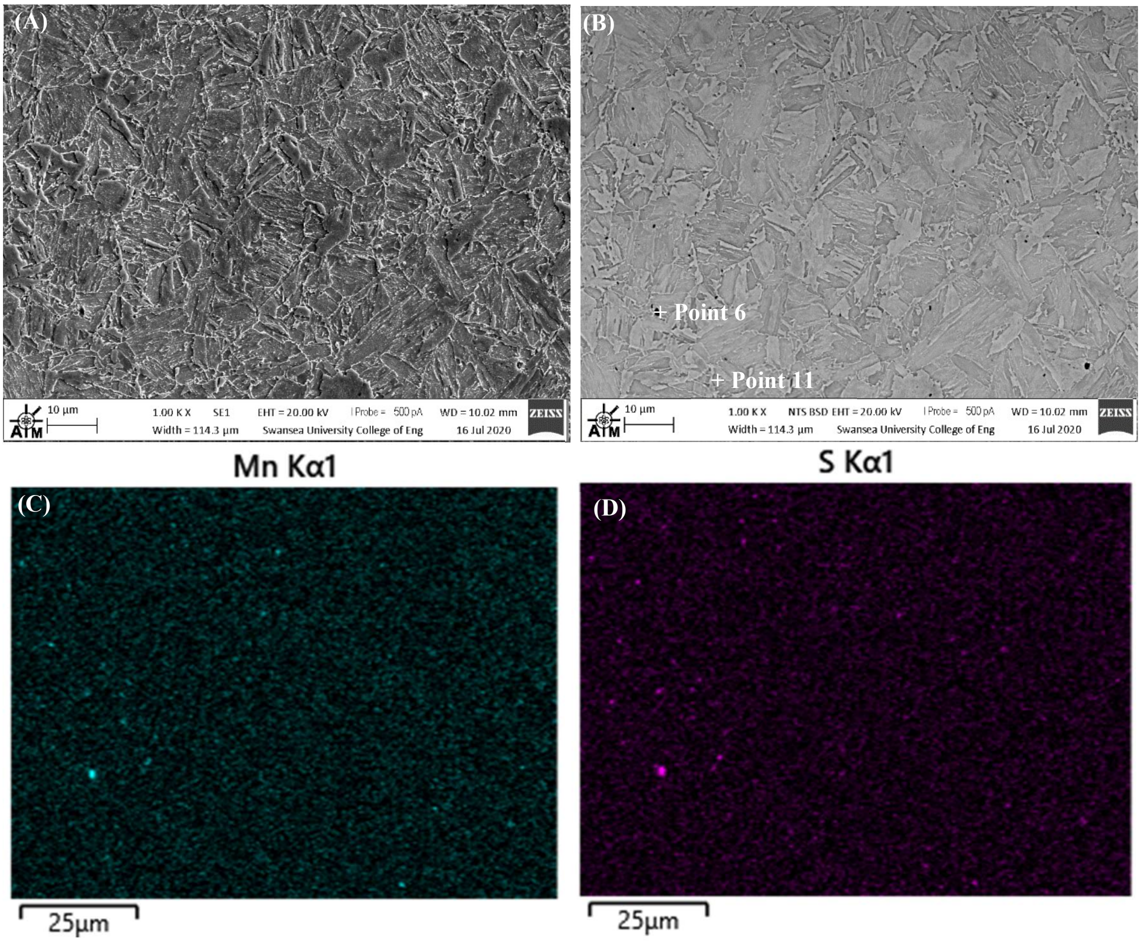

Figure 4.12 Micrographs taken in the quenched edge region of sample 6C using a secondary detector (A) and back scatter detector (B) and EDS images for manganese (C) and Sulphur (D). Rolling direction is perpendicular to the page.

6C Edge Composition	Wt%									
	Fe	Mn	Cu	Si	Cr	S	Al	P	Mo	O
Map Sum	98.2	0.9	0.4	0.2	0.1	0.0	0.0	0.0	0.1	0.0
Point 11	96.1	2.5	0.9	0.0	0.0	0.5	0.0	0.0	0.0	0
Point 6	36.2	39.5	0.4	1.6	0.0	20.4	0.0	0.0	0.0	1.6

Table 4.10 Composition results from EDS analysis of the mapped area, a point in a grain (point 11), and a point in an inclusion (point 6) for the quenched edge region of sample 6C shown in Figure 4.12.

The cross section of the edge, shown in figure 4.12 and table 4.10, contains lath martensite grains since a high density of dislocations are visible within prior austenite grains. Circular inclusions containing manganese and sulphur are also present. The map sum contains a composition closer to the target composition. The point within a grain, point 11 contains greater fractions of additional elements than expected, 2.5 wt% manganese, 0.9 wt% copper, and 0.5 wt% sulphur. This may be due to the point being close to a grain boundary. Point 6 shows that the inclusion contains large proportions of manganese and sulphur. The silicon seen may have been deposited during polishing.

6L Core

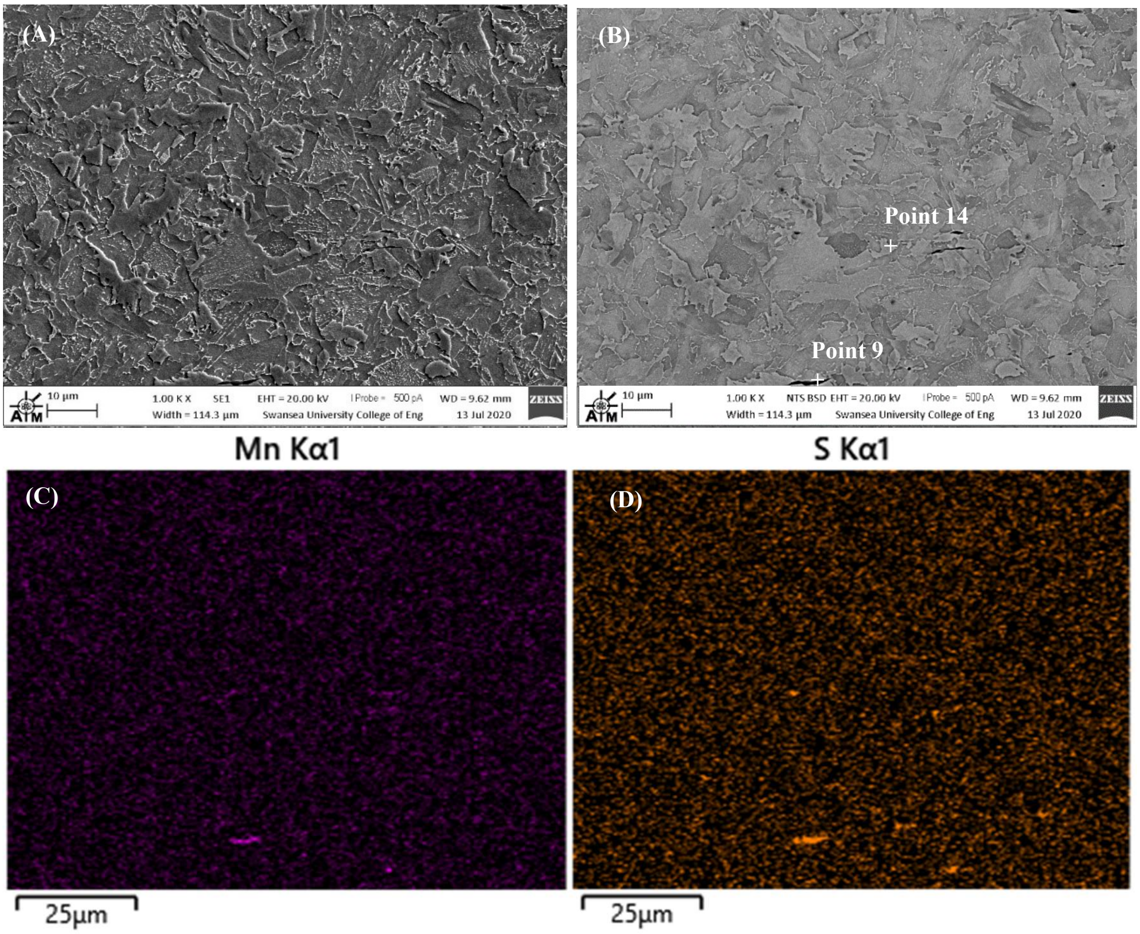

Figure 4.13 Micrographs taken in the self-tempered tempered core of sample 6L using a secondary detector (A) and back scatter detector (B) and EDS images for manganese (C) and Sulphur (D). Rolling direction is left to right.

6L Core Composition	Wt%								
	Fe	Mn	Cu	Si	Cr	S	Al	P	Mo
Map Sum	98.3	0.9	0.4	0.1	0.1	0.0	0.0	0.0	0.1
point 14	98.5	1.0	0.6	0.0	0.0	0.0	0.0	0.0	0.0
Point 9	62.6	23.3	0.4	0.0	0.0	13.6	0.0	0.0	0.0

Table 4.11 Composition results from EDS analysis of the mapped area, a point in a grain, and a point in an inclusion for the tempered core of sample 6L shown in Figure 4.13.

The microstructure and composition in the core of the longitudinal section of sample six are shown in figure 4.13 and 4.11. The micrographs show equiaxed grains and inclusions which are elongated in the rolling direction. EDS analysis shows that the grains contain 98.5 wt% Fe, as well as Mn and Cu in similar levels to the sum composition, whereas the inclusion contains a larger proportion of Mn and S.

6L Edge

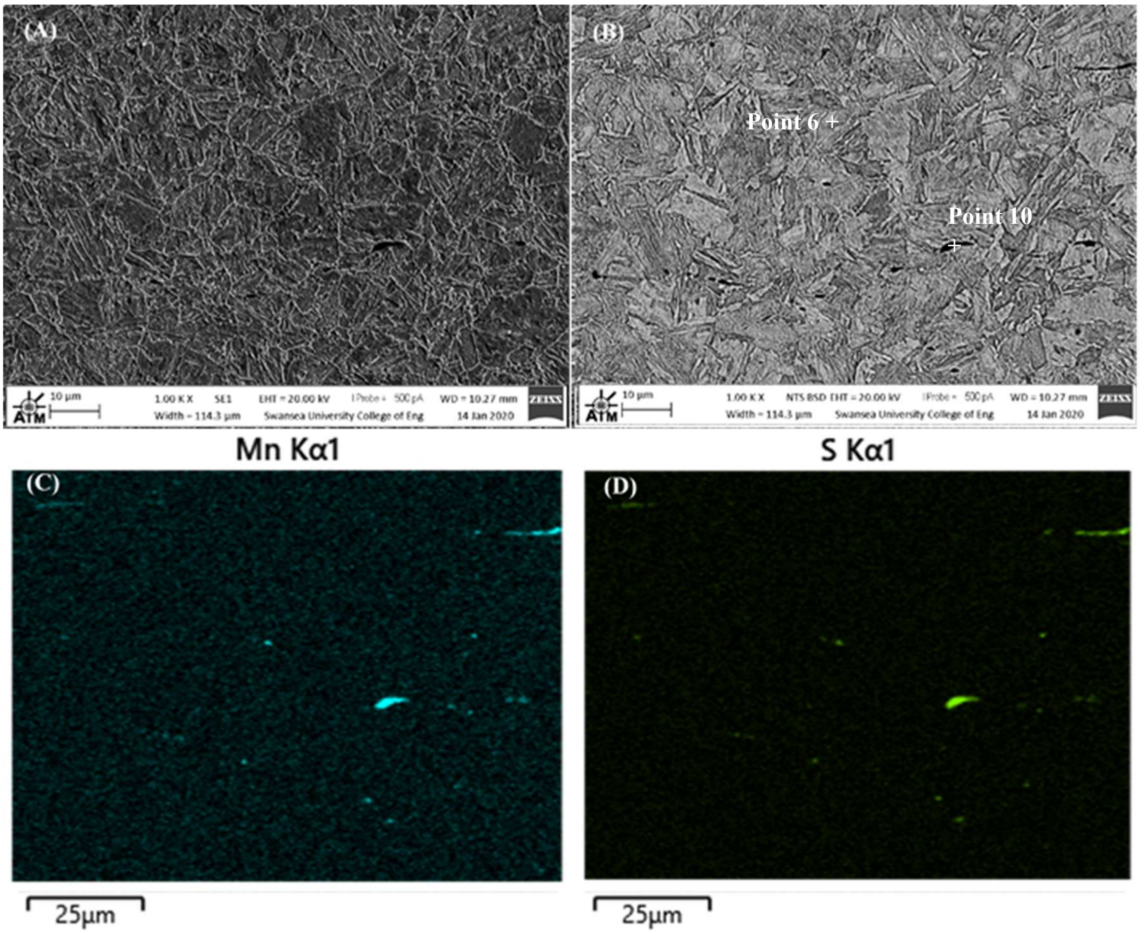

Figure 4.14 Micrographs taken in the quenched edge region of sample 6L using a secondary detector (A) and back scatter detector (B) and EDS images for manganese (C) and Sulphur (D). Rolling direction is left to right.

6L Edge	Wt%								
Composition	Fe	Mn	Cu	Si	Cr	S	Al	P	Mo
Map Sum	97.9	1.0	0.5	0.2	0.2	0.1	0.0	0.0	0.0
point 6	99.0	0.8	0.0	0.2	0.0	0.0	0.0	0.0	0.0
Point 10	62.7	23.3	0.4	0.0	0.0	13.6	0.0	0.0	0.0

Table 4.12 Composition results from EDS analysis of the mapped area, a point in a grain, and a point in an inclusion for the quenched edge region of sample 6L shown in Figure 4.14.

Figure 4.14 shows micrographs of a region near the edge of the sample six longitudinal section and the location of two points for which the composition, and the sum composition of the area, is shown in table 4.12. Lathes visible within grains in (B) give the appearance of martensite. Inclusions containing manganese and sulphur are visible from the EDS maps (C) and (D) and show elongation in the rolling direction. The table shows a standard composition for the map sum, however, point 6, within a grain, does not show any copper.

7C Core

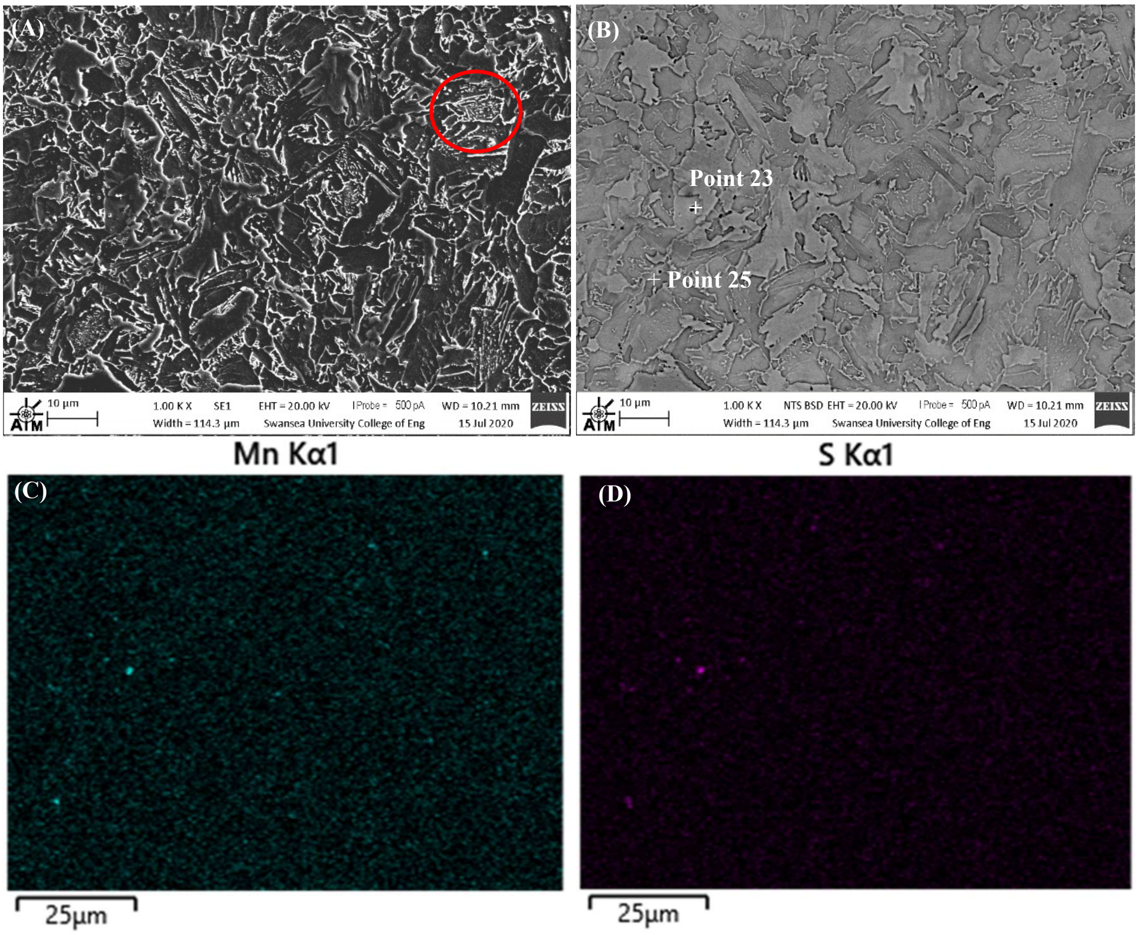

Figure 4.15 Micrographs taken in the self-tempered core of sample 7C using a secondary detector (left) and backscatter detector (right) and EDS images for manganese (C) and Sulphur (D). Rolling direction is perpendicular to the page.

7C Core Composition	Wt%								
	Fe	Mn	Cu	Si	Cr	S	Al	P	Mo
Map Sum	98.3	1.0	0.3	0.2	0.1	0.0	0.0	0.1	0.0
Point 25	98.6	0.8	0.5	0.2	0.0	0.0	0.0	0.0	0.0
Point 23	46.9	32.9	1.1	0.0	0.6	18.5	0.0	0.0	0.0

Table 4.13 Composition results from EDS analysis of the mapped area, a point in a grain, and a point in an inclusion for the tempered core of sample 7C shown in Figure 4.15.

The 7C core contains ferrite and pearlite grains with visible alternating layers of ferrite and cementite, as circled in figure 4.15 (A). Circular inclusions visible in the backscattered image (figure 4.15 (B)) are composed of manganese and sulphur (figure 4.15 (C) and (D). In addition to high fractions of ferrite, manganese and sulphur, the point in an inclusion, point 23, contains 1.1 wt% copper and 0.6 wt% chromium.

7C Edge

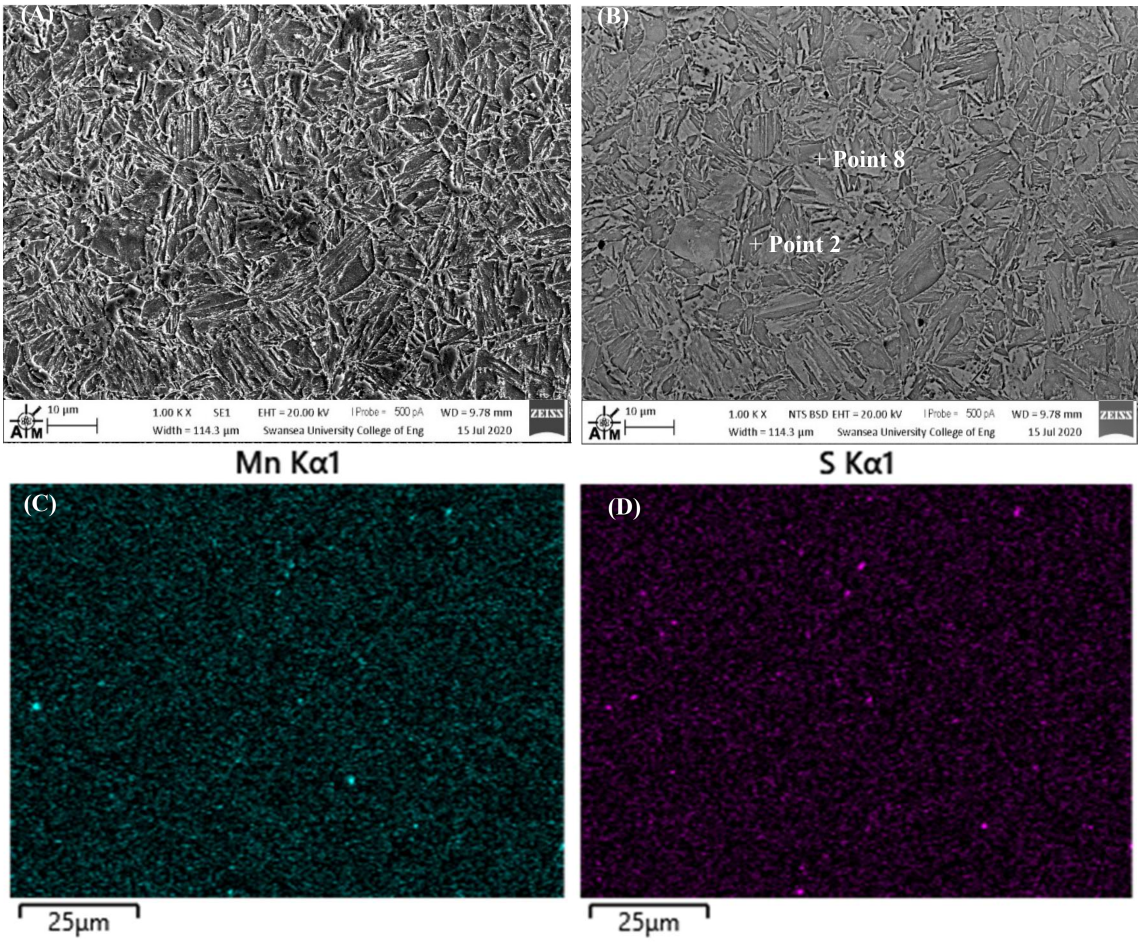

Figure 4.16 Micrographs taken in the quenched edge region of sample 7C using a secondary detector (A) and back scatter detector (B) and EDS images for manganese (C) and Sulphur (D). Rolling direction is perpendicular to the page.

7C Edge Composition	Wt%									
	Fe	Mn	Cu	Si	Cr	S	Al	P	Mo	O
Map Sum	98.3	1.0	0.4	0.2	0.2	0.0	0.0	0.0	0.0	0.0
Point 2	98.4	0.9	0.5	0.2	0.0	0.0	0.0	0.0	0.0	0.0
Point 8	74.9	14.7	0.8	0.0	0.0	7.7	0.0	0.0	0.0	1.9

Table 4.14 Composition results from EDS analysis of the mapped area, a point in a grain, and a point in an inclusion for the quenched edge region of sample 7C shown in Figure 4.16.

The quenched edge region of sample 7C contains lath martensite grains and circular inclusions, as shown in figure 4.16. As with the other samples, EDS analysis shows these inclusions contain manganese and sulphur and thus are manganese sulphide inclusions. Point 2 is a point placed within a grain and point 8 is within an inclusion, the positions of these are shown in figure 4.16. EDS point analysis at these points shows the composition within a grain is close to the map sum composition and the inclusion contains large fractions of manganese and sulphur.

7L Core

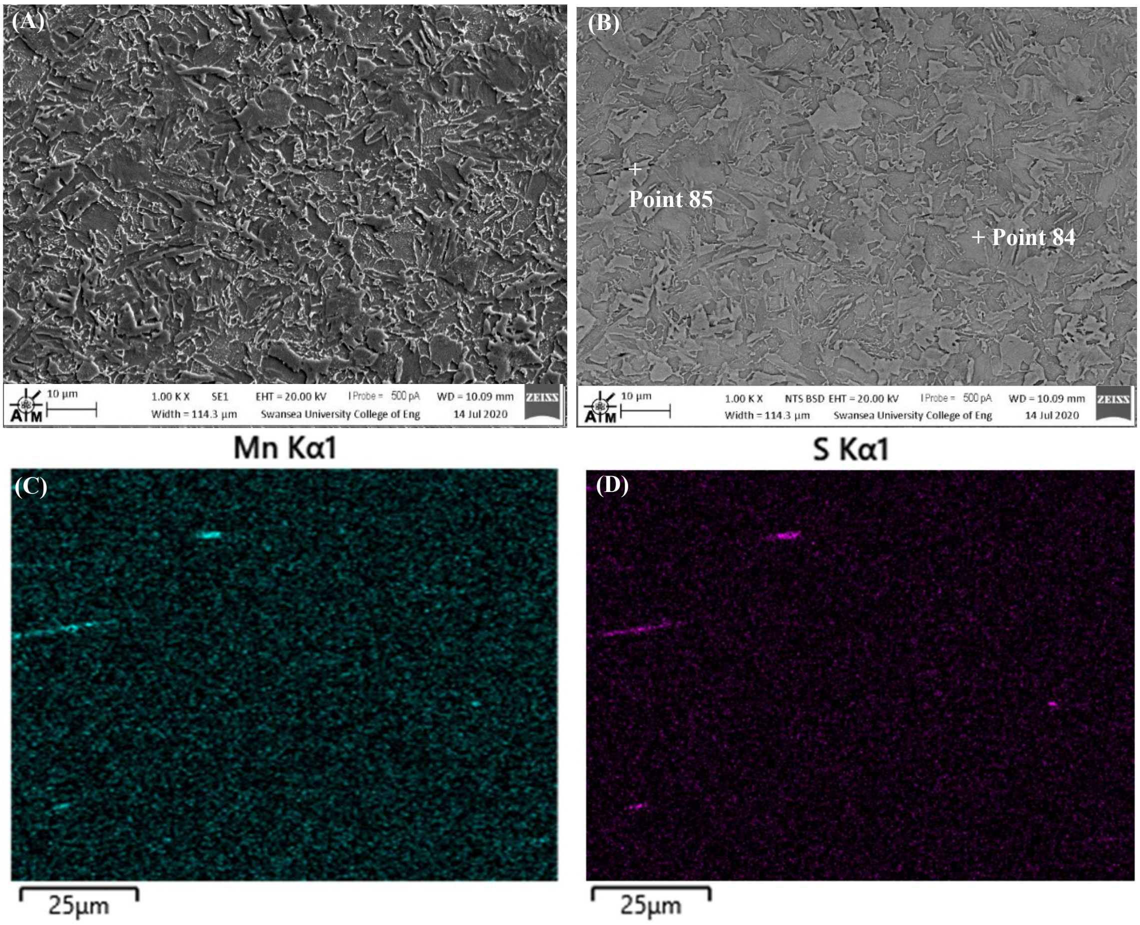

Figure 4.17 Micrographs taken in the self-tempered tempered core of sample 7L using a secondary detector (A) and back scatter detector (B) and EDS images for manganese (C) and Sulphur (D). Rolling direction is left to right.

7L Core	Wt%								
Composition	Fe	Mn	Cu	Si	Cr	S	Al	P	Mo
Map Sum	98.3	1.0	0.4	0.1	0.2	0.0	0.0	0.0	0.0
Point 84	98.5	0.8	0.5	0.0	0.2	0.0	0.0	0.0	0.0
Point 85	89.0	6.3	0.5	0.2	0.2	3.7	0.0	0.0	0.0

Table 4.15 Composition results from EDS analysis of the mapped area, a point in a grain, and a point in an inclusion for the tempered core of sample 7L shown in Figure 4.17.

The manganese sulphide inclusions visible in the core of sample 7L, shown in figure 4.17, are elongated in the rolling direction (left to right). However, grains are not elongated, instead they are mostly equiaxed which shows they recrystallize after hot rolling. These grains are mostly ferrite, and some are pearlite. The EDS for a point in an inclusion in table 4.15, point 85, shows a much smaller amount of sulphur and manganese than the other samples. This may be because it is in the edge of the inclusion or in a small region of ferrite within the inclusion.

7L Edge

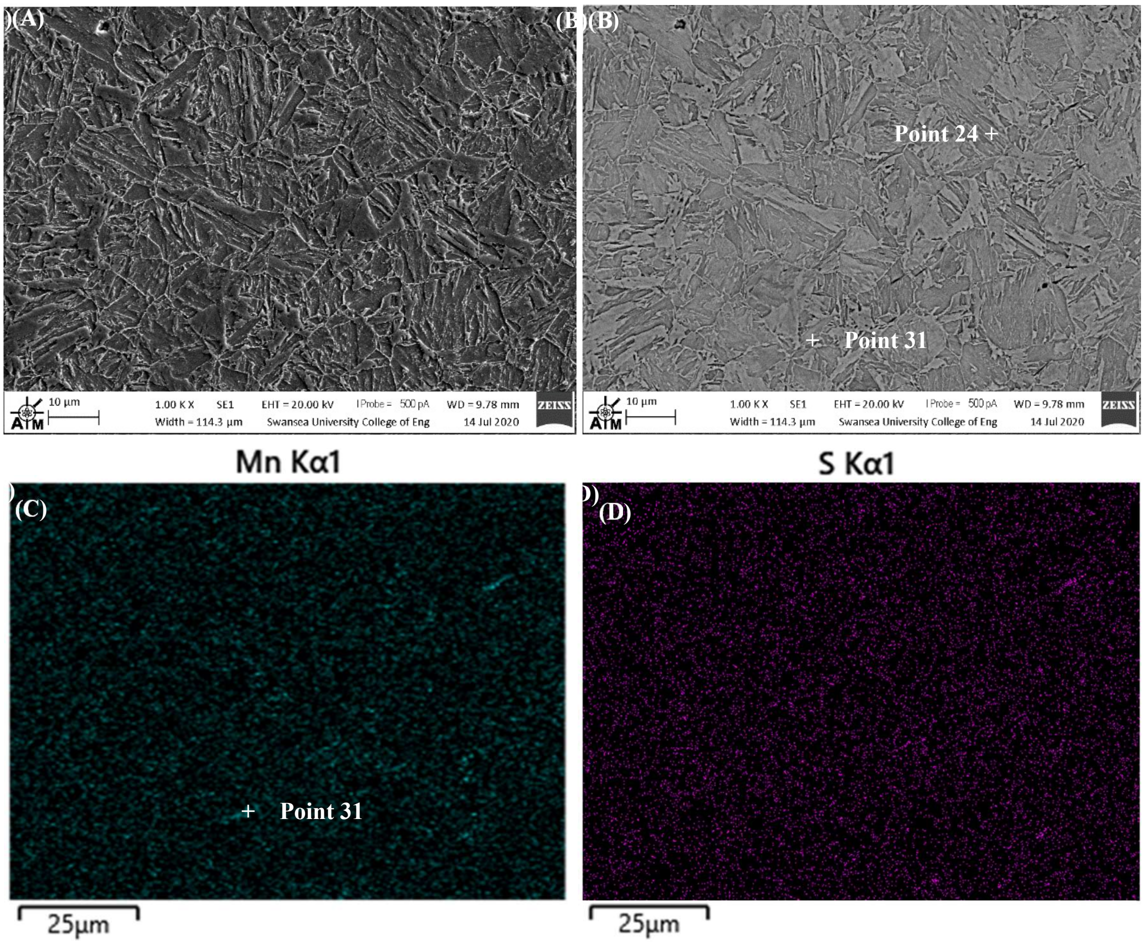

Figure 4.18 Micrographs taken in the quenched edge region of sample 7L using a secondary detector (A) and back scatter detector (B) and EDS images for manganese (C) and Sulphur (D). Rolling direction is left to right.

7L Edge Composition	Wt%								
	Fe	Mn	Cu	Si	Cr	S	Al	P	Mo
Map Sum	98.3	0.9	0.4	0.1	0.2	0.0	0.0	0.0	0.0
Point 24	98.9	0.9	0.0	0.0	0.2	0.0	0.0	0.0	0.0
Point 31	97.7	1.3	0.5	0.2	0.0	0.3	0.0	0.0	0.0

Table 4.16 Composition results from EDS analysis of the mapped area, a point in a grain, and a point in an inclusion for the quenched edge region of sample 7L shown in Figure 4.18.

Figure 4.18 shows the edge region of sample 7L is made up of martensite laths within prior austenite grains that have an equiaxed structure. Manganese sulphide inclusions are elongated approximately in the rolling direction. Results of EDS analysis in table 4.16 shows the sum composition of the map is similar to the composition of a point within a grain, point 24. This is expected since the steel is primarily made up of grains. A point within an inclusion, point 31, contains 1.3 wt% manganese and 0.3 wt% sulphur. Both mapped areas shown from sample 7L show less manganese and sulphur mass fractions in inclusion points than the other samples.

8C Core

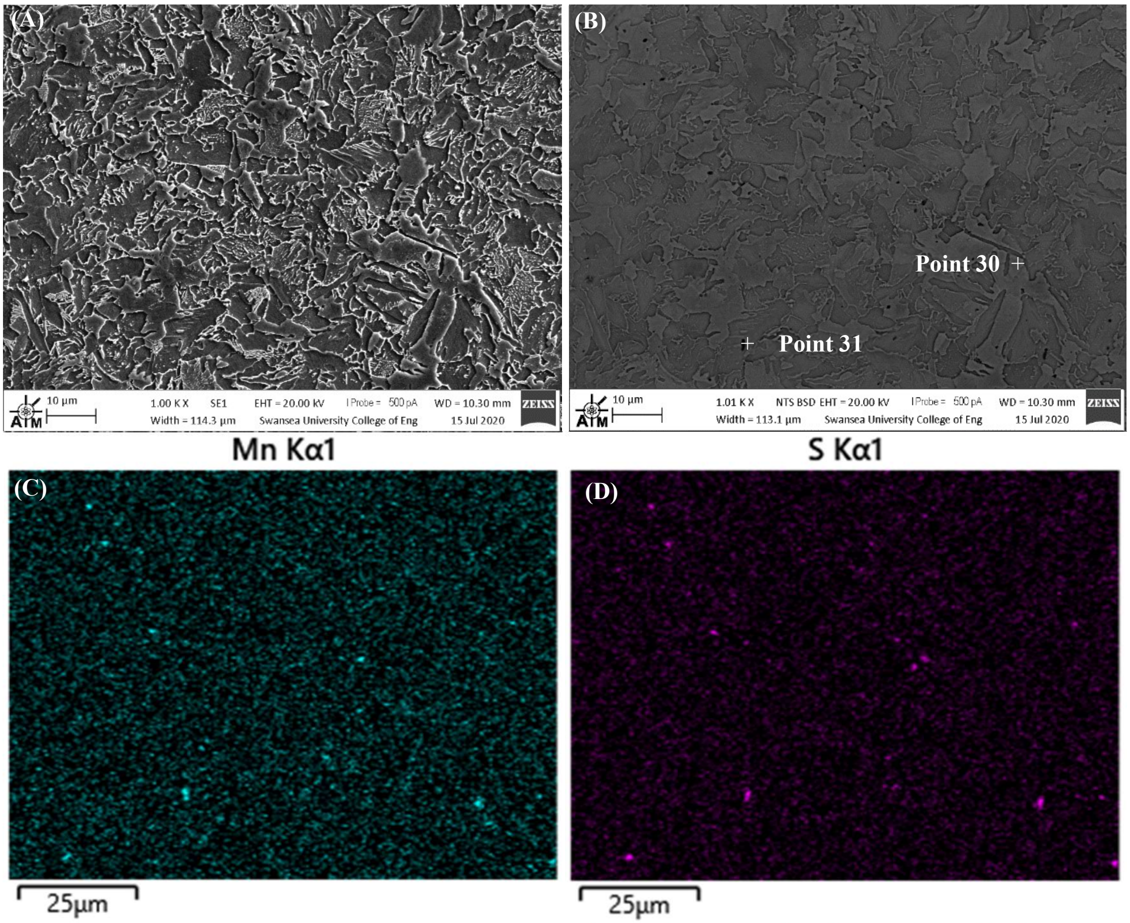

Figure 4.19 Micrographs taken in the self-tempered core of sample 8C using a secondary detector (A) and backscatter detector (B) and EDS images for manganese (C) and Sulphur (D). Rolling direction is perpendicular to the page.

8C Core Composition	Wt%								
	Fe	Mn	Cu	Si	Cr	S	Al	P	Mo
Map Sum	98.1	1.0	0.5	0.2	0.2	0.1	0.0	0.0	0.0
Point 30	98.2	1.0	0.6	0.0	0.2	0.0	0.0	0.0	0.0
Point 31	38.2	40.0	0.6	0.0	0.0	21.2	0.0	0.0	0.0

Table 4.17 Composition results from EDS analysis of the mapped area, a point in a grain, and a point in an inclusion for the self-tempered core of sample 8C shown in Figure 4.19.

Sample 8 displayed twisting when the coil was processed with an automatic link bender and the microstructure in the core region of sample 8 is shown in figure 4.19. Like other samples, grains are primarily ferrite with some pearlite grains that have visible layers of ferrite and cementite. Some small, approximately circular manganese sulphide inclusions are also visible in figure 4.19 and a point within one of the inclusions, point 31 in table 4.17, contains 40 wt% manganese and 21.2 wt% sulphur. The map sum composition from EDS analysis shows the composition is approximately equal to other samples and the target composition.

8C Edge

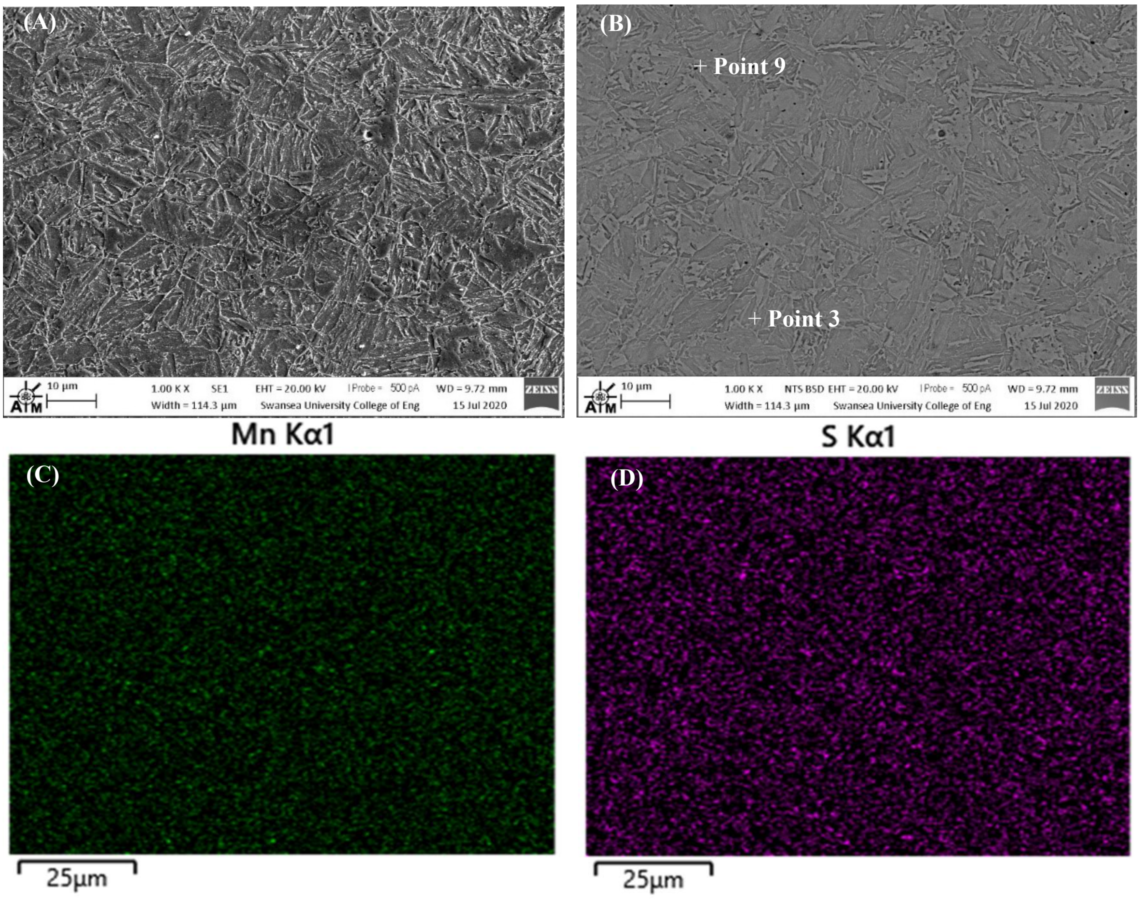

Figure 4.20 Micrographs taken in the quenched edge region of sample 7C using a secondary detector (A) and back scatter detector (B) and EDS images for manganese (C) and Sulphur (D). Rolling direction is perpendicular to the page.

8C Edge Composition	Wt%								
	Fe	Mn	Cu	Si	Cr	S	Al	P	Mo
Map Sum	98.1	1.0	0.5	0.2	0.2	0.0	0.0	0.0	0.0
Point 3	97.8	1.0	0.6	0.3	0.2	0.0	0.0	0.0	0.0
Point 9	68.1	20.4	0.7	0.2	0.3	10.5	0.0	0.0	0.0

Table 4.18 Composition results from EDS analysis of the mapped area, a point in a grain, and a point in an inclusion for the quenched edge region of sample 8C shown in Figure 4.20.

The quenched edge region of sample 8C contains lath pearlite within prior austenite grains with small, circular inclusions containing Mn and S, as shown by figure 4.20. Point 3 is in a martensite lathe and point 9 is in an inclusion. Table 4.18 shows that the lathe composition is similar to the sum composition of the map whereas point 9 contains 20.4 wt% Mn and 10.5 wt% S.

<u>8L Core</u>

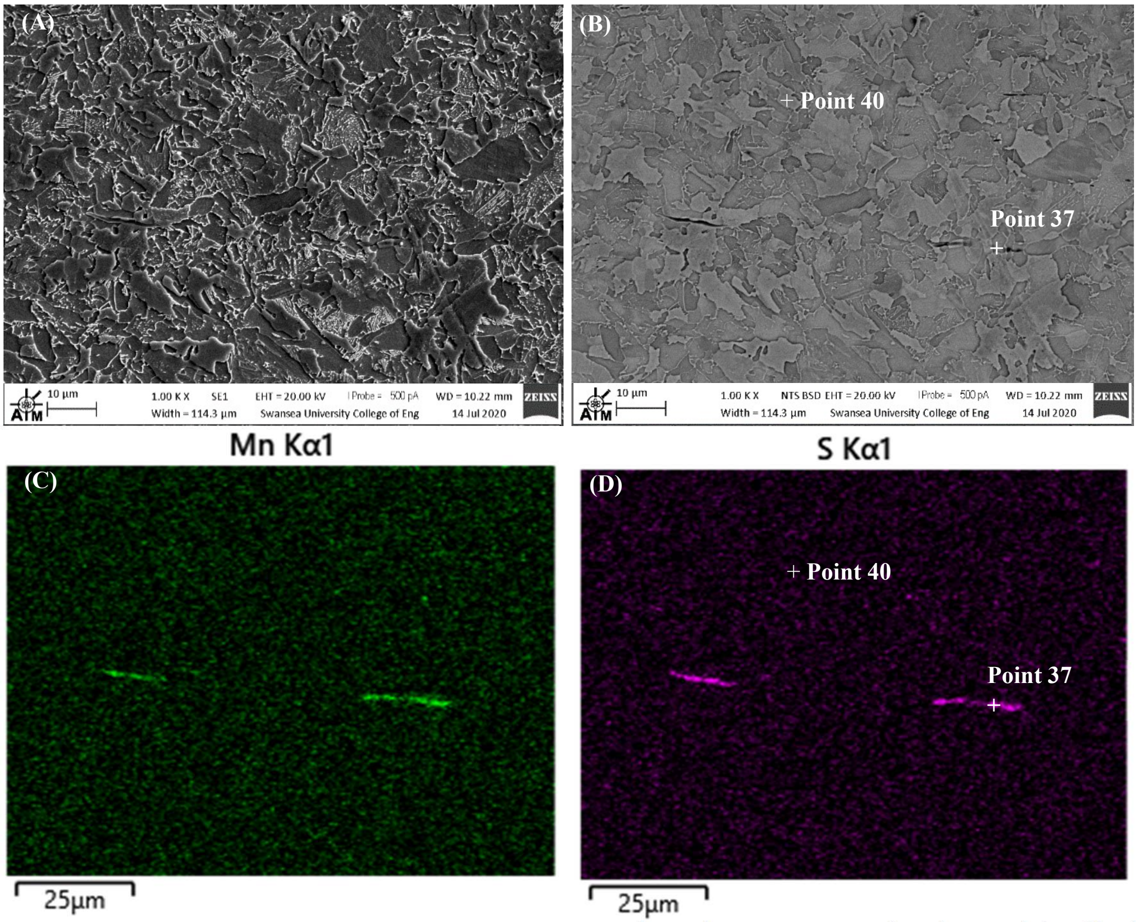

Figure 4.21 Micrographs taken in the self-tempered tempered core of sample 8L using a secondary detector (A) and back scatter detector (B) and EDS images for manganese (C) and Sulphur (D). Rolling direction is left to right.

8L Core Composition	Wt%								
	Fe	Mn	Cu	Si	Cr	S	Al	P	Mo
Map Sum	98.2	1.0	0.5	0.2	0.2	0.0	0.0	0.0	0.0
Point 40	98.4	1.2	0.4	0.0	0.0	0.0	0.0	0.0	0.0
Point 37	57.6	28.8	0	1.7	0.0	11.8	0.0	0.0	0.0

Table 4.19 Composition results from EDS analysis of the mapped area, a point in a grain, and a point in an inclusion for the self-tempered core of sample 8L shown in Figure 4.21.

The core of sample 8L in figure 4.21 has a similar microstructure to the core of sample 8C, in figure 4.19, except the inclusions are elongated in the rolling direction, left to right. For cross section samples, the rolling direction is perpendicular to the image, so these inclusions appear circular. There is a mixture of ferrite and pearlite grains in sample 8L. Two large inclusions are visible in figure 4.21 and point 37 is placed in one of these. EDS analysis of point 37 shows the inclusion point contains 28.8 wt% manganese and 11.8 wt% sulphur.

8L Edge

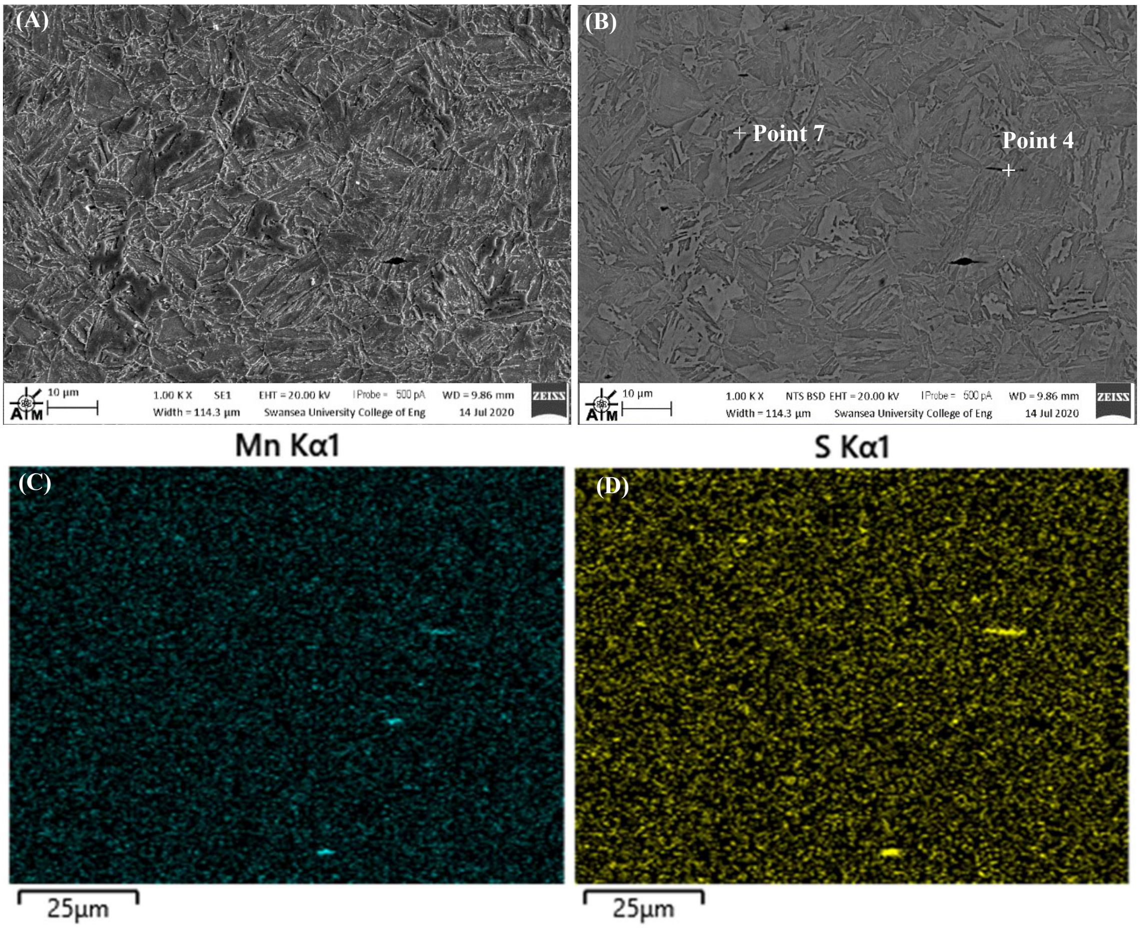

Figure 4.22 Micrographs taken in the quenched edge region of sample 8L using a secondary detector (A) and back scatter detector (B) and EDS images for manganese (C) and Sulphur (D). Rolling direction is left to right.

8L Edge Composition	Wt%								
	Fe	Mn	Cu	Si	Cr	S	Al	P	Mo
Map Sum	98.1	1.0	0.5	0.2	0.2	0.0	0.0	0.0	0.0
Point 7	98.5	1.0	0.3	0.2	0.0	0.0	0.0	0.0	0.0
Point 4	93.5	4.1	0.7	0.0	0.0	1.7	0.0	0.0	0.0

Table 4.20 Composition results from EDS analysis of the mapped area, a point in a grain, and a point in an inclusion for the quenched edge region of sample 8L shown in Figure 4.22.

Figure 4.22 shows the microstructure of sample 8L in the edge region contains lath martensite with some elongated inclusions in the rolling direction. EDS analysis shows low fractions of alloying elements in a martensite lath but high amounts of manganese and sulphur in the inclusions. However, the point in an inclusion, point four, has much lower proportions of manganese and sulphur than most other samples as 93.5 wt% of point four is ferrite.

SEM Summary

The SEM results in figures 4.15 to 4.22 show that all the samples contain ferrite and pearlite grains and manganese sulphide inclusions in the core region, and martensite grains with manganese sulphide inclusions in the quenched edge region. In each sample, the grains are approximately equiaxed while inclusions are thin and elongated in the rolling direction. EDS analysis shows compositions in each sample which are close to the expected composition, with low amounts of alloying elements.

Three SEM maps were created in the core region of each sample, one of these for each sample is shown in figures 4.15, 4.17, 4.19, 4.21. The average MLI and inclusion percentage for each sample was found using MLI and inclusion area measurements from the three micrographs. Table 4.19 shows that the samples measured from SEM micrographs have similar grain sizes. The average grain diameter of the samples varies by 0.86 µm, between 3.61 and 4.47 µm, as measured using the MLI technique. There is no clear difference in the grain size, between samples or between longitudinal and cross-sectional planes. Standard deviation was larger in longitudinal samples than cross sections.

There are small differences in the area proportion covered by inclusions seen between samples and planes in table 4.21. Samples 7 and 8 have approximately 0.23% inclusion area whereas samples 5 and 6 have inclusion area greater than 0.30%. Also, longitudinal samples generally have greater inclusion percentage area which is likely to be because inclusions are elongated in the rolling direction so are more visible in this plane.

Description	Sample	Average MLI (µm)	MLI Standard Deviation	Inclusion % Area	Inclusion Standard Deviation
Control	5C Core	3.78	0.03	0.30	0.04
	5L Core	3.61	0.32	0.34	0.05
Twin Strand, Shorter	6C Core	4.17	0.16	0.29	0.07
	6L Core	3.67	0.23	0.37	0.03
Twin Strand, Longer	7C Core	3.91	0.08	0.24	0.08
	7L Core	4.47	0.44	0.23	0.11
Twisting	8C Core	3.68	0.15	0.22	0.03
	8L Core	3.81	0.27	0.24	0.14
average		3.89	0.21	0.28	0.07

Table 4.21 Average MLI and percentage area of inclusions measured from three BSD detector images in the core of samples with different processing characteristics. Each sample is imaged in cross sectional and longitudinal planes.

4.3 EBSD Results and Analysis

5C

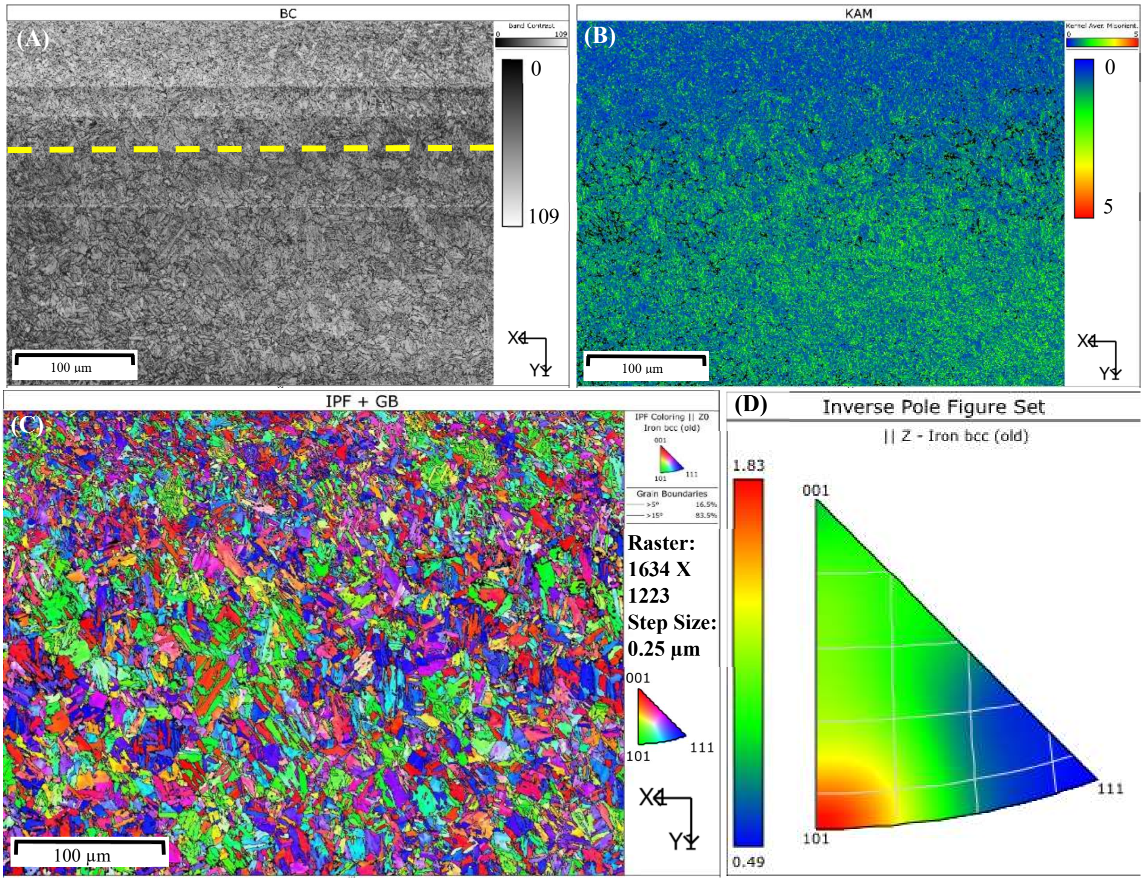

Figure 4.23 EBSD figures for 5C, the consistently processed sample cross section at a site in the interface region with ferrite at the top and martensite at the bottom, below the dashed line. The figures shown are (A) Band contrast map, (B) KAM map, (C) IPF map with grain boundaries and (D) inverse pole figure.

The band contrast in figure 4.23 (A) shows that signal strength of the Kikuchi diffraction pattern reduces slightly from the top of the image, especially when the scan reaches the quenched region. Figure 4.23 (B) also shows that the quenched region has a higher dislocation density than the core region at the top of the image. This is expected since martensite forms where quench rate is sufficient to retain carbon atoms within the crystal structure. A martensite lattice is distorted which induces high dislocation density and residual stress and these cause the poor diffraction pattern and lower signal strength seen. Figure 4.23 (C) and (D) show a weak rolling texture since a maximum of 1.83 exists in the 110 orientation. However, a multiplier of only 1.83 means most grains are randomly orientated. There is a minimum in the 111 orientation of 0.49. This suggests the steel is in the austenitic region during rolling and most grains recrystallise after rolling.

5L

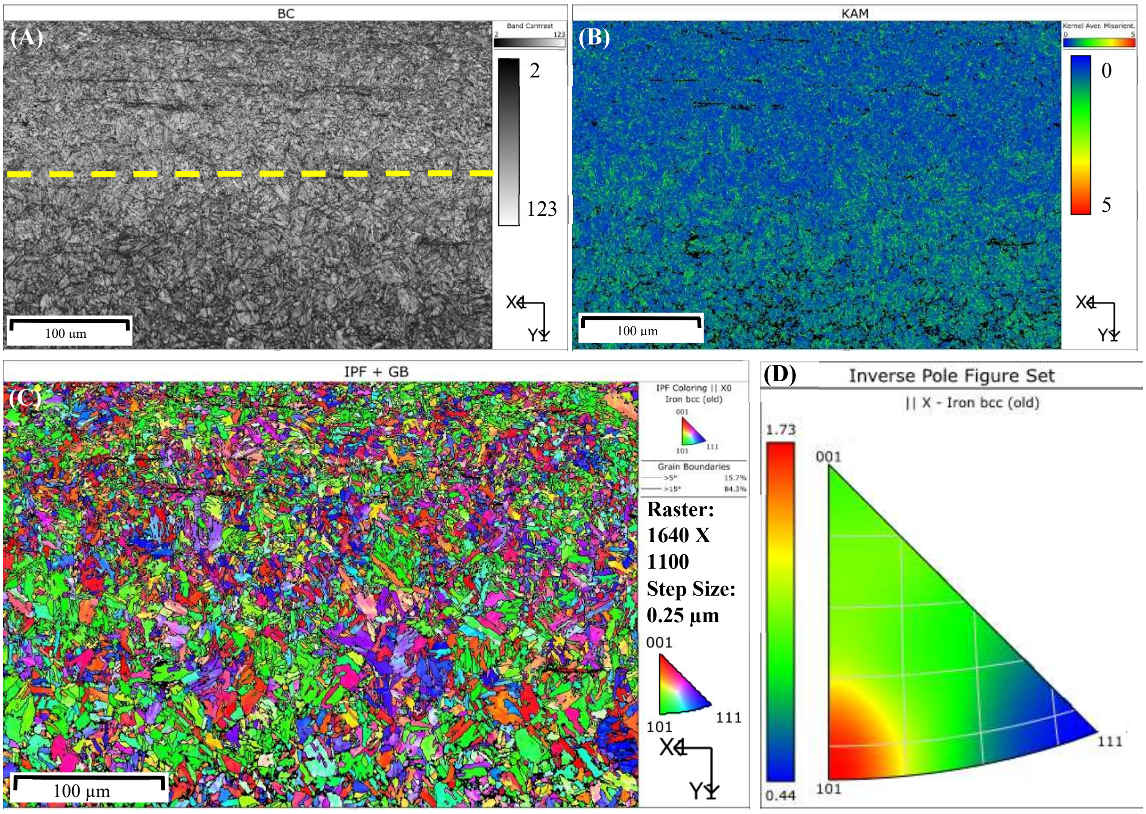

Figure 4.24 EBSD figures for 5L, the consistently processed sample, longitudinal section, at a site in the interface region with ferrite at the top and martensite at the bottom, below the dashed line. The figures shown are (A) Band contrast map, (B) KAM map, (C) IPF map with grain boundaries and (D) inverse pole figure.

The top half of figure 4.24 is the ferrite and pearlite core region, while the bottom half is the quenched edge, with greater dislocation density. Grains in the ferrite region appear finer than the martensite lathes which is unexpected since the ferrite experiences more self-tempering. Lines with poor signal strength are visible, particularly in the core region. These lines are likely to be manganese sulphide inclusions, elongated in the rolling direction, as seen in the section 4.5. An IPF X map is shown in (C) since the rolling direction is in the x axis for longitudinal samples. The key shows that red grains have 001 orientation, green grains are 110 and blue grains are 111. The texture in this longitudinal sample is very similar to that of 5C, it is quite randomised with a slight preference for the 110 orientation, with maxima of 1.73 and minima in the 111 orientation of 0.44. The rolling texture is stronger in the 5C and 5L samples than the other samples, although it is still a relatively weak texture.

6C

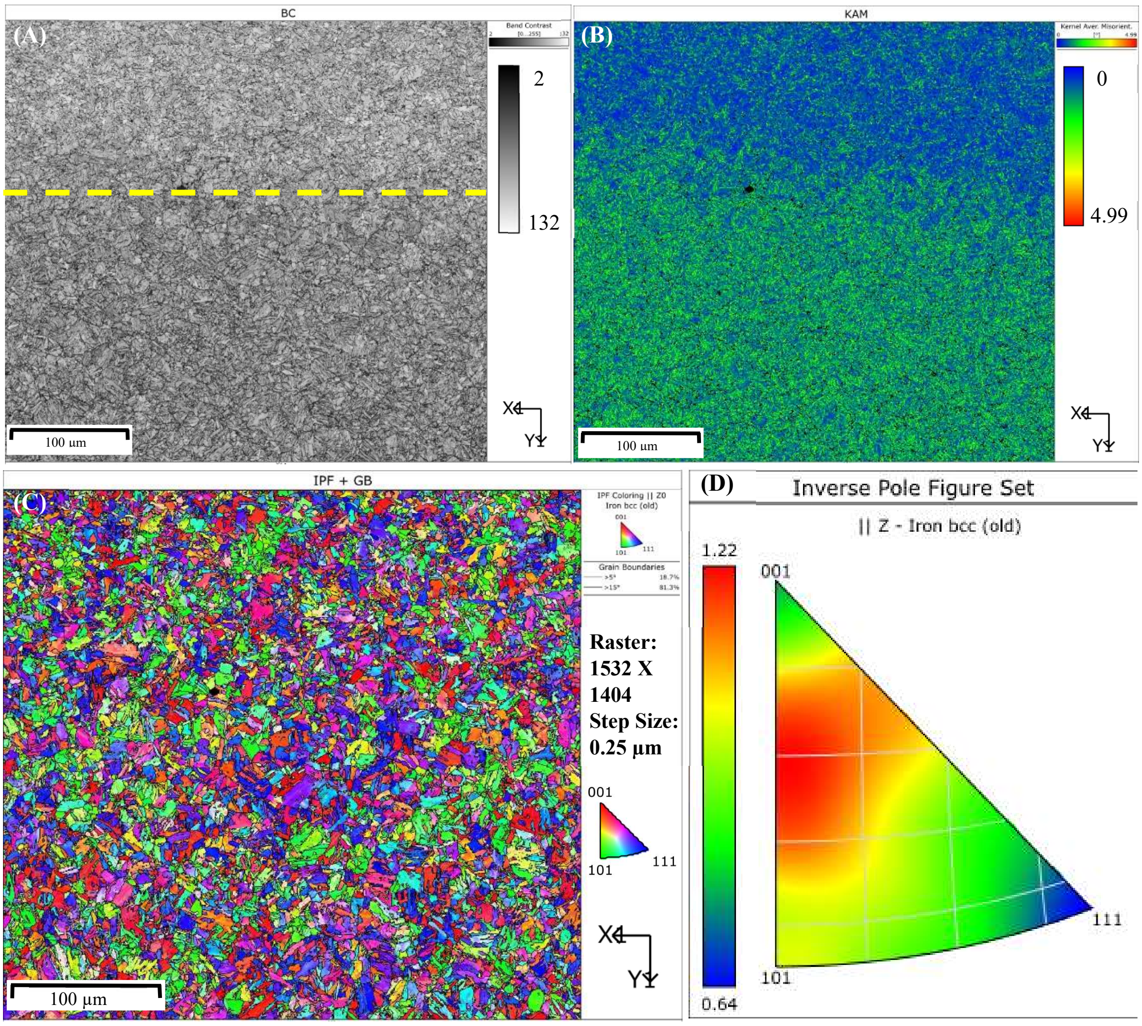

Figure 4.25 EBSD figures for the cross section of coil six, which produced shorter lengths when processed in a twin strand ALB machine. The area mapped is in the interface region with ferrite at the top and martensite at the bottom, below the dashed line. The figures shown are (A) Band contrast map, (B) KAM map, (C) IPF map with grain boundaries and (D) inverse pole figure.

Sample 6C in figure 4.25 shows equiaxed grains, randomly oriented, with low dislocation density in the core region. Whereas the quenched region contains martensite laths with greater dislocation density. Signal strength is relatively strong for the whole map as the band contrast is bright throughout. The inverse pole figure, figure 4.25 (D), has a random distribution of orientation in grains as the maximum points density is only 1.22. Most points are spread between orientation types 001 and 110, while a minimum exists at 111 of 0.64. This texture is more randomised than the texture seen in sample 5.

6L

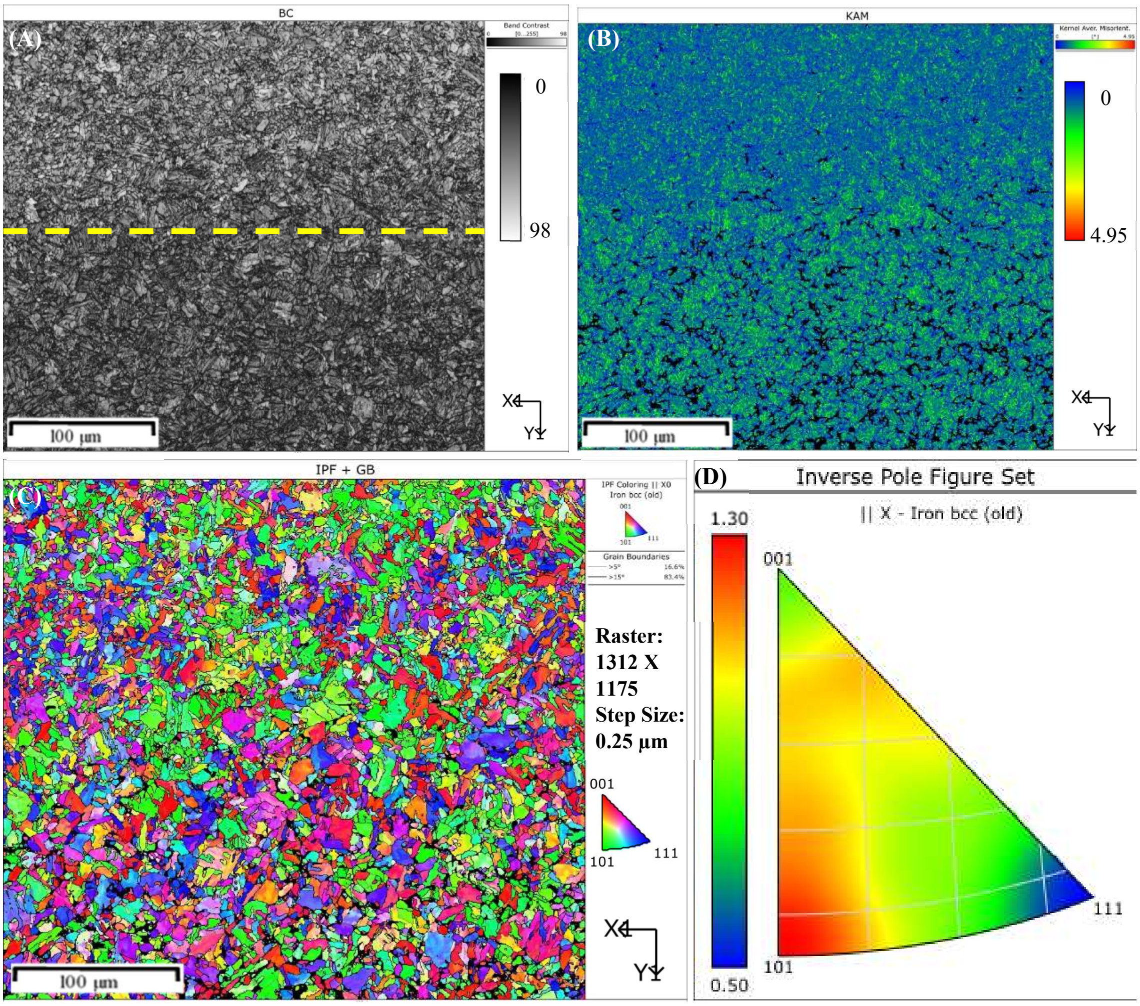

Figure 4.26 EBSD figures for the longitudinal section of coil 6, which produced shorter lengths when processed in a twin strand ALB machine. The area mapped is in the interface region with ferrite at the top and martensite at the bottom, below the dashed line. The figures shown are (A) Band contrast map, (B) KAM map, (C) IPF map with grain boundaries and (D) inverse pole figure.

Signal strength is weaker for sample 6L in figure 4.26, particularly in the quenched region. The band contrast map is less bright and unindexed regions are visible. This may be partly due to the strained crystal structure of martensite as well as inaccuracy in the EBSD operation, such as dynamic focus and beam drift. Nevertheless, the figure displays similar microstructure to the other samples, namely a ferritic core with martensite at the edge, and a relatively randomised orientation distribution with a weak rolling texture. Pole figure maximum intensity is 1.30 at orientation 110 and the minimum is 0.5 at 111. Once again, dislocations in the KAM map are much denser in the martensitic region, making the interface between the core and edge clear in figure 4.26 (B).

<u>7C</u>

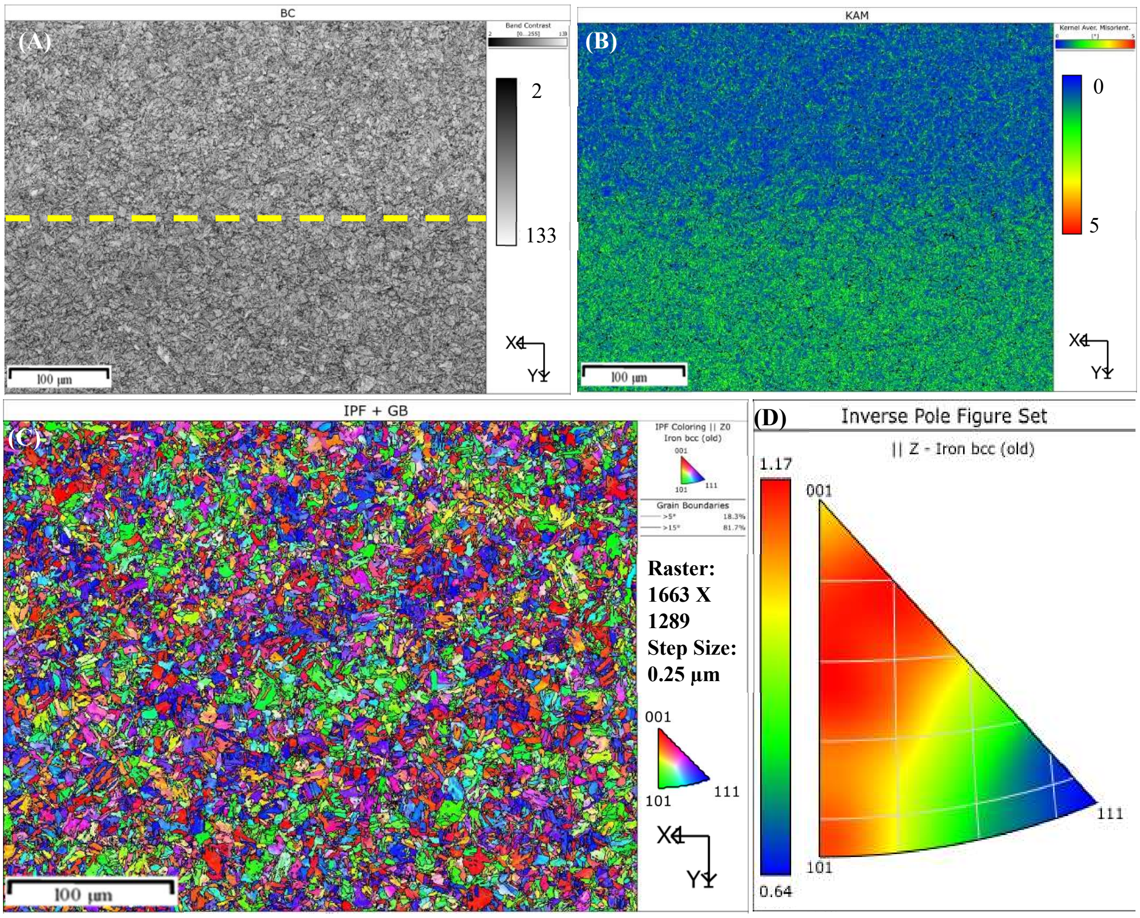

Figure 4.27 EBSD figures for the cross section of coil 7, which produced longer lengths when processed in a twin strand ALB machine. The area mapped is in the interface region with ferrite at the top and martensite at the bottom, below the dashed line. The figures shown are (A) Band contrast map, (B) KAM map, (C) IPF map with grain boundaries and (D) inverse pole figure.

Figure 4.27 (A) shows that the signal strength was relatively high throughout the EBSD scan of sample 7C and the KAM map in (B) shows a clear interface between the ferrite and pearlite region and martensite region as the martensite contains a greater density of dislocations. An IPF Z map is shown in (C) since this is a cross section sample with rolling direction in the Z axis. This shows a randomised texture, which is supported by the inverse pole figure (D). The maxima are spread between 001 and 110 orientations with a multiplier of only 1.17. This is more randomised than the textures seen in samples 5 or 6 since the maxima multiplier is lower and maxima regions are spread between 001 and 110 orientations.

7L

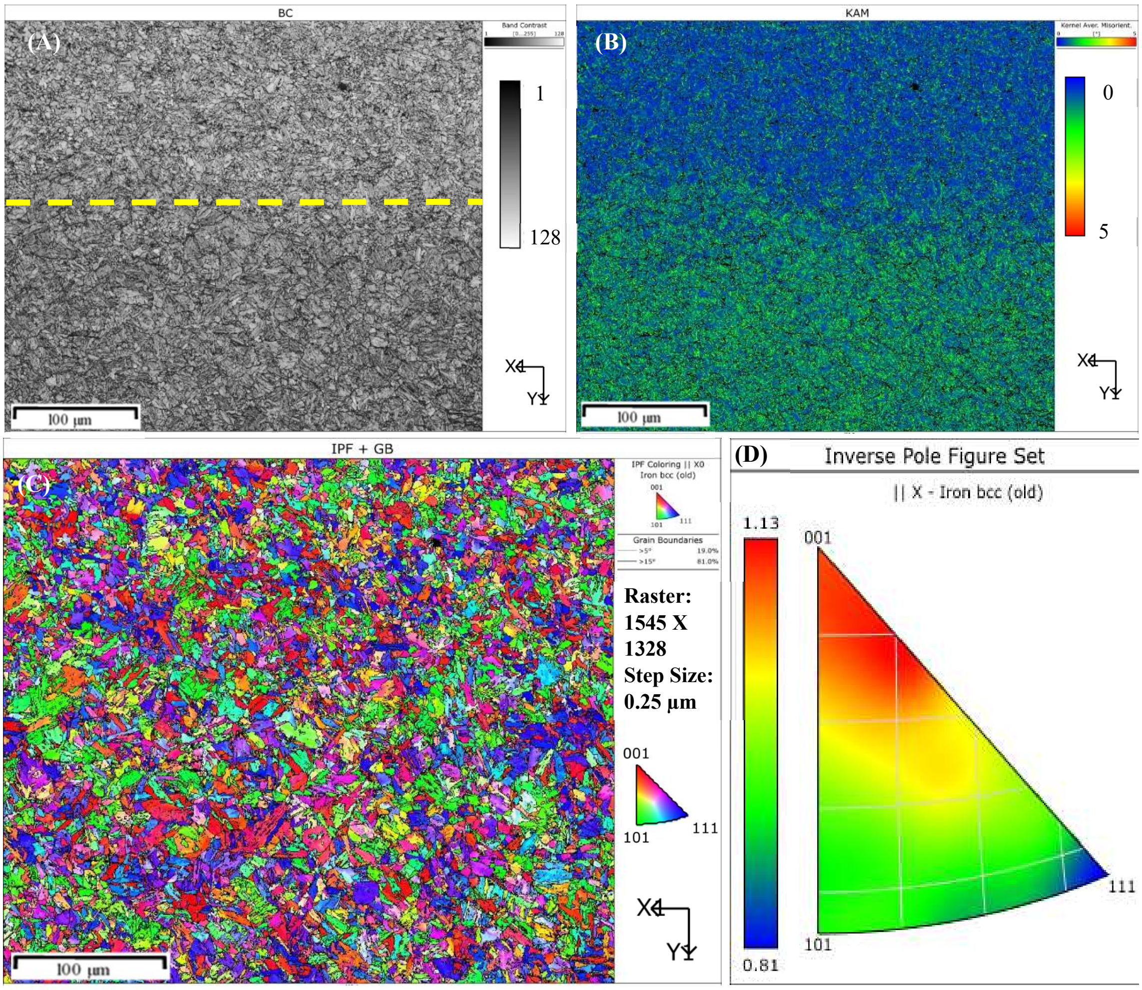

Figure 4.28 EBSD figures for the longitudinal section of coil 7, which produced longer lengths when processed in a twin strand ALB machine. The area mapped is in the interface region with ferrite at the top and martensite at the bottom, below the dashed line. The figures shown are (A) Band contrast map, (B) KAM map, (C) IPF map with grain boundaries and (D) inverse pole figure.

Figure 4.28 shows similar results for sample 7L to those seen for sample 7C. Band contrast (A) shows good signal strength and smaller grains in the ferrite region than in the martensite. The KAM map (B) shows that the core region has a low dislocation density while the martensite region has a high density of dislocations of approximately three – four degrees. There is an even distribution of colours in the IPF map (C) which indicates a randomised texture. The inverse pole figure shows that 001 is a slightly preferred direction but the maximum intensity is only 1.13 so this is close to an even distribution of orientations. A multiplier value of one reflects no preference for or against an orientation.

<u>8C</u>

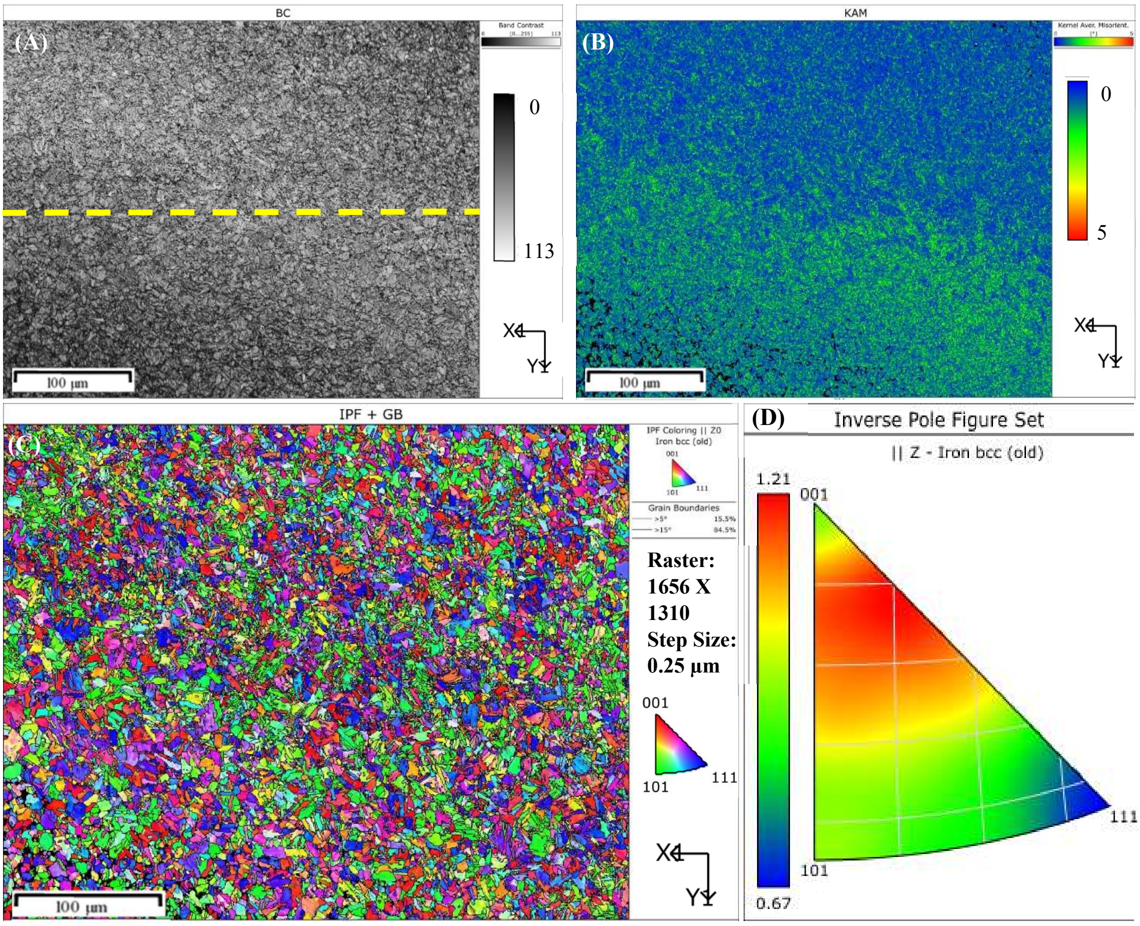

Figure 4.29 EBSD figures for the cross section of coil 8, which displayed twisting when processed using an ALB machine. The area mapped is in the interface region with ferrite at the top and martensite at the bottom, below the dashed line. The figures shown are (A) Band contrast map, (B) KAM map, (C) IPF map with grain boundaries and (D) inverse pole figure.

The signal strength of sample 8C is lower in the top right and bottom left corners of figure 4.29 (A) and there are regions with unindexed points, even after the clean-up procedure has been applied. This is likely to be due to inaccuracy in the setup of the dynamic focus since these are opposite corners and the centre has better signal strength. Like other samples, sample 8C shows consistent misorientations of approximately three to four degrees between martensite laths. The IPF Z map (C) shows no clear orientation preference. The inverse pole figure indicates the site has a very weak preference close to the 001 orientation. However, the texture is very weak, and the sample is quite randomised as the maxima is only 1.21.

8L

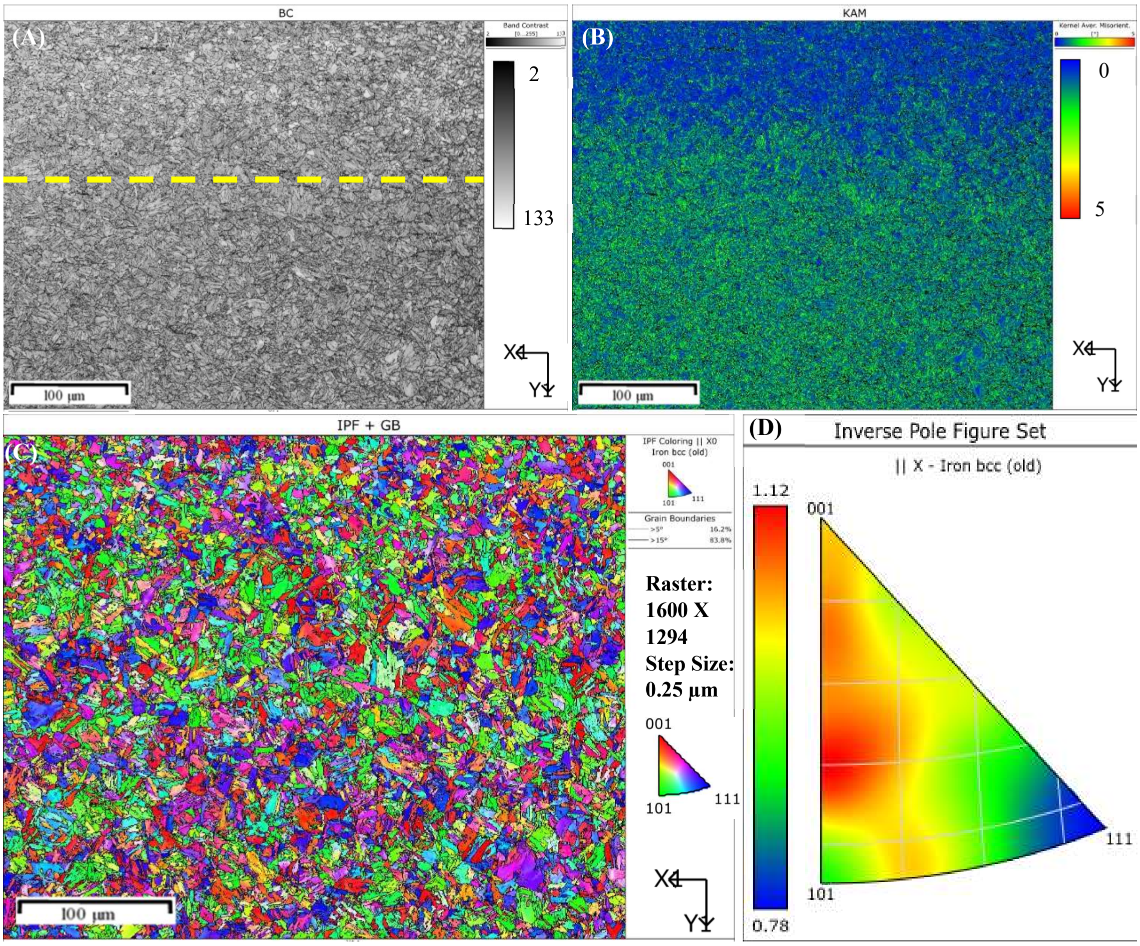

Figure 4.30 EBSD figures for the longitudinal section of coil 8, which displayed twisting when processed using an ALB machine. The area mapped is in the interface region with ferrite at the top and martensite at the bottom, below the dashed line. The figures shown are (A) Band contrast map, (B) KAM map, (C) IPF map with grain boundaries and (D) inverse pole figure.

Sample 8L has a good signal strength across the mapped area in figure 4.30 (A) with some thin unindexed lines in the rolling direction indicating the position of inclusions. The martensite region has a high density of misorientations which are evident in the KAM map (B). A randomised distribution of grain orientations is visible in the IPF X map (C) and inverse pole figure (D), which has a multiplier of 1.12. The maxima are spread between the 001 and 110 orientations with minima in the 111 orientation.

EBSD Summary

Figures 4.23 – 4.30 Show subsets of similar sizes for each sample for visual comparison. These subsets are taken from larger EBSD maps which were used to collect grain and lathe size data. The size of these maps was maximised according to SEM laboratory availability when each sample was scanned to increase reliability in the data. The smallest area mapped is 1640 by 1100 steps which included 12070 grains. So, even the smallest mapped area size contains enough grains to give a reliable representation of the section's microstructure.

Subsets were also created which separate the core and edge regions for individual analysis and comparison. The KAM map was used to find the separate regions, as shown in figure 4.31, which contains the KAM map created for sample 7C with two subsets, the top one is in the core and the lower subset is in the quenched edge.

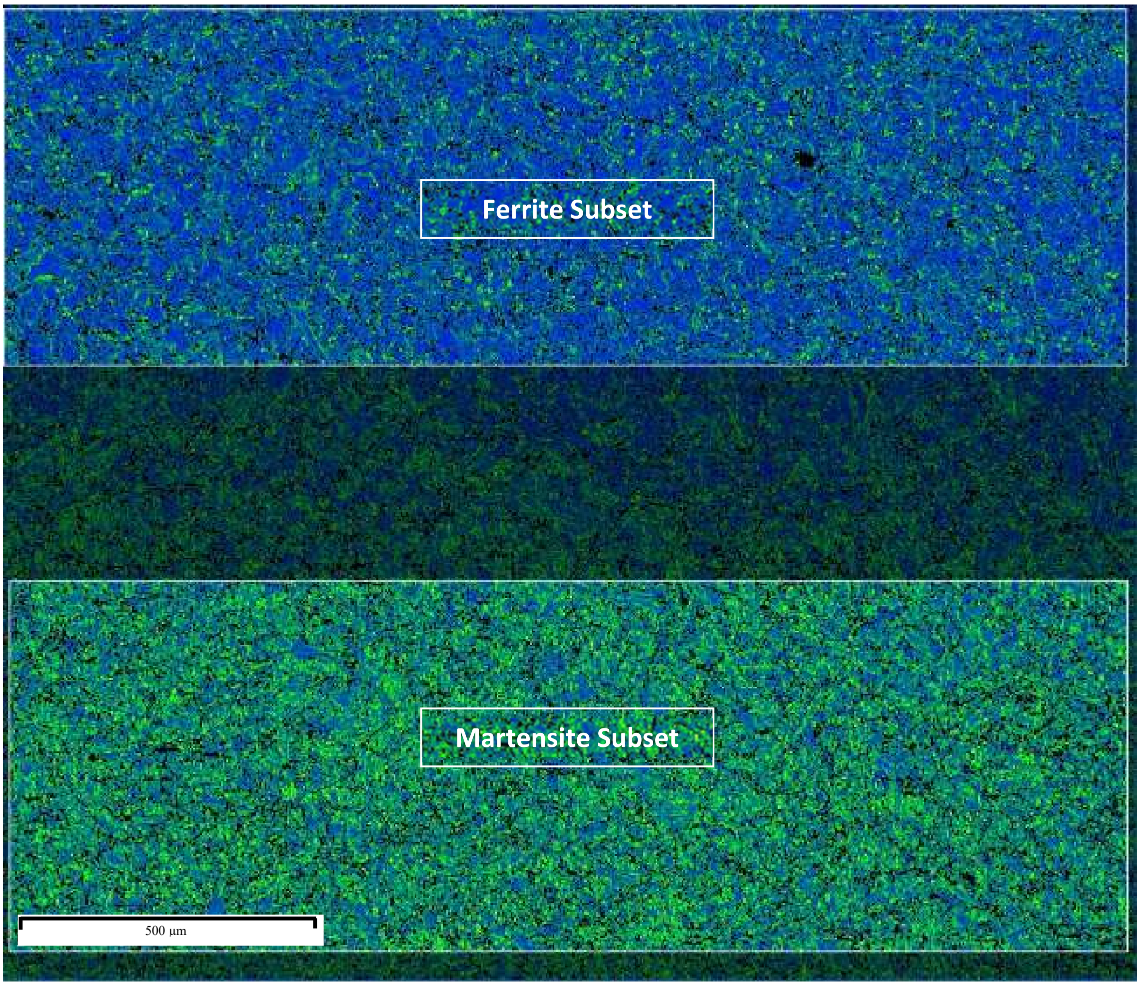

Figure 4.31 KAM map of sample 7C with lighter rectangles indicating the subsets created in the ferrite and the martensite region which were used to analyse EBSD data for each region separately.

The grain data from each sample was used to calculate the average, standard deviation, maximum and minimum values of the ECD. These values are shown for comparison in table 4.22, along with the number of grains in each scan, number of steps in the x and y directions, and the size of the area scanned. Size of area scanned is calculated by multiplying the number of steps in each direction by the step size, 0.25 μm. Due to the step size, grains with ECD smaller than 0.89 μm are excluded, therefore this was the minimum ECD measured for each sample. The table shows that samples have consistent average ECD, ranging between 2.4 – 2.9 μm. There is also no clear difference in average ECD or standard deviation between cross sectional and longitudinal samples. However, maximum ECD is larger for longitudinal than cross sectional samples. For each sample, the maximum grain ECD in the longitudinal section is at least 1.6 μm larger. The number of grains in each mapped area ranges between 12070 and 95123, and sample area ranges between 112750 and 766590 μm².

Entire Sample	Avg ECD (μm)	ECD Standard Deviation	Maximum ECD (μm)	Minimum ECD (μm)	Number of Grains	Number of Steps, X	Number of Steps, Y	Sample Area (μm²)
5C	2.7	2.4	24.0	0.89	12,070	1,634	1,223	124,899
5L	2.6	1.9	25.6	0.89	13,067	1,640	1,100	112,750
6C	2.6	2.0	19.9	0.89	29,671	2,353	1,760	258,830
6L	2.9	2.1	21.9	0.89	53,648	3,923	2,942	721,342
7C	2.9	2.1	22.7	0.89	95,123	4,040	3,036	766,590
7L	2.7	2.1	26.3	0.89	47,276	3,138	2,354	461,678
8C	2.6	1.7	18.2	0.89	31,925	2,353	1,765	259,565
8L	2.4	1.8	20.9	0.89	30,609	2,353	1,765	259,565
Average	2.7	2.0	22.4	0.89	39,174	2,679	1,993	370,652

Table 4.22 Grain size data from EBSD analysis of each sample, including the average, maximum, minimum, and standard deviation values of the equivalent circle diameter (ECD), the number of grains and size of the mapped area.

Table 4.23 shows the grain data results from the core region subset taken from each sample. Average ECD in the core subsets is 2.6 μm, which is very close to the average ECD in table 4.22 for the entire maps, 2.7 μm. Maximum grain size in the ferrite region ranges between 13.1 and 20.5 μm. Samples 6L and 7C have the largest average ECD and there is not a clear difference in grain size between the twin strand pair of samples six and seven. Sample 5 has the smallest average ECD for both sections. The number of grains and sample area is smaller than table 4.23 for each sample because they are subsets taken from the original map. Minimum number of grains is 3084.

The grain data from the quenched edge subsets are shown in table 4.24. There is no clear difference in average ECD between core and edge regions since the average between martensite regions is 2.7 μm which is equal to the entire sample and close to the ferrite subset. However, in the edge region, standard deviation is 2.1 and maximum ECD is 20.6 µm, which are both greater than the core. The core has a standard deviation and maximum ECD of only 1.7 and 17.2 µm, respectively. Number of grains in the edge subset is between 3066 and 27875 and sample area ranges from 33089 to 219186 µm². In the martensite regions, ECD measures individual lathes with orientation boundaries of greater than 10° whereas in the core region, orientation boundaries of greater than 10° are between grains.

Ferrite Subset	Avg ECD (µm)	ECD Standard Deviation	Maximum ECD (µm)	Minimum ECD (µm)	Number of Grains	Number of Steps, X	Number of Steps, Y	Sample Area (µm²)
5C	2.3	1.5	19.5	0.89	5,620	1,630	335	34,128
5L	2.4	1.5	16.7	0.89	6,381	1,614	414	41,762
6C	2.5	1.7	15.9	0.89	6,363	1,815	425	48,211
6L	2.9	2.0	19.4	0.89	20,937	3,481	950	206,684
7C	2.9	2.0	20.5	0.89	24,656	3,232	904	182,608
7L	2.8	1.9	18.8	0.89	14,985	2,737	800	136,850
8C	2.5	1.6	13.4	0.89	8,352	1,560	591	57,623
8L	2.6	1.7	13.1	0.89	3,084	1,300	300	24,375
Average	2.6	1.7	17.2	0.89	11,297	2,171	590	91,530

Table 4.23 Grain size data from EBSD analysis of the core region subset of each sample, including the average, maximum, minimum, and standard deviation values of the equivalent circle diameter (ECD), the number of grains and size of the subset area.

Martensite Subset	Avg ECD (µm)	ECD Standard Deviation	Maximum ECD (µm)	Minimum ECD (µm)	Number of Lathes	Number of Steps, X	Number of Steps, Y	Sample Area (µm²)
5C	2.7	2.2	18.8	0.89	4,101	1,630	400	40,750
5L	2.7	2.3	25.6	0.89	3,066	1,598	336	33,558
6C	2.6	2.0	19.9	0.89	6,970	1,805	567	63,965
6L	3.0	2.2	21.9	0.89	15,023	2,920	1,040	189,800
7C	2.9	2.1	22.7	0.89	27,875	3,608	972	219,186
7L	2.7	2.2	23.1	0.89	11,806	2,406	812	122,105
8C	2.7	1.8	14.0	0.89	5,220	1,600	449	44,900
8L	2.6	2.0	19.2	0.89	3,920	1,285	412	33,089
Average	2.7	2.1	20.6	0.89	9,748	2,107	624	93,419

Table 4.24 Grain size data from EBSD analysis of the edge region subset of each sample, including the average, maximum, minimum, and standard deviation values of the equivalent circle diameter (ECD), the number of grains and size of the subset area.

From the EBSD data in this study, the texture in samples has been found to be quite randomised with a weak rolling texture in samples 5C and 5L. There is a high density of thin misorientations in the edge region, which is characteristic of lathes in martensite. Average ECD is approximately 2.6 µm and no clear difference in grain size can be seen between the samples or subset regions. However, the maximum and standard deviation values of ECD are greater in the martensite regions.

4.4 Dimension Analysis

Stitched images of each sample obtained using the Carl Zeiss Axio Observer Z1M were used to measure dimensional accuracy in the rebar. Dimensional variation potentially leads to differences in rebar processing, particularly the aspect ratio and thickness, so consistency of the samples was investigated. Figure 4.32 shows the stitched images of each cross-section sample annotated with the dimensions which were measured using ImageJ software. A darker region is visible around the edge of each cross section, approximately 1 mm thick. This is the quenched region and is especially visible in the 8C sample.

The dimensions measured from stitched images were used to calculate the aspect ratio for the diameter between ribs, where there are no ribs, and across the tempered core. The dimensions these were calculated from are shown in equations 4.2 to 4.5.

$$Rib\ to\ Rib\ Aspect\ Ratio = \frac{Height}{Width} \qquad \text{Eq. 4.2}$$

$$Diameter\ Aspect\ Ratio = \frac{Diameter\ A}{Diameter\ B} \qquad \text{Eq. 4.3}$$

$$Core\ Aspect\ Ratio\ 1 = \frac{Core\ Diamter\ A}{Core\ Diameter\ B} \qquad \text{Eq. 4.4}$$

$$Core\ Aspect\ Ratio\ 2 = \frac{Core\ Diamter\ C}{Core\ Diameter\ D} \qquad \text{Eq. 4.5}$$

The images in figure 4.32 are not circular since there are ribs on the surface of the rebar, which are visible around the edge of these cross sections. There are four longitudinal ribs in each cross section and the number of transverse ribs visible depends on where the rebar was cut. Since the number and height of transverse ribs are designed to vary along the rebar, only the longitudinal ribs were measured.

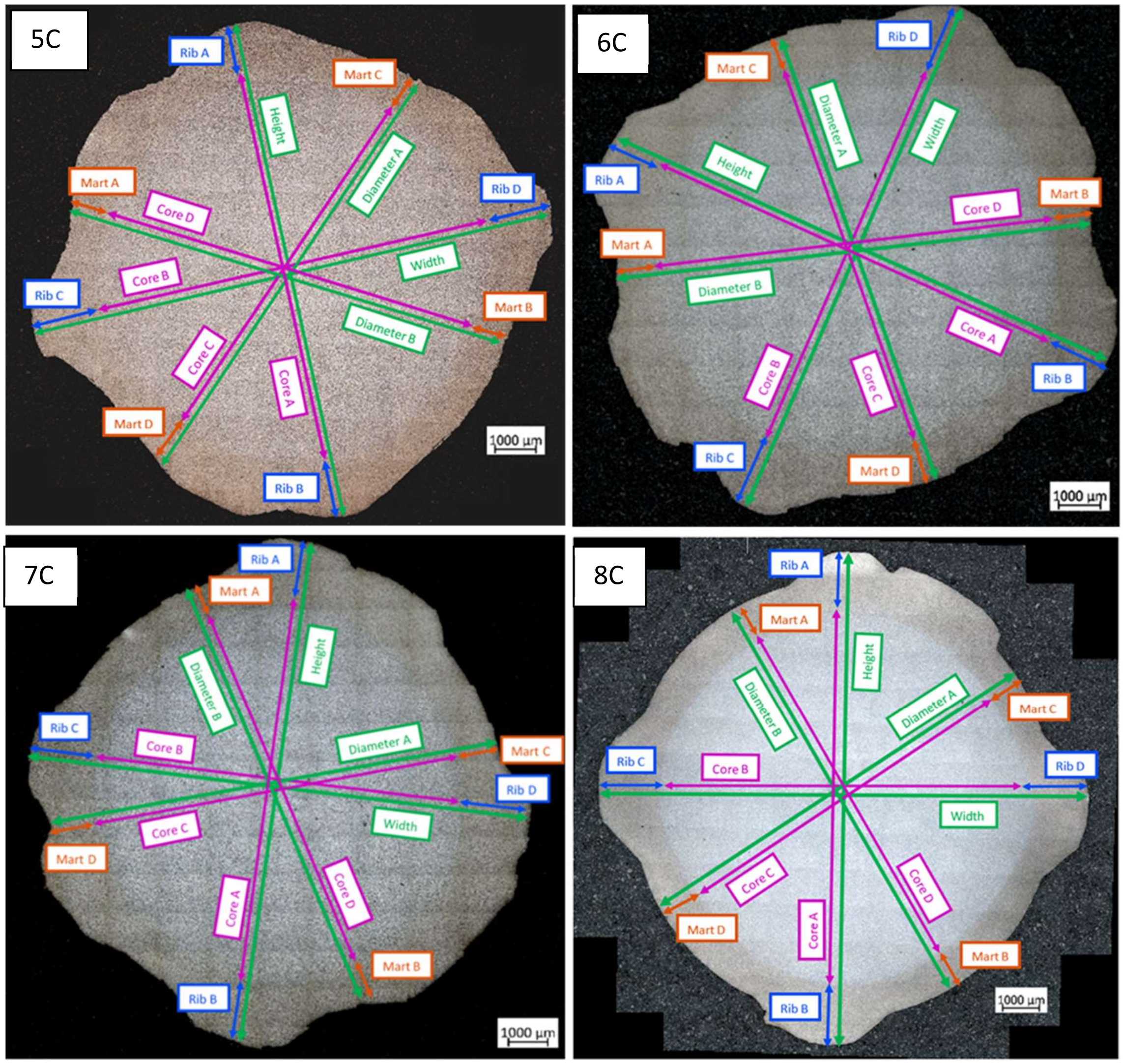

Figure 4.32 Stitched macroscopic images at 10X magnification, annotated with the dimensions measured using ImageJ software program, for the cross-section samples (A) 5C, (B) 6C, (C) 7C and (D) 8C.

Sample	Height (mm)	Width (mm)	Rib to Rib Aspect	Diameter A (mm)	Diameter B (mm)	Diameter Aspect	Core Diameter A (mm)	Core Diameter B (mm)	Core Aspect 1 (A/B)	Core Diameter C (mm)	Core Diameter D (mm)	Core Aspect 2 (C/D)
5C	13.4	14.1	0.95	12.3	12.1	1.02	10.6	10.9	0.97	10.0	10.2	0.98
6C	13.3	13.2	1.00	11.4	11.6	0.98	9.1	9.7	0.94	9.7	9.9	0.98
7C	13.5	13.5	1.00	12.1	12.0	1.0	10.0	9.7	1.04	9.9	10.2	0.97
8C	13.2	13.1	1.01	11.5	11.7	0.98	9.9	10.1	0.98	9.4	9.7	0.97
Standard Deviaton	0.10	0.36	0.02	0.39	0.20	0.02	0.53	0.50	0.04	0.22	0.23	0.01

Table 4.25 Results from measurement of diameters at longitudinal ribs, in between ribs, and the tempered core as well as the aspect ratios calculated from each dimension for the four samples that displayed unique processing characteristics.

The dimensions presented in table 4.25 show that height varies between 13.2 mm and 13.5 mm while width varies between 13.1 mm and 14.1 mm. The width and height are similar for each sample, except for sample 5C which has a larger width, 14.1 mm, compared to its height, 13.4

mm. This is shown by the rib-to-rib aspect ratio, ratio of height to width, which is approximately one in samples 6, 7 and 8. Sample 5 however, has a 0.95 aspect ratio. Diameters A and B have close values between each sample as the diameter aspect ratios range between 0.98 to 1.02. This means that, excluding the ribs, the surface of each sample is close to circular for each cross section. Finally, the tempered core appears to vary more in core A and B, which are the tempered cores measured between ribs, than core C and D, which are measured where there are no ribs. Cores A and B have standard deviation of 0.53 and 0.50, respectively, whereas standard deviation in cores C and D is 0.22 and 0.23, respectively. Despite this variation, the aspect ratio between both pairs of measurements is mostly close to one. Core aspect one of sample 6C is 0.94 which is the least circular core measurement of the samples, but the other dimensions of 6C are all much closer to one. Similarly, sample 5C has an aspect ratio of 0.95 between height and width, but its other dimensions are more circular as the aspect ratios are closer to one.

Sample	Average Quench Thickness (mm)	Quench Deviation	Average Rib Height (mm)	Rib Height Deviation
5C	1.00	0.13	1.48	0.13
6C	1.08	0.06	1.73	0.07
7C	1.08	0.10	1.71	0.09
8C	1.02	0.08	1.58	0.10

Table 4.26 Results of the average thickness of the quenched region and height of longitudinal ribs around the cross section of rebar, and the calculated standard deviation of each measurement for the four samples that displayed unique processing characteristics.

Table 4.26 shows that the quenched edge is approximately one mm thick and does not show much variation between the four samples. On the other hand, rib height varies more between samples as height ranges between 1.48 and 1.73 mm. The pair of twin strand samples, 6C and 7C, both have rib height of approximately 1.7 mm. Rib height was measured from the edge of the tempered core. So, subtracting the thickness of the quenched region from the rib height value would give rib height from the surface in between ribs. Standard deviation varies by approximately five to ten percent of both the quench thickness and rib height values.

4.5 Micro Hardness Testing

Figure 4.33 shows the locations of indents created by each microhardness test point on a cross section sample. There are three lines of indents across the rebar diameter. Each line begins with point one at an edge and moves across the diameter to the opposite edge. Depending on the location of ribs, either 12 or 13 points can fit, each one millimetre apart.

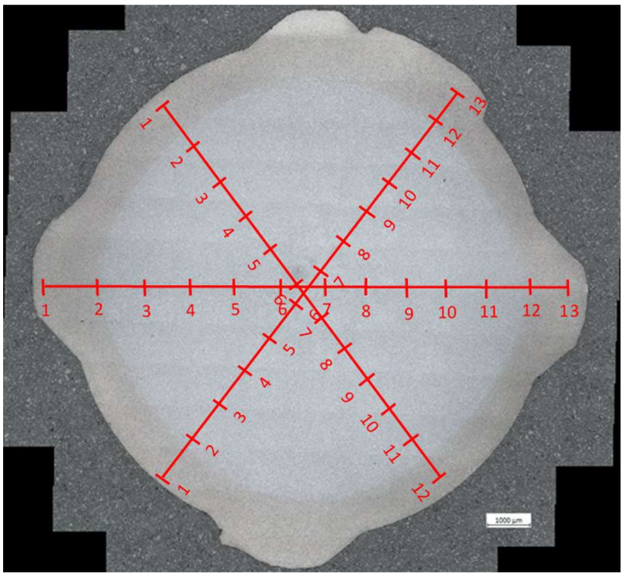

Figure 4.33 Illustration of the locations of microhardness test points on a cross sectional sample. Three lines of 12 – 13 points across the diameter measure hardness through the sample.

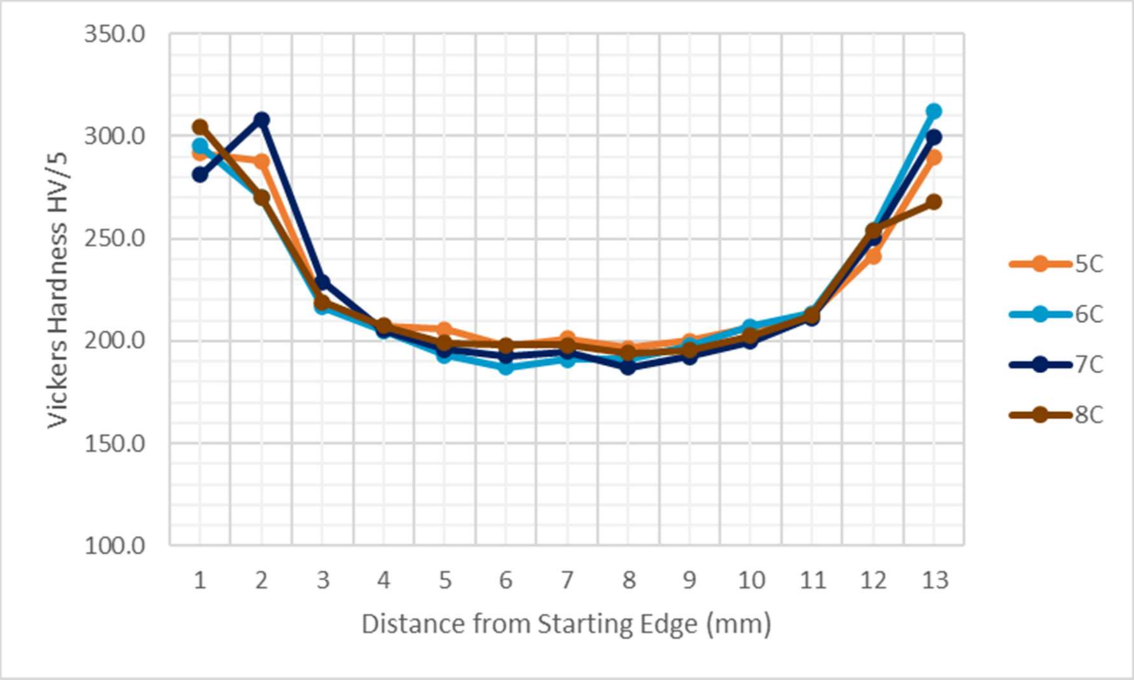

Figure 4.34 Average Vickers hardness measured at points spaced one millimetre apart across cross section samples of rebar using a load of five kilograms with a ten second dwell time.

The results of microhardness testing across the cross-sectional samples are shown in figure 4.34. The average of the three lines measured per sample are calculated at each point. The graph shows that each sample has similar hardness through the sample. All samples have greater hardness at the edges, where the steel is affected by quenching, and hardness is lower in the middle, between points 3 – 11 mm from the starting edge. The first and last points (1 and 13) range between 267 and 312 HV/5, whereas the points between 3 and 11 mm from the starting edge range between 187 and 229 HV/5. There are small differences between samples, particularly near the edges; 8C has lower hardness at point 13 and 7C has greater hardness at point 2. This may be due to the location of ribs determining whether these edge points are in the quenched region.

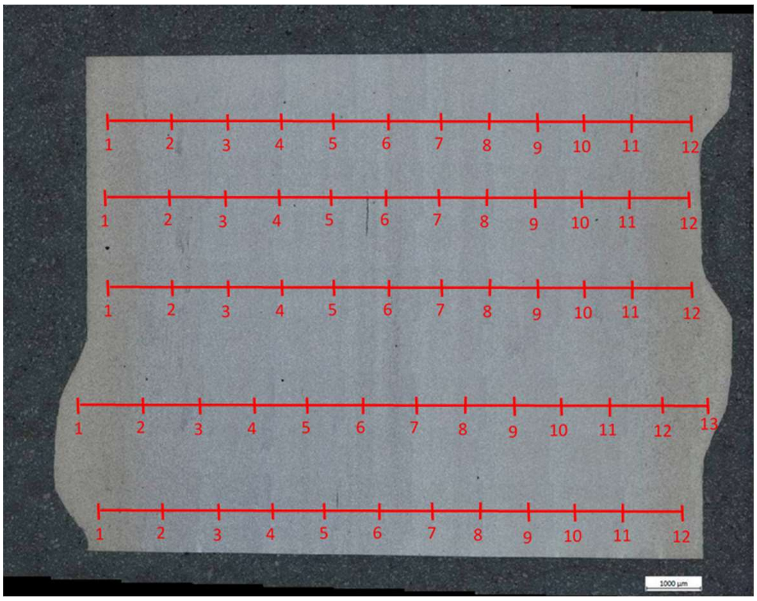

Figure 4.35 Illustration of the locations of microhardness test points on a longitudinal section sample. Five lines of 12 – 13 points across the diameter measure hardness through the sample.

The locations of microhardness tested points for longitudinal samples are shown in figure 4.35. These lines of indents are parallel to each other for longitudinal samples so five lines could be used in the sample without any points being close enough to influence other points through work hardening the area. Thus, the longitudinal samples provide more reliable results than the hardness testing on cross sectional samples.

Figure 4.36 presents the results of hardness testing on longitudinal samples and shows similar results to those seen for cross section samples in figure 4.34. The quenched edges are harder than the core. Points 1 mm and 12 mm - 13 mm from the starting edge are between 270 - 290

HV/5, while points between 3 mm and 10 mm from the starting edge range by 180 - 210 HV/5. Only one of the longitudinal samples have 13 points, the others have only 12 across the diameter whereas all the cross-section samples fit 13 points across the samples. This is likely to be because the longitudinal ribs are not always visible in longitudinal cuts, depending on the location of the cut. Since these ribs are larger than transverse ribs, 13 points are likely to have been recorded where these ribs are present.

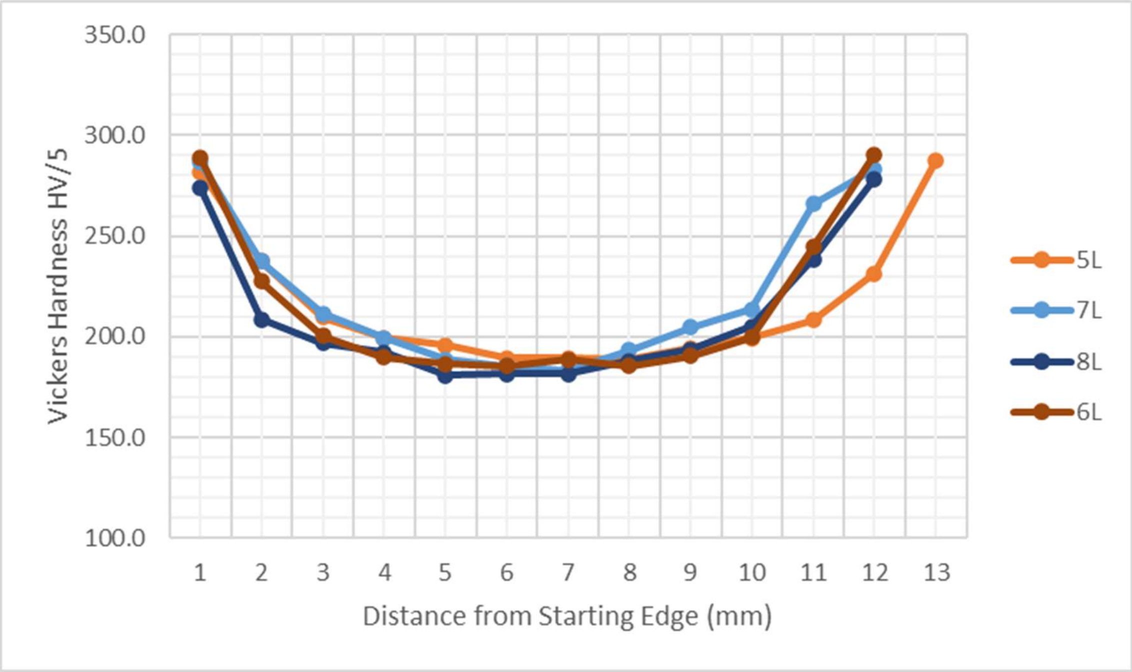

Figure 4.36 Average Vickers hardness measured at points spaced one millimetre apart across longitudinal section samples of rebar using a load of five kilograms with a ten second dwell time.

4.6 Discussion

4.6.1 EDS Discussion

The results of EDS analysis showed relatively consistent composition between all the samples. All compositions were within the maximum limit specified by BS4449:2005 and alloying elements did not vary by more than 0.1 wt% [11]. Therefore, the evidence does not suggest that changes in composition are a major cause of the differences in processing characteristics displayed by each of the samples.

The sample size is very small so cannot represent the whole 2.2 km coil. EDS data for each sample was collected from three micrographs at 1000X magnification on the same plane. Also, the processing characteristics that were seen in the four coils that samples were taken from may not be present in the samples. The plane that micrographs were taken from may not contain the unique properties causing the processing characteristics. Therefore, planes at set distances throughout coils should be analysed and the location samples are taken from must be recorded to increase the likelihood of observing the processing characteristics.

4.6.2 SEM Discussion

SEM micrographs of sample cores showed ferrite and pearlite grains with manganese sulphide inclusions. Conversely, the edge regions contain martensite with manganese sulphide inclusions. This martensite edge is due to the quenching process. Quenching causes austenite near the rebar surface to rapidly cool, which prevents sufficient carbon atoms from diffusing out of the crystal structure. As a result, a highly strained body centred tetragonal forms, which is known as martensite.

Manganese sulphide inclusions found were circular in cross section planes and elongated in the rolling direction in longitudinal planes. These inclusions have been elongated by the rolling process. The elongation is not visible in cross section samples since the rolling direction is in the Z-axis for these micrographs. Grains in the core and quenched regions are generally equiaxed, which infers the steel was above the eutectoid temperature when rolled. The steel fully recrystallizes after rolling so ferrite, pearlite, and martensite would subsequently form, unaffected by the previous rolling process. Therefore, these are primary inclusions since they are formed above the eutectoid temperature and deform plasticly at the rolling temperature.

From the SEM micrographs in this study, all samples have similar microstructure and no clear differences in microstructural properties have been determined as causes of the processing characteristics. However, there are small differences found between the samples, such as grain size and percentage area of inclusions. Average grain diameter measurements in the core range between 3.61 and 4.47 µm while inclusion area percentage ranges from 0.2 to 0.34 percent. These could potentially affect processing, but the differences seen are small, and more evidence would be needed to conclude whether these affect the processing characteristics. More coils with the same processing characteristics should be tested to see if these differences are repeated for the same characteristics.

Although only a small grain diameter variation was found, grain size is expected to vary along the length of a coil. Grain size is expected to change within coils since the coil cut up reports in section 3 show tensile strength variations along coils. This is likely to be due to different cooling rates allowing more grain growth in the core of a coil than in the exterior sections. Such variations along the length of coils would not have been detected in the SEM investigation since only two samples were analysed per coil and their location within the coil was not recorded. Only small variations in average grain diameter were seen, from 3.61 to 4.17 µm, so samples collected may have been located at similar regions in their coils. Since a relationship between coil position and strength properties has been seen in section 3, samples should be taken from specific locations in the coil to test the prediction that grain size is smaller in the core, where yield strength is smaller.

If grain size is found to cause the tensile strength variation along coils, this could be a key factor effecting the changes in processing characteristics in coils. As tensile strength changes, processing machines may require adjustment to straighten and bend the finished coils consistently. Twin strand machines could also be affected by tensile strength if a certain strength of metal is gripped and pulled by drive rollers with less slip than metal with different tensile strength.

A small difference in the percentage area covered by manganese sulphide inclusions was seen between the pair of coils which were processed in a twin strand machine, samples six and seven. Sample six had 0.29 and 0.37 percent inclusion area in samples 6C and 6L, respectively. On the other hand, inclusion area in sample seven was found to be 0.24 and 0.23 percent for 7C and 7L, respectively. Manganese sulphide inclusions often increase ductility and reduce tensile strength, so an increase in the percentage area could make the steel less strong which may affect processing characteristics. For example, this difference might be the cause of different lengths being pulled through the ALB machine as drive roller teeth grip a coil with a certain strength better than other strengths. The difference seen between samples is small and the area tested cannot represent the entire 2.2 km coil. In addition, the colour threshold technique used to measure inclusion percentage area often includes some grain boundaries and surface defects as these have a similar colour to the inclusions. This reduces the accuracy of the recorded value and may be the reason for the differences seen between samples.

The samples tested are limited and it is possible that large variations could be seen by testing a much larger sample range. *Celsa Steel UK* coils of 12 mm rebar are approximately 2.2km when unrolled. Two samples, a cross section and longitudinal section, approximately 12 X 12 mm each were taken from each 2.2 km coil and viewed using SEM techniques. Therefore, the microstructure found may not represent the rest of the coil. In future, samples taken at set lengths through the coil would provide a more reliable representation of the whole coil microstructure. This was outside the scope of this project as it would require whole coils to be set aside and many samples to be examined. Also, when this study began, the differences along coils found from the coil cut up reports in section 3 were not known, so the importance of testing properties throughout a coil had not been realised.

4.6.3 EBSD Discussion

Like the SEM micrographs, EBSD scans showed a region of martensite close to the edge of the steel, and a mixture of ferrite and pearlite grains further towards the middle for all samples. From the EBSD data, ECD has been characterized as approximately 1.7 µm and 2.1 µm for the ferritic core and quenched martensite regions, respectively. KAM maps show that martensite has a greater density of misorientations than the ferritic region, and the texture in both regions is relatively randomised. These results suggest that the microstructure created by the quenching process is relatively consistent and does not cause the unique processing characteristics of the samples.

ECD in the ferritic core was expected to be larger than in the martensite since the core is tempered and ECD measures martensite lathes. However, the EBSD results show martensite average ECD is 0.4 µm larger than the core ECD. Grain size could be larger closer to the centre of the bar because the core region that was mapped is within 250 µm of the martensite region. These ferrite and pearlite grains would have been cooled at a rate close to the required rate for quenching and would experience less tempering than the centre. This may be the reason that the ECD measured for the ferrite and pearlite was smaller than the martensite. Larger grains might be found further towards the centre of the rebar.

Texture variation found between samples are small and do not show clear links to any of the changes in processing characteristics between samples. All samples have a relatively randomised texture as the maximum multiplier seen for an orientation was 1.83. Sample 5 had a weak preference for the 110-type orientation, with maximum concentration of 1.83 and 1.73 in samples 5C and 5L, respectively. These 110 textures form due to rolling as grains become elongated in the rolling direction. Since the steel is hot rolled, the grains mostly recrystallise without a preferred orientation, but some residual texture must remain to create this weak rolling texture seen in samples 5C and 5L.

The weak rolling texture seen in sample 5 may be due to a lower rolling temperature than the other samples as this could cause more residual texture to remain after cooling. This lower rolling temperature could be responsible for changing properties that effect the steel post processing behaviour. Patel and Wiltshire found that, for Nb HSLA steel, a rolling temperature close to, but above the austenite to ferrite transformation temperature, improved consistency of properties along the coil. Therefore, a lower temperature could be the reason for the stronger rolling texture seen in sample 5 and the consistent processing behaviour seen in this sample. However, neither the rolling temperature for sample 5, nor the effects of rolling temperature on Celsamax coils are known.

Both microscopy techniques measure the average diameter of grains in the tempered core region. However, core grain diameter value calculated from EBSD was smaller than the results of MLI results from SEM micrographs. Average ferrite grain diameter calculated was 3.89 µm from the SEM technique, and 2.6 µm from the EBSD data and for each sample, the SEM value was at least one micron larger. One reason the EBSD data may give smaller values is because some misorientations within grains, such as martensite lathes and pearlite lathes, were characterised as separate grains by the EBSD software. A grain boundary was defined in the software by a misorientation greater than 10°. Any misorientations within a grain that were greater than this would be classed as a separate grain, which would have reduced the recorded ECD size. On the other hand, the SEM calculated value may be larger since MLI measurement is a manual technique and may have excluded some small grains. If grain boundaries were not clearly visible enough, they would not be noticed so less grains would be counted thus increasing the average grain size. Also, EBSD images were taken at the interface between core and quenched regions, so grain size was calculated for a subset of the core less than 250 µm from this interface. This region may cool faster and experience less tempering than the centre. This may create smaller grains in the core closer to the interface with martensite than in the centre of the core region. Both the ECD and MLI techniques suggest a strong bias toward the imposed minimum grain size.

The ECD technique had a much larger standard deviation and sample size than the MLI technique. Standard deviation for the MLI and ECD methods were 0.21 µm and 2.0 µm, respectively. ECD of ferrite was measured from a subset of a 100 X magnification scan which included a minimum of 3084 grains. Conversely, MLI was calculated from 30 lines of grains from three different 1000 X magnification micrographs. Although ECD has a large standard deviation, it is calculated from a larger number of grains so has a more reliable source of data. However, it is likely to be changed by counting misorientations as individual grains and a small number of very large grains, since the maximum grain diameter in ferrite was 20.5 µm.

4.6.4 Dimension Measurement Discussion

Dimensional analysis using ImageJ software to measure stitched images of cross section samples showed that height is similar in size to the width for all samples, except 5C. The rib-to-rib aspect ratio is 1.00 – 1.01 for samples 6C, 7C and 8C but sample 5C had a ratio of 0.95 as the height was 13.4 mm and width was 14.1 mm. It is unknown how much a difference in width of 0.7 mm will change the processing characteristics, but it could affect the force required to straighten and bend the coil. If dimensions vary along a coil, frequent adjustment could be required. Also, greater rebar thickness is likely to increase wear on processing machines.

Results showed that width appeared to vary more than height between samples. Height varied between 13.2 to 13.5 mm while width ranged from 13.1 to 14.1 mm. The height is created by the roller spacing between the grooves in the final rollers which create the ribbed profile. On the other hand, ribs at the width are created as excess steel is forced out between the space between the rollers. If steel feed into the rollers varies, the amount of steel forced out at the sides increases or decreases, so the width varies while height should remain constant. This may be the reason width measurements vary more than height.

Many height and width measurements were outside of the product limits, but this does not appear to affect coil processing. *Celsa Steel UK*'s control limits for both height and width of Celsamax rebar is between 12.7 mm and 13.3 mm. Many of the measured width and heights are greater than the upper limit. Since each coil was only measured in one location, this measurement does not reflect the whole coil and the rest of the coil may be within the limits. The measurement of sample 5C is furthest above the upper limit but this sample was processed without need for frequent processing adjustments. This suggests that being outside the control limits may not affect processing. Providing the dimensions are consistent along the coil, once the processing machine is set up, it should not require frequent adjustment.

The surface diameter measured was close to the target in the 5C and 7C samples, but samples 6C and 8C are larger. The *Celsa Steel UK* target for the diameter at the surface where ribs are not present is 12 mm. Samples 5C and 7C measurements ranged between 12.0 mm and 12.3 mm, whereas samples 6C and 8C ranged between 11.4 mm and 11.7 mm. These smaller diameters in 6C and 8C correspond to more accurate measurements of height and width. Furthermore, width and height for samples 5C and 7C were too large but their diameter measurements are close to the target. This suggests the rib height could be too large as both measurements cannot be achieved together. All samples have relatively circular diameters as aspect ratio ranges from 0.98 to 1.02.

The diameters of the tempered core regions measured for all samples range from 9.1 mm to 10.9 mm and have a standard deviation of 0.42. The core region aspect ratios range from 0.94 to 1.04. Martensite was found to be approximately one mm thick, with a standard deviation of 0.09. Average rib height was 1.48 for 5C and 1.58 for 8C whereas samples 6C and 7C were 1.73 and 1.71, respectively. This rib height measured from the interface between the core and quench regions, to the surface of the rib. So, subtracting the approximate martensite thickness, one millimetre, shows that the rib surface is between 0.48 and 0.73 mm above the lower rebar surface. There is no relationship seen between the height and width and the rib height, since samples 5C and 7C have largest diameter but 6C and 7C have the largest rib height. Therefore, for the samples measured, rib height varies independently from the rebar diameter.

The dimensions of samples recorded show that dimensions vary outside of the tolerance. Increasing the number of samples measured from each coil could better represent the processing characteristics seen in those coils. One cross section has been measured from each coil and section 3 showed that properties can vary along a coil. Each sample of the rebar was taken close to where the processing characteristics were found, however it is still not known if these samples contain the properties that caused the post processing characteristics. The results show that variation in dimensions of at least one millimetre exist for width. This variation should be investigated to determine the effect on processing characteristics. Taking many measurements along coils and around sections that displayed the processing characteristics could better represent the effects of dimensional changes but was outside of the scope of this study. Measuring along whole coils would require sampling at set distances, while recording the processing behaviour for comparison.

For the pair of coils which were processed simultaneously in a twin strand ALB machine, it was found that the rebar which produced longer lengths was slightly larger at the measured cross section. The height and width were 0.2 mm and 0.3 mm larger for sample 7C than 6C, respectively. Sample 7C is from the coil which produced longer lengths when both coils were pulled through drive rollers simultaneously to produce the same lengths. Since sample 7C was larger, it could have pushed the drive rollers apart to fit through. This might cause the other coil to make less contact with the drive rollers and slip more than the larger coil. However, since only one sample was measured for each processing characteristic, the size difference may not exist for other coils with this twin strand issue. Also, a size difference of 0.3 mm may not have a significant effect on the drive roller grip. Alternatively, sample 7C could be softer since the tempered core is slightly larger, with the same martensite thickness. Softer rebar might be gripped by drive roller teeth more than a harder rebar and thus slip less. The difference in tempered core diameter may not mean that sample 7C is softer though as the external diameter measurements are larger than sample 6C.

The sample which twisted as it was processed, sample 8C, showed relatively circular dimensions with small variations. The largest variation was a 0.5 mm difference between two perpendicular measurements across the tempered core, 9.4 mm and 9.7 mm. Rebar which is oval, instead of circular, in cross section, could twist as certain orientations are deformed more easily. During bending, if the thickness is smaller than the perpendicular thickness, the thinner orientation will bend with less required force. Therefore, the rebar might twist to align the thinnest orientation with the bend plane to bend with least resistance. This twist could cause the out of plane bending that has been seen by customers.

4.6.5 Microhardness Discussion

Microhardness testing across samples showed that all samples were harder in the edge regions and had a softer core. The edge millimetre at the rebar surface had a hardness of approximately 280 HV5 and a softer core, approximately 200 HV5. Pantazopoulos et al.

found similar values in B500C rebar with 14 mm diameter, measured hardness was 310 HV and 190 HV in the edge and core, respectively [21]. This is the desired effect of the quenching process, creating stronger martensite around the edge, while the core self-tempers and is more ductile. Overall, this steel will be both strong and ductile.

The quenching process appears to produce an even layer of martensite around the rebar since large differences in hardness at the edge were not found. For the longitudinal samples, the first and last points ranged between 273 and 290 HV5. The cross sections showed some variation at the edge but only three lines were recorded for each sample, so these are more affected by anomalies.

Variations at the interface between hard and soft regions are likely to be due to starting lines at different distances from the edge and ribs changing the martensite thickness. Some samples appear to vary in thickness of the hard-edge region as hardness reduced at different rates towards the middle for all samples. Quenched region visibly differs in thickness between where ribs are present and where they are not, as seen in the dimensional accuracy measurement. Because of this, the number of indents of a line that fit into the quenched region varied between one and two at either end. So, points two and 12 are averaged from combinations of indents in both quenched and tempered regions. Measuring hardness only in lines that have ribs at either end would ensure indents are in similar locations between all samples. For this, larger samples would have to be made and dimensional variation between samples would still cause some variation in the locations of indents.

4.7 Summary

The grain size was measured using both MLI and ECD techniques in the core. Average grain diameter was found to be 3.89 μm using the MLI technique and 2.6 μm using the ECD technique. In the quenched edge region of the samples, ECD was 2.7 μm and measured mostly martensite lathes. There are only small differences in grain size between samples as the range of ferrite grain size variation is only 0.85 μm and 0.61 μm for the MLI and ECD techniques, respectively. These small differences between samples and cross and longitudinal sections appeared to be random and unlikely to affect rebar properties or processing significantly.

Inclusions were found in the core and edge regions of all samples. These appeared circular in cross section and elongated in the rolling direction in longitudinal sections. EDS analysis showed that these inclusions contained manganese sulphide and the percentage area they cover ranges from 0.22 to 0.37 percent. These inclusions were relatively consistent in all samples and the manganese and sulphur do not exceed the limit in any of the samples. So, the manganese sulphide inclusions are not expected to be detrimental to the rebar or cause any of the samples' unique processing characteristics.

All samples tested showed consistent composition which was within the BS449:2005 limits and close to the composition measured by *Celsa Steel UK* [11]. The main alloying elements are manganese and copper, and all elements are approximately within their specified limits. Variations between samples does not exceed 0.2 wt% for any element so no element can be attributed to the different processing characteristics between the samples.

Texture in samples were quite randomised and showed little orientation preference, except sample 5 which showed a weak rolling texture. The maximum intensity in inverse pole figures for samples 6, 7 and 8 was 1.30. Whereas, in samples 5C and 5L, maximum intensity was 1.83 and 1.73 and both maxima were in the 110 orientation. As steel is rolled, a preference for the 110-type plane of orientation is developed. Rebar is hot rolled so is in the austenite phase during rolling, when grains recrystallise most of the rolling texture is lost and equiaxed grains of ferrite and pearlite form in the core. Since coil five has a weak preference for the 110 plane, it may have been rolled at a lower temperature where not all the grains were above the ferrite to austenite transformation temperature. Coil 5 was processed without issues so this texture may be beneficial to the processing characteristics, however, it is a weak texture and may not have any significant effect.

Small dimensional variations were found in the cross-section samples which could affect the coil behaviour during processing. Sample 7C has a larger height and width than 6C by 0.2 mm and 0.3 mm, respectively. This could affect the twin strand processing as these samples passed through the same drive roller simultaneously. Since the larger bar, sample 7C, was pulled further through the drive roller, larger diameters may slip less than smaller diameters. Sample 5C was the largest sample and had a width of 14.1 mm, 0.7 mm larger than its height. However, this did not affect processing detrimentally. The diameter of sample 8C had an aspect ratio of 0.98. Non-circular dimensions could lead to twisting and out of plane bending as the shortest orientation is deformed with the least required force. The dimensions were only measured at one cross section for each sample, so could vary along the rebar.

From microhardness tests on each sample, it was found that hardness is greatest at the edge, where the steel is affected by quenching, and softer in the core. Hardness was approximately

200 HV5 in the core and 280 HV5 in the region one to two millimetres from the edge. This shows that quenching achieves the intended effect of hardening the edge, while allowing the core to self-temper. Since hardness was relatively consistent in all positions, quenching appears to be uniform, and the processing characteristics are not likely to be affected by hardness.

Location within the coils that the samples were taken from is unknown and only two samples for each coil were tested. The samples were taken where specific processing characteristics occurred but the location within the coil was not recorded. Coils of 12 mm diameter are approximately 2.2 km in length so the properties found in the tested samples cannot represent the entire coils. The microstructure, hardness and dimensions should be measured along sections of the rebar where the sample processing characteristics were seen, and along entire coils, to investigate dimensional variation along the rebar. By testing samples frequently along coils, more reliable characterisation for each of the processing characteristics could indicate influential parameters more reliably.

Chapter 5 FEA Modelling

5.1 Model Objective

The effect of changes in rebar dimensions on the behaviour of the rebar during post processing by customers has been investigated in this study using FEA modelling. Variations in dimensions have been seen between the four samples tested in section 4.4, as well as in technical reports of samples that were returned to *Celsa Steel UK* after inconsistent processing behaviour. These dimensional variations are expected to contribute to changes in processing characteristics since the force required to deform rebar is dependent on the rebar geometry and thickness. However, the effect of these dimensional variations on post processing has not previously been tested. It is not known if the range of dimension observed in samples could be large enough to cause the post processing issues. Therefore, a simplified FEA model of a common processing technique, rebar bending, has been developed in this study to investigate the effect of diameter changes on out of plane deflection.

Dimensional variations have been found both in the samples tested in section 4.4 and samples examined by *Celsa Steel UK* in reports of coils returned by customers. Section 4.4 showed differences in diameter of up to 0.2 mm within a cross section and up to 0.9 mm between the four samples. Thickness of the quenched region at the ribs was also seen to vary by up to 0.3 mm within a sample and 0.5 mm between the samples.

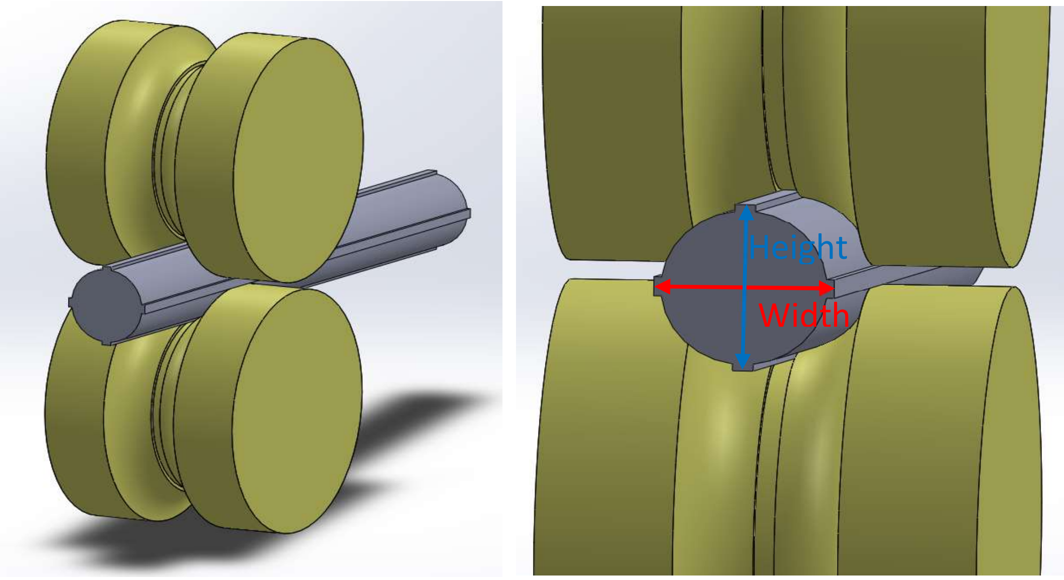

Figure 5.1 Illustration of the location of the height and width dimensions during rolling. These measurements are recorded in technical reports. Both measurements are between two longitudinal ribs and should be approximately 13 mm for 12 mm rebar.

Celsa Steel UK produce technical reports of any sections or whole coils which are returned to them by customers who experienced processing issues. Many of these either describe difficulty straightening the coil or the coil deforming in a plane perpendicular to the intended bending plane. One of the properties *Celsa Steel UK* test on these sections is the dimensions at three points along the section. Dimensions are often found to vary in samples in these reports and are suggested as a cause of the processing issues. Height and width recorded in these reports is measured between two longitudinal ribs, as illustrated in figure 5.1. Height is the distance between ribs that are created by grooves in the rollers, whereas width is between the ribs which were created by the space between rollers. The maximum differences between height and width recorded from each sample in the technical reports for 12 mm rebar is shown in table 5.1 below. The greatest difference between height and width is highlighted and has a height of 13.0 mm and width of only 12.1 mm, a difference of 0.9 mm.

Coil Report	Height (mm)	Width (mm)	Difference (mm)	Aspect Ratio
Thames 2019 07	13.0	12.3	0.7	1.1
	13.0	12.1	0.9	1.1
	12.9	12.3	0.6	1.0
	13.0	12.2	0.7	1.1
Romtech 2019 18	12.9	12.9	-0.1	1.0
	13.0	13.7	-0.6	1.0
Romtech 2019 19	13.0	13.8	-0.8	0.9
	13.0	12.7	0.3	1.0
BRC 2019 23	13.1	13.3	-0.2	1.0
	13.1	13.5	-0.4	1.0
BRC 2019 27	13.1	12.9	0.2	1.0
	13.0	12.8	0.3	1.0
	13.1	12.8	0.3	1.0
	13.0	12.8	0.2	1.0
Craigavon 2019 38	12.7	12.9	-0.2	1.0
	12.9	12.7	0.2	1.0

Table 5.1 Height and width dimensions of 12 mm rebar samples recorded in technical reports of rebar which displayed either out of plane bending or twisting during straightening processes. Each sample was measured in three locations and the location with greatest difference in height and width is shown.

Celsa Steel UK requires 12 mm rebar to have a rib-to-rib diameter around the bar within the limits of 12.7 mm to 13.2 mm, a range of 0.5 mm. Therefore, many of the dimensions found in technical reports in table 5.1 are outside of the limit. Rebar will be modelled without ribs in this study because these are small features which would vastly increase the required computation time. Since rib height on either side is 0.5 mm, the acceptable limits of diameter for the round bar with ribs removed is between 11.7 mm and 12.2 mm.

One hypothesis is that dimensional differences are the cause of some processing irregularities such as out-of-plane bending. Out of plane bending is where a section of rebar is bent in a specific plane, but also deforms perpendicular to this plane, creating a part which is not flat. Dimensional variation between height and width could potentially cause this because if the reinforcing bar is not circular, the thinnest orientation will require the least force to bend. During bending, the rebar might deform most in the thinnest orientation which may not be the intended bending plane. The amount that a change in geometry effects this bending process is not known.

An FEA model has been created using Ansys to characterise the effect of dimensional accuracy on bending deformation. The model simulates an industrial machine bender performing a 90° bend. The geometry of the model was created using Solidworks. Stress distribution and deformation are analysed after the bend is complete to measure the effect of changes in dimensions.

Out of plane deformation was expected to be evident in deformation values at the bar end face in the plane perpendicular to bending. High strain regions may also indicate out of plane bending if they are off centre. The deformation in the Y axis gives the amount of deformation perpendicular to the intended bending plane, which is the XZ plane in this model.

5.2 Model Set Up

5.2.1 Model Geometry

The rebar dimensions in the model are based on the BS4449:2005 specification for 12 mm diameter rebar [11]. This specifies a cylindrical core with a 12 mm diameter and ribs protruding from this. *Celsa Steel UK* have internal control limits which require height and width to be between 12.7 mm and 13.2 mm. To reduce the processing time and number of variables, only the round core of the rebar is modelled, without any ribs. Subtracting rib height, this round bar should have a diameter between 11.8 mm and 12.2 mm.

The mandrel dimensions were based on an automatic link bender (ALB) used at Express Reinforcements in Neath, shown in figure 5.2. This is used to straighten, bend, and cut 12 mm reinforcing bar into various shapes and can process one or two coils at a time. The FEA model replicates this bending process for a single coil of rebar, rather than two.

An automatic link bender has 8 pairs of rollers to straighten the coil and two pairs of drive rollers which the rebar passes through before the bending stage. During bending, the drive rollers keep one end of the rebar fixed. To reduce computation time, a fixed joint was used on the end face of the feed end instead of modelling these rollers.

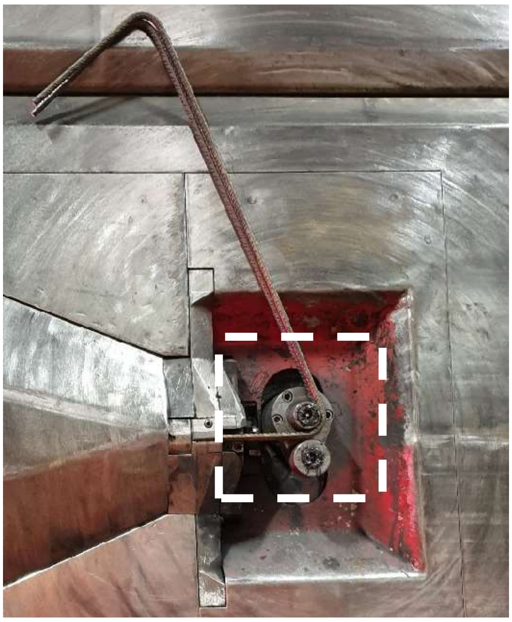

Figure 5.2 An ALB machine at Express Reinforcements UK, bending two sections of reinforcing bar simultaneously. The rebar passes through a covered section of straightening rollers on the left, then between a mandrel and bending pin. The bending pin in this photograph has rotated to bend the rebar upwards and then returned to its starting position.

The geometry of the model is shown in figure 5.3. A section of rebar, 190 mm long, is positioned in an ALB machine with 100 mm protruding passed the mandrel. The rebar is then bent around this mandrel. A linking component connects the mandrel to the bending pin and rotates 90° about the mandrel to cause the bending pin to deform the rebar around the mandrel. The link then rotates back 30° to release the bar and allow any springback.

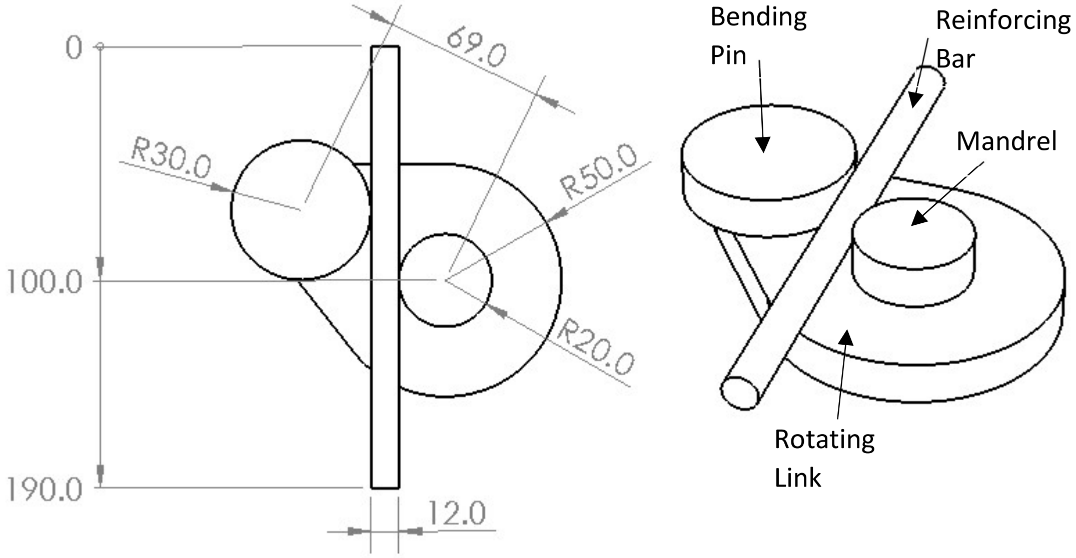

Figure 5.3 Model geometry of ALB machine in the starting position with key dimensions shown, created using Solidworks. The top view (left) and isometric view (right) are shown. A round bar, 190 mm long, is held between a mandrel and bending pin, which are connected by a rotating link.

5.2.2 Material Properties

Characteristic yield tensile strength is specified in BS4449:2005 as 500 MPa and the absolute maximum permissible yield strength is 650 MPa [11]. The reinforcing steel deforms plastically so it is assigned as a nonlinear material. A multilinear isotropic hardening property is assigned so that strength is dependent on strain in the material. The stress and strain properties of reinforcing steel in the model are taken from measurements of quenched and self-tempered reinforcing steel bar recorded by the UK Certification Authority for Reinforcing Steels (CARES) [12]. These stress and strain values are shown in figure 5.4. Yield strength is 550 MPa and UTS is 630 MPa, thus meeting the BS4449:2005 requirements. Young's modulus and Poisson's ratio are not specified in the British Standard so typical room temperature steel values were used to calculate bulk and shear modulus. For reinforcing steel, the young's modulus is 200 GPa and Poisson's ratio is 0.3, giving bulk and shear modulus values of 167 GPa and 76.9 GPa, respectively [3].

For all bending machine parts of the model (mandrel, link, and bending pin), heat treated H13 tool steel was assigned. The yield strength of the H13 tool steel is 1250 MPa and UTS is 1500 MPa [72]. Young's modulus and Poisson's Ratio were 210 GPa and 0.3, respectively which gave bulk and shear modulus values for tool steel of 175 GPa and 80.8 GPa, respectively [3].

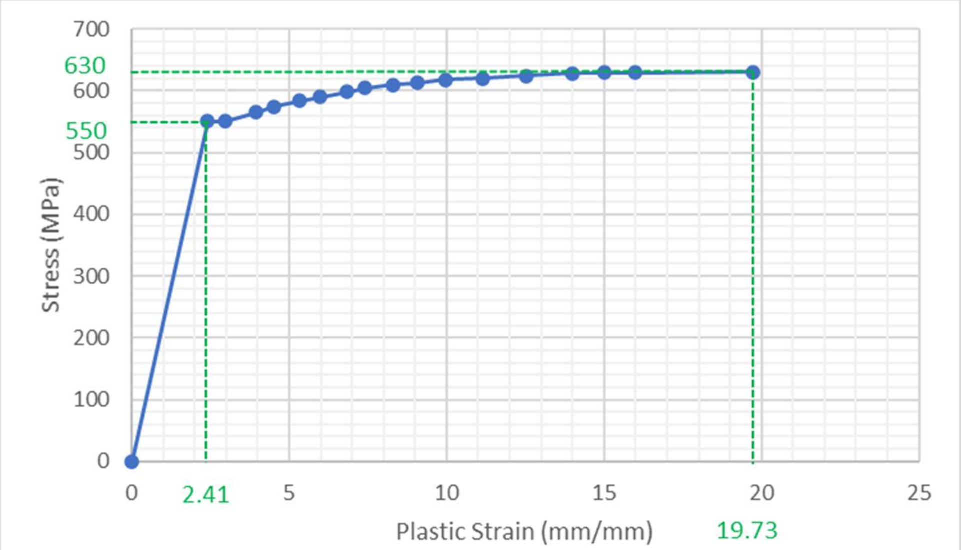

Figure 5.4 Stress-strain graph for quenched and self-tempered reinforcing steel bar measured by UK CARES and used in the FEA bending model (12). Yield strength is 550MPa and UTS is 630 MPa.

5.2.3 Ansys

The 3D model created in Solidworks was imported into Ansys software to undertake FEA of the bending process. A Static Structural analysis system was chosen over a transient structural system since this can determine displacements, stresses, strains, and forces in structures. On the other hand, transient structural analysis involves loads that are a function of time and it is used where the inertia and damping effects are important. Inertia and damping effects are not relevant for this model since the rotational velocity is constant.

5.2.4 Connections and joints

In the model assembly, prior to bending, rebar is tangential to both the mandrel and bending pin and parallel to the link below. The feed end of the rebar is positioned 90 mm from the mandrel so that 100 mm extends past the mandrel, to be bent. The model contains two body-to-ground joints. The first is a fixed joint applied to the face at the feed end of the rebar because, in the automatic link bender, this is held by feed rollers which are fixed during bending. The other body-to-ground joint is fixed about the centre of the mandrel as this is the fixed part that the rebar bends around. Additionally, there are two revolute body-to-body joints. One is between the mandrel and connecting link and the other connects the bending pin to the connecting link, shown in figure 5.5. Both revolute joints have no torsional stiffness or torsional damping because, for this model, the machine parts move by a set displacement, rather than in response to a force. The mandrel joint is rotated to initiate bending while the bending pin joint rotates due to friction, simulating a bush bearing in the actual machine.

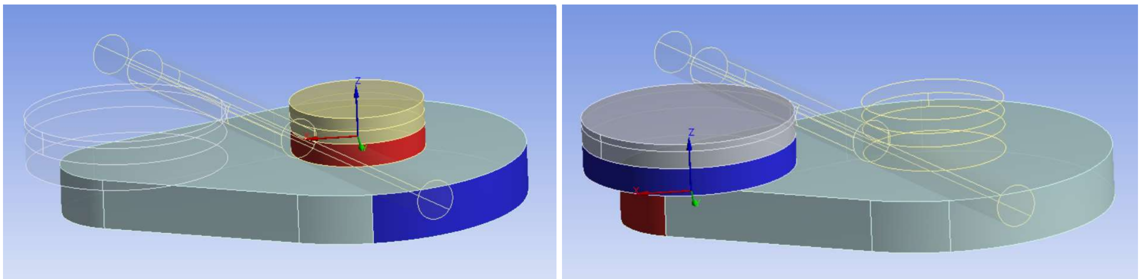

Figure 5.5 Location of revolute joints in the model assembly, the red and blue faces indicate the faces connected by the joint. The mandrel is connected to the connecting link (left), and the connecting link is connected to the bending pin by the second joint (right).

Contacts with no separation are applied between the mandrel and link, and the bending pin and link. These allow for the necessary rotation while keeping all parts in contact. This method reduces computation time compared to modelling the pins used to keep the parts in contact in the actual ALB machine.

Frictional sliding contacts exist in both the inner and outer rebar contact regions. The inner region is between the mandrel and rebar, while the outer region is between the rebar and bending pin. Both frictional contacts are between a body of reinforcing steel and a tool steel body. The coefficient of friction for both contacts is 0.15 since this is a measured value for the contact between two dry steel surfaces [73]. The inner and outer contact regions are shown in figure 5.6, each region is 5 mm in vertical height and extends at least 5 mm over the region that makes contact when the bar is fully bent. At the frictional contact surfaces, an interface treatment adds an offset of 0.01 mm with no ramping to eliminate very small contact areas that can prevent the model converging.

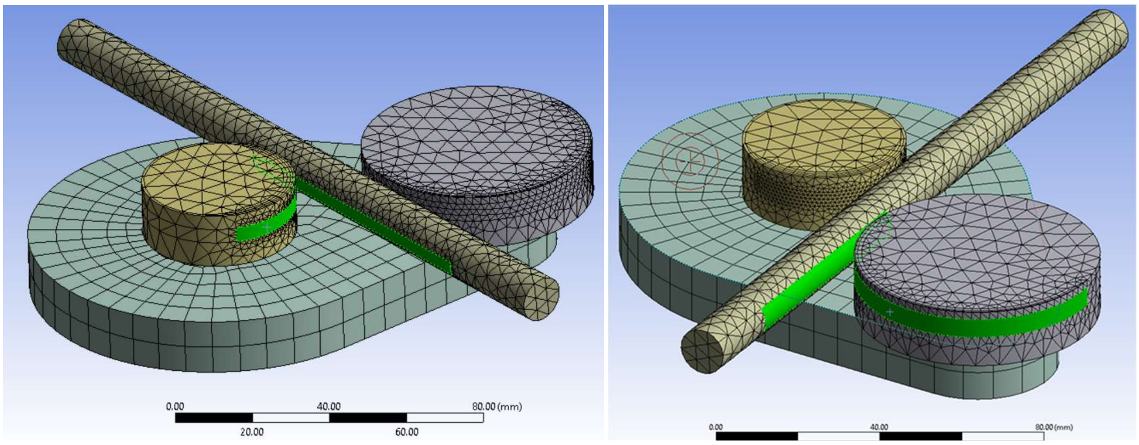

Figure 5.6 Mesh generated for the bending model with inner (left) and outer (right) contact regions highlighted in green. When the bar is bent 90°, all contact made between parts during bending is between these regions.

5.2.5 Meshing

A mesh for the model was created and refined using one case of values for rebar dimensions. Once the mesh was refined to meet the required accuracy, it was applied to all dimension cases tested. The dimensions of the mesh refinement model had diameter A and B values of 11.8 mm and 12.2 mm, respectively. The size of the mesh was gradually reduced until the simulation results converged to a variation below two percent. With variation below two percent, the results are mesh independent and refining the mesh further would increase the required computation time without significantly increasing its accuracy.

A large element size of 7 mm was used for the link component since it experiences very low stress and does not contact the rebar. Both the mandrel and bending pin have 6 mm body element sizes while the rebar body element size is 4 mm. A face element sizing and an inflation were applied to increase the number of elements at each contact region between the mandrel, rebar and bending pin since these are the regions of greatest stress. The contact surface on the mandrel has an inflation with four layers, a growth rate of 1.2, and maximum thickness of 3.0 mm. The Rebar contact region has an inflation with five layers, a 1.4 growth rate, and 2.5 mm maximum thickness, because this is the part being studied. Inflation at the bending pin region has three layers, 1.8 growth rate and 1.8 mm maximum thickness as the outer contact was seen to experience less stress than the inner contact in preliminary tests. These inflation settings were determined by the geometry of each region.

Preliminary tests showed greatest stress at the areas where the rebar contacted the mandrel and bending pin. Therefore, these areas have most impact on deformation and were refined to ensure results that were independent of the mesh. The inner side of the bend had greater stress than on the outer side of the bend in initial tests. So, the contact faces between the inner side of the rebar and mandrel require finer mesh elements than the contact regions of the rebar and bending pin, because the region of greater stress will have greater impact on deformation results.

Table 5.2 shows the results from each mesh iteration tested in the mesh refinement. The variation of each result from the average of all results in the mesh element convergence is calculated. Y axis deformation is the most important variable to refine since this represents the out of plane deformation that is investigated in this modelled. Initially, the inner face was varied, and the Y axis deformation results were found to converge within two percent at an element size of 1.1 mm. The outer face was then tested and found to converge at a 2.1 mm element size. Therefore, the final converged mesh element sizes are 1.1 mm and 2.1 mm for the inner and outer contact surfaces, respectively. By applying this method of mesh refinement, the model mesh has been validated to within two percent. This final mesh is shown in figure 5.7.

Mesh Element Size (mm)		Y-Axis Deformation (mm)		Stress (Mpa)		Plastic Strain mm/mm	
Inner	Outer	Maximum	Variation (%)	Maximum	Variation (%)	Maximum	Variation (%)
1.0	2.2	0.69	1.80	547.7	1.22	0.30	4.6
1.1	2.2	0.67	-0.05	542.2	0.21	0.29	0.4
1.2	2.2	0.71	6.01	545.9	0.88	0.28	-1.1
1.3	2.2	0.62	-8.30	536.6	-0.82	0.28	-3.1
1.4	2.2	0.68	0.55	533.0	-1.49	0.28	-0.9
1.5	2.2	Failed	Failed	Failed	Failed	Failed	Failed
1.1	**2.0**	0.70	-1.71	537.7	-0.46	0.29	1.1
1.1	**2.1**	0.72	1.80	540.7	0.10	0.30	1.6
1.1	**2.2**	0.67	-5.26	542.2	0.38	0.29	-1.0
1.1	**2.3**	0.78	9.63	540.1	-0.02	0.29	-1.6

Table 5.2 Results of mesh refinement of the bending model. Mesh element size for the rebar contact regions at the inner and outer sides of the bend were varied, starting with the inner contact, to ensure the model results converged within two percent. The converged mesh has element sizes 1.1 mm and 2.1 mm.

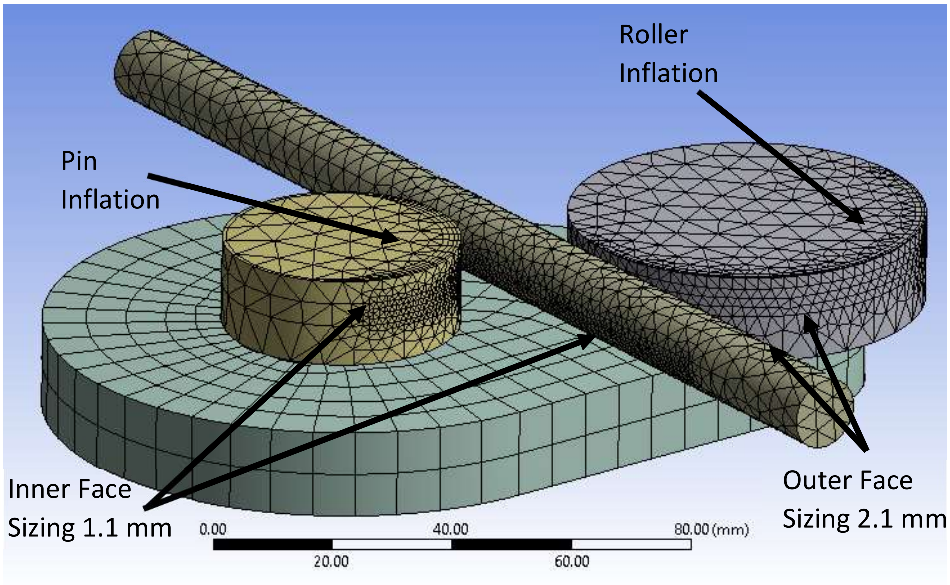

Figure 5.7 Final mesh parameters for the bending model. Mesh element size is 1.1 mm and 2.1 mm for the inner and outer face contact regions, respectively. Inflation regions are visible at the top faces by multiple layers closer together.

5.2.6 Solver Techniques

The revolute body-to-body joint between the mandrel and link is assigned a ramped rotation of 90° over one second. This means the displacement increases linearly until it reaches 90° at the end of the time step. Since the mandrel contains a fixed joint, this stays stationary while the link moves during the rotation. A second time step is used to rotate the machine parts back by 20° over 0.5 seconds. This allows the bent rebar to be viewed after the bending forces have been removed and any spring back and subsequent twist have occurred. During the first timestep, the number of analysis subsets is between 1 to 100 to allow the model to converge.

Large deflection is applied since the bar experiences large plastic deformation and non-linear properties are significant to the model. This allows rebar stiffness to change as the rebar deforms. Figure 5.4 shows that as the reinforcing steel deforms, the stress required to deform it further increases until it reaches the UTS.

The properties measured from the results of this model are deformation, stress, and plastic strain. Deformation is measured in the X, Y, and Z planes individually. Since the machine's rotary motion is in the X-Z plane, any deformation of the rebar in the Y plane is considered out-of-plane deformation. This is the key result that will be compared for the different rebar dimensions tested. In addition, the stress and maximum strain will be measured for the rebar. Any stress and strain that is not symmetrical through the bar may also indicate out of plane bending effect.

5.2.7 Variables

The independent variables in this test are the dimensions of the rebar cross section. These are diameters A and B, as shown in figure 5.8. Diagonals A and B refer to two perpendicular distances across the rebar, which are each 45 degrees to the bending plane, which is the XZ plane in figure 5.8. These diameters are the independent variables and have been varied by decreasing the value of diameter A and increasing the value of diameter B, so that the aspect ratio of the rebar deviates further from one. The diameter values that were tested are shown in table 5.3. The limits for the diameter, excluding ribs, are 11.7 mm and 12.2 mm, so dimensions both within and outside of this range were tested. From the technical reports, the largest difference seen between diameters within a cross section is 0.9 mm. Therefore, dimensions were tested in increments of 0.2 mm from a circular rebar up to a 0.8 mm difference.

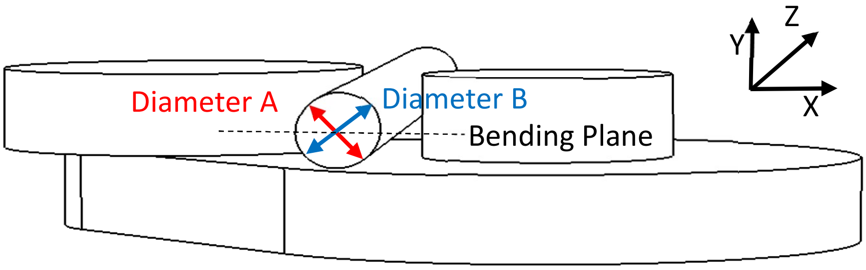

Figure 5.8 Location of independent variables, diameter A and diameter B, which are tested at different values. The diameters are perpendicular from each other and both 45° from the bending plane, the XY plane, represented by a dotted line.

	Dimensions (mm)	
	Diameter A	Diameter B
Within Tolerance	12.0	12.0
	11.9	12.1
	11.8	12.2
Outside Tolerance	11.7	12.3
	11.6	12.4

Table 5.3 Planned values of the independent variables, diameters A and B, for testing their effect on out of plane deformation during bending. Diameters A and B are the thickness across the rebar in two perpendicular orientations, both 45° from the bending plane.

It is expected that rebar with different values for diameters A and B, both 45° from the bending plane, will cause out of plane deformation. Increasing the difference between A and B is expected to lead to greater out of-plane deformation. Since the effect of these dimensions on bending have not previously been tested, it is unknown whether the out of plane deformation caused will be sufficient to make a finished part out of tolerance.

5.3 Results

Stress, strain, and displacement were measured for each dimension case and results are shown for the rebar with diameters A and B that had 0.0 mm, 0.4 mm and 0.8 mm difference. Red areas indicate high values while dark blue indicates the minimum values of either strain or deformation. The ALB machine parts did not experience large stress or deformation because the parts are large and made of tool steel, which has greater strength than reinforcing steel. Figure 5.9 shows the whole model assembly, for round rebar at three timesteps, after 0.5 seconds and 45° rotation, after 1.0 seconds and 90° rotation, and after 1.5 seconds when rotation is 70° from the original position. Stress is larger during bending than after bending and a very small amount of springback appears to occur. Springback after the bar is released is 1.3mm, 0.0 mm, and 1.8 mm in the X, Y, and Z directions, respectively.

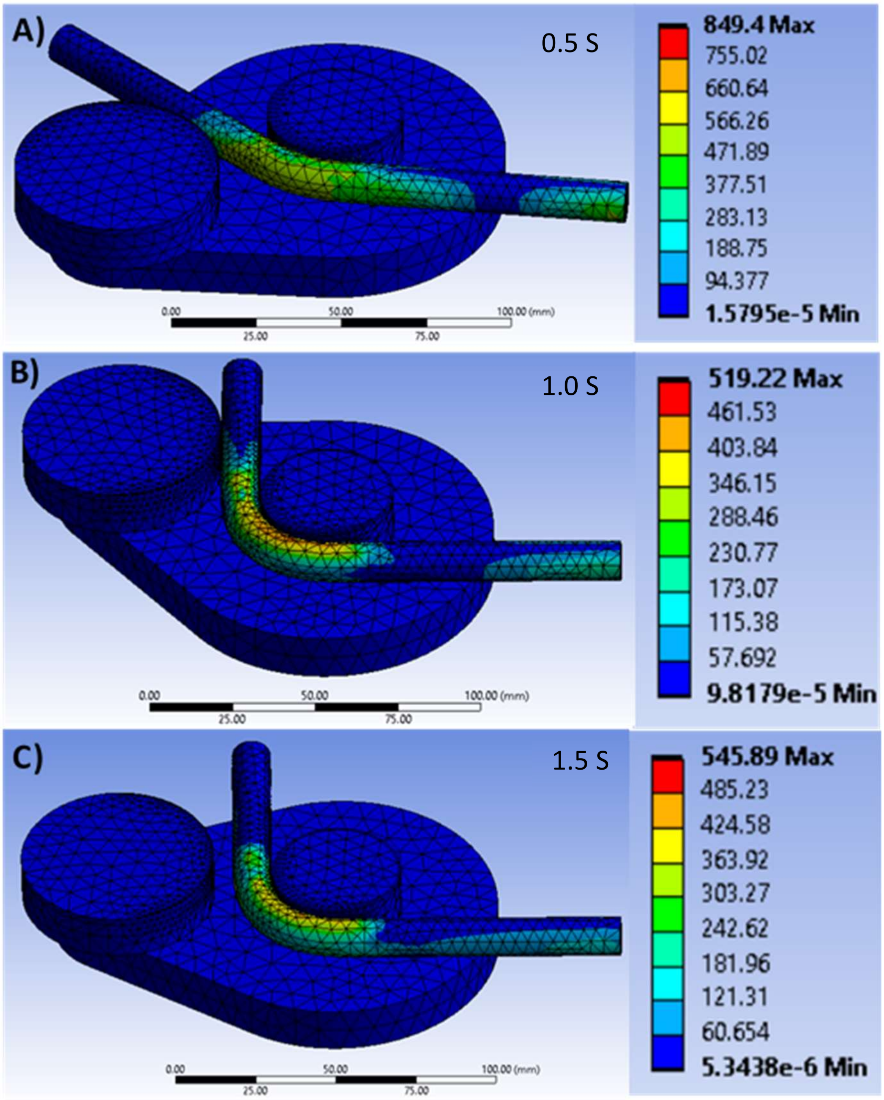

Figure 5.9 Equivalent stress in the whole model, with both dimensions A and B equal to 12 mm, at three timesteps during the bend process A) after 0.5 seconds and 45° rotation, B) after one second and 90° rotation, and C) after 1.5 seconds and 20° reverse rotation.

Results of the case where diameters A and B are both 12.0 mm, so the bar is cylindrical, are presented in figure 5.10. Figure 5.10 shows Y-axis directional deformation and plastic strain images for this rebar at 1.5 seconds, after bending and subsequent release from the bending machine. The Y-axis is positive in the downward direction in the deformation result figures, so negative Y values indicate upward deformation, away from the bending machine. Figure 5.10 shows Y-axis (out of plane) deformation of between -0.42 mm and 0.40 mm. The regions of maximum and minimum deformation are located around the bend. As this section of the bar is squeezed between the mandrel and bending pin, it deforms to a less round shape with flat areas against the mandrel and bending pin. The bent end face, approximately 100 mm from the bend, shows 0.044 mm Y-axis deformation. This is a very small amount of out of plane deformation. In a larger part with multiple bends, this is unlikely to lead to enough out of plane deformation to make the part unusable. The maximum equivalent plastic strain was 0.278 and occurred at the inner radius of the bend. The strain field is relatively uniform, there is little difference between the top and bottom halves, which is expected for a circular bar.

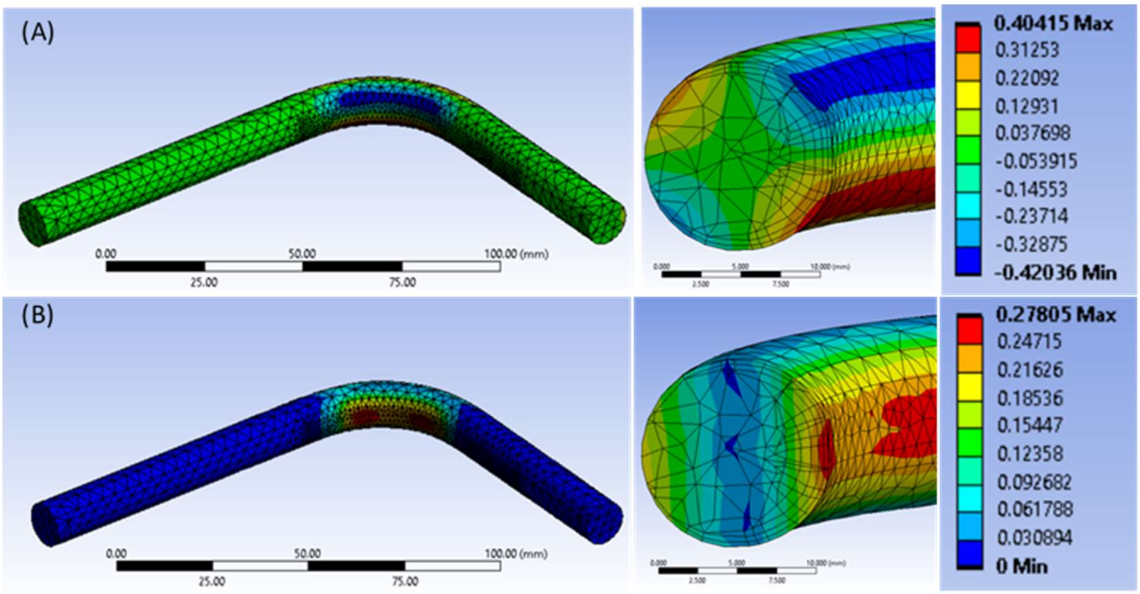

Figure 5.10 Results of bending a bar with 12.0 mm length in both diameters A and B, including a cross section through the centre of the bend and a colour contour range. The results shown are for (A) Y-axis deformation, and (B) plastic strain in the rebar.

Figure 5.11 shows the results of the tolerance limit case at 1.5 seconds, where dimension A and B are 11.8 mm and 12.2 mm, respectively. The Y-axis deformation around the bend is approximately 0.4 mm, like the previous round bar case. However, the greatest Y-axis deformation occurred at the bent end, which reached 0.72 mm. This out-of-plane deformation increases from the bend towards the end face which suggests a twist in the bend region initiates this out of plane trajectory. The greatest plastic strain is 0.296, located at the inside of the bend. The cross section through the centre of the bend appears approximately equally strained between the top and bottom halves which does not suggest any large unequal strain caused by the difference in dimensions.

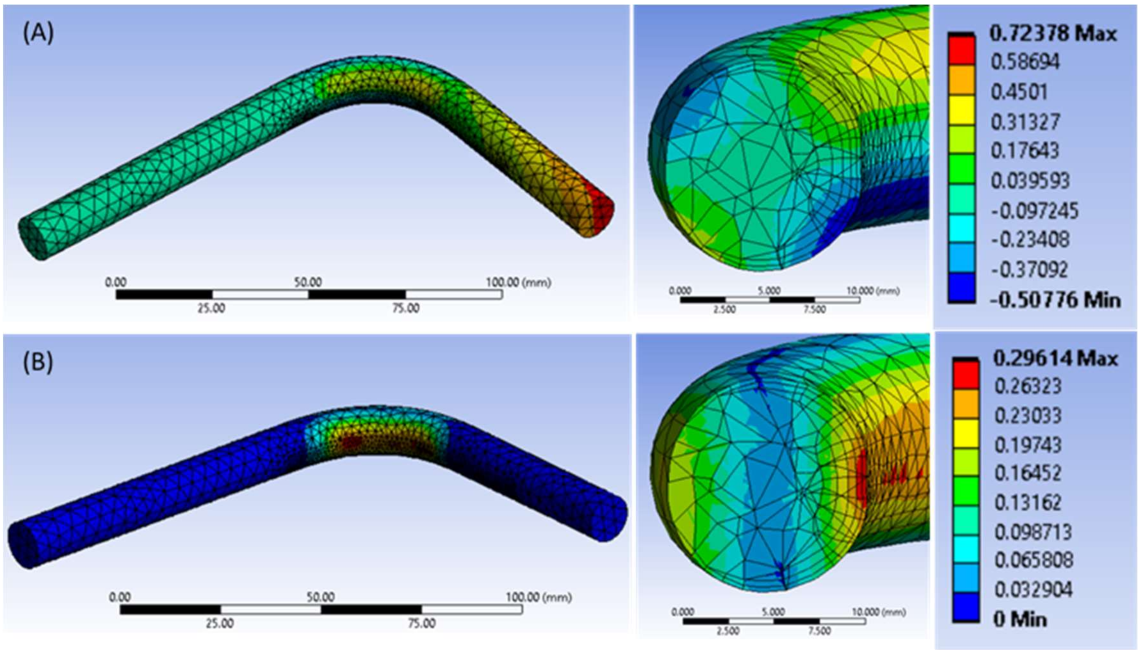

Figure 5.11 Results of bending a bar with 11.8 mm and 12.2 mm length in diameters A and B, respectively, including a cross section through the centre of the bend and a colour contour range. The results shown are (A) Y-axis deformation, and (B) plastic strain in the rebar.

Results of the rebar case in which diameters are close to the greatest variation in diameter found in technical reports are shown in figure 5.12. In this case, diameters A and B are 11.6 mm and 12.4 mm, respectively. The out of plane deformation is greatest at the bent end, where it reaches 1.46 mm. This is a downward deformation, the side of the rebar in which the thinnest diameter (diameter A) is closest to the mandrel and the thicker diameter is on the outside of the bend. The maximum strain is 0.289, which is close to the previous dimension cases. The strain cross section shows greater strain at the bottom than the top and the face that is flattened against the mandrel deforms more at the top than the bottom.

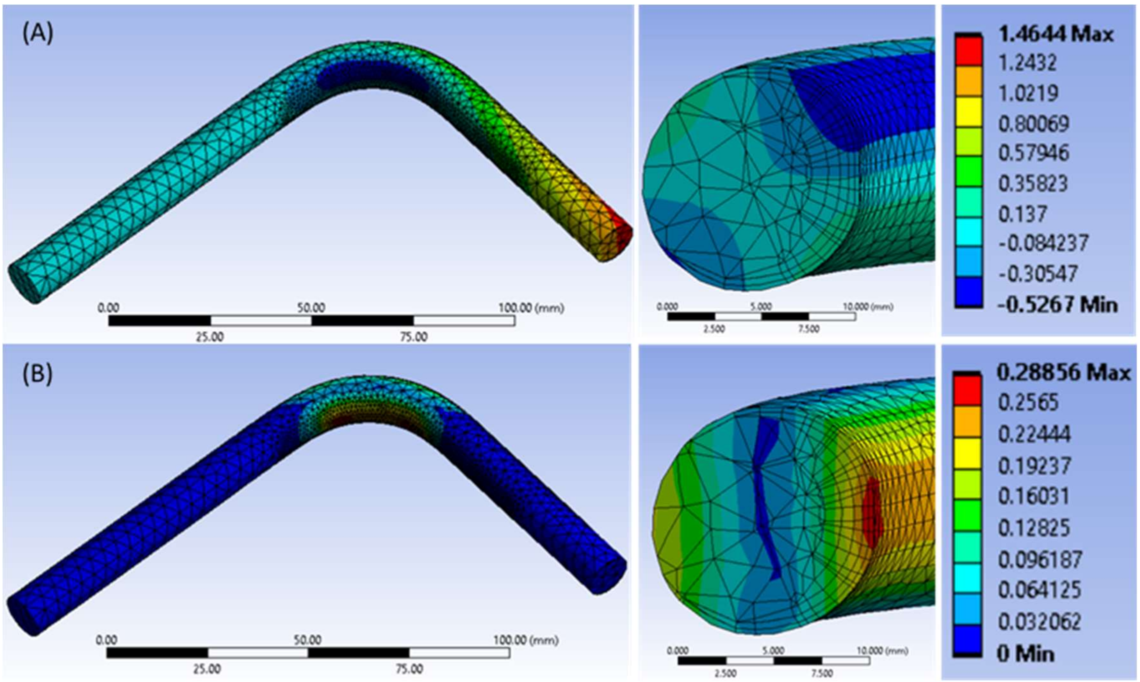

Figure 5.12 Results of bending a bar with 11.6 mm and 12.4 mm length in diameters A and B, respectively, including a cross section through the centre of the bend and a colour contour range. The results shown are (A) Y-axis deformation, and (B) plastic strain in the rebar.

The results of all dimension cases tested using the FEA bending model are shown in table 5.4. Diameter A was incrementally reduced by 0.1 mm while diameter B was increased by 0.1 mm, gradually increasing the ovality of the rebar. Maximum Y deformation at the bent end was seen to increase from 0.04 mm to 1.46 mm as the difference between diameters A and B increase. The out of plane angle was calculated from the out of plane deformation 100 mm from the bend, using trigonemetry, and increases from 0.0004° to 0.0146°. Using this angle, the out of plane deformation that would be produced for a 500- by 500- mm square shape with four bends is predicted. The calculation assumes the same out of plane angle is created at each of the four bends, compounding the effect. This produces large cumulative out of plane deformation, up to 73 mm, which is likely to be unacceptable for processors. No clear correlation between either maximum stress or maximum plastic strain and the difference between diameters can be deduced from table 5.4. All maximum stress values are between 540 and 546 MPa and strain varies between 0.28 and 0.30.

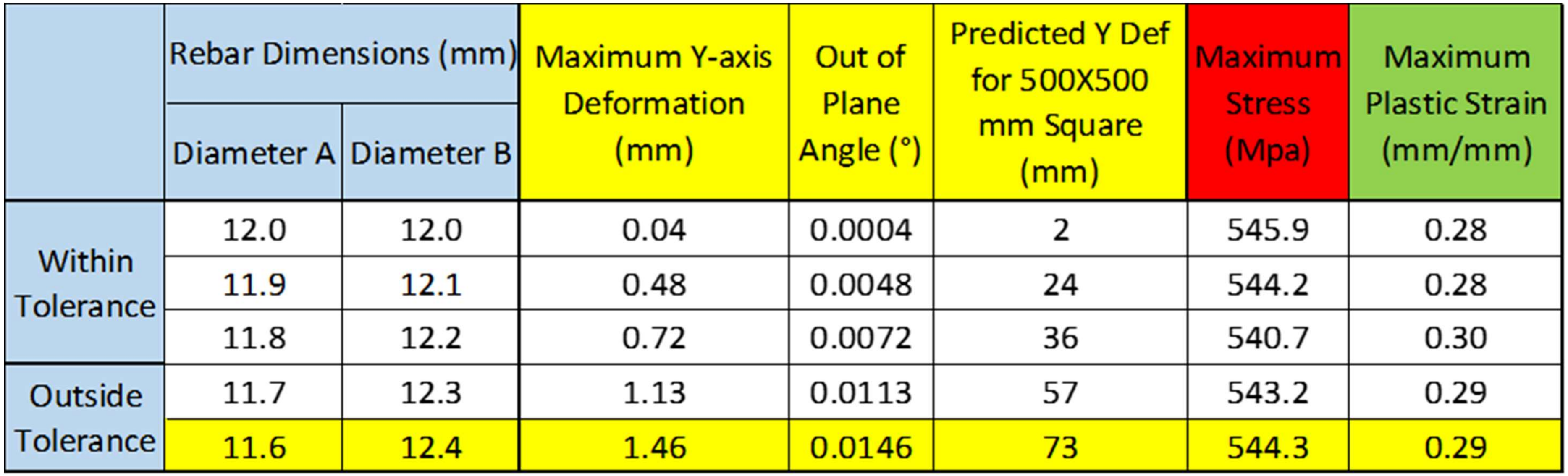

	Rebar Dimensions (mm)		Maximum Y-axis Deformation (mm)	Out of Plane Angle (°)	Predicted Y Def for 500X500 mm Square (mm)	Maximum Stress (Mpa)	Maximum Plastic Strain (mm/mm)
	Diameter A	Diameter B					
Within Tolerance	12.0	12.0	0.04	0.0004	2	545.9	0.28
	11.9	12.1	0.48	0.0048	24	544.2	0.28
	11.8	12.2	0.72	0.0072	36	540.7	0.30
Outside Tolerance	11.7	12.3	1.13	0.0113	57	543.2	0.29
	11.6	12.4	1.46	0.0146	73	544.3	0.29

Table 5.4 Comparison of results from all rebar dimensions tested with the FEA bending model, both within and outside the tolerance limits. Maximum Y-axis deformation is at the end face, 100 mm from the bend. Predicted Y-deformation is the predicted out of plane deformation for a typical 500 x 500 mm square with 4 bends, calculated from the out of plane angle.

5.4 Discussion

The results of the model show that as the bar becomes increasingly oval, it deforms increasingly out of plane when bent. Increasing the difference between diameters A and B from zero mm to 0.8 mm caused the out of plane deformation, 100 mm after the bend, to increase from 0.04 mm to 1.46 mm. This is calculated to increase the out of plane deformation in a 500 mm square with four bends from 2 mm to 73 mm. The out of plane deformation is in the downward direction, towards the half of the bar in which the thinnest orientation (diameter A) faces the mandrel.

Non-circular dimensions do not show any effect on the maximum strain or stress experienced during bending. This may be because the average diameter of all the dimension cases is 12.0 mm since diameter A was always reduced by the same amount that diameter B was increased. Testing the model with dimensions that give a different average thickness, for example where diameter A is 12.0 mm and diameter B is 12.4 mm, is expected to change the maximum amount of stress and strain.

Based on the Y-axis deformation results, non-circular dimensions are shown to cause out of plane bending in this FEA model. The angle at which the bar was out of plane increased by 0.0036° on average for an increase of 0.2 mm in the difference between diameters A and B. The out of plane deformation would lead to out of tolerance shapes which are unusable in concrete structures or require further processing to be flattened. Even rebar which is within the dimensional tolerance displayed an out of plane bending angle of 0.0072°. This could create out of tolerance parts if the desired shape has a large geometry and multiple bends.

Improving dimensional accuracy could improve the consistency of rebar processing with ALB machines by reducing out of plane bending. Dimensional accuracy has been shown in this model to have a detrimental effect on bending of a round steel bar as it can cause out of plane bending, a key processing issue. Improving accuracy of rebar dimensions is likely to improve the reliability of rebar processing behaviour. This would reduce the need for machine adjustment and scrap during processing, increasing production rates and profitability. Dimensional accuracy of steel bar is most affected by the rolling stage, so further research to improve this stage of manufacture is likely to be most beneficial.

Results of the FEA model may not reflect results of rebar in an actual ALB machine. The modelled rebar does not include ribs; only the smooth core is modelled. The effect of these ribs on bending strain and deformation is not known. Also, various properties such as coefficient of friction and the tool steel properties will be different in an industrial bending machine. The standard coefficient of friction value between two dry steel surfaces was used in the model. To increase the model accuracy, experimental values should be found for such properties.

The model indicates that dimensional variations do affect out of plane bending behaviour and may be significant enough to cause processing issues. This model should be validated by experimental tests of bending rebar with specific dimensions. The similarity between out of plane deformation in these tests can be compared to the model to evaluate the accuracy and confidence of results. In addition, potential manufacturing improvements to increase dimensional accuracy could be investigated. Since rolling has the most influence on rebar geometry, development of the rolling process may be beneficial to reduce out of plane bending as well as other processing inconsistencies.

5.5 Summary

The FEA bending model shows that variation in cross sectional dimensions can cause out of plane deformation during bending. When the diameter is longer in one orientation than its perpendicular diameter, each are 45° to the bending plane, out of plane deformation occurs. For a difference between diameters of 0.8 mm, out of plane deformation 100 mm from the bend reaches 1.46 mm (table 5.4). This shows that dimensions are influential in causing the out of plane bending processing inconsistency. Improving the consistency of cross-sectional dimensions may reduce the frequency with which adjustments are required during processing. Thus, increasing production rate and reducing waste.

Chapter 6 Conclusions

6.1 Conclusions

Data analysis, microstructural investigations and modelling were conducted on steel rebar produced in an EAF by *Celsa Steel UK* to determine key parameters causing deficiencies which lead to rejection from customers. Tensile strength along coils has been analysed to draw conclusions on the variations between coils and within individual coils. Materials properties such as grain size, orientation, hardness, and composition, were tested for cross sections and longitudinal samples that each displayed different processing characteristics. An FEA model was created of the bending process that creates shapes from finished rebar coils and dimensional variations were tested to measure the effect on out of plane deflection. The following conclusions can be drawn:

Significant variations in tensile strength were found within a 2.2km coil of 12 mm rebar produced by an EAF. A variation in yield strength between 502 MPa and 597 MPa within a coil has been found through coil cut up reports. With a target yield strength of 500 MPa, this is a variation of 19% compared to the ideal tensile strength. Coils were shown to have greater tensile strength at external turns of the coil compared to the inner turns. It is suggested that differences in coil cooling rates throughout the coil cause the variation in tensile strength [62].

Two different post processing inconsistencies were compared with a nominal sample. Firstly, it when twin coils were fed simultaneously through a two-bar bending machine, dissimilar deformation resulted in one coil being pulled through the drive roller further than the other. Secondly, out of plane bending occurred when coils were run through a bending machine. In both cases, microstructural investigation showed no significant variation in average grain size, orientation, hardness, and composition when compared to a nominal sample. Small differences in dimensions were found between samples and around the circumference of each sample.

Cross sectional dimensions were identified as a key factor effecting rebar mechanical properties. Ansys modelling of 12mm rebar with the maximum tolerated aspect ratio, 1.03, and the thickest plane orientated 45° to the bending plane, showed out of plane deflection after a bend of 90°. The out of plane deflection reached 0.72 mm at the end face, 100 mm from the bend. Aspect ratio was increased further, up to 1.07, as these dimensions have been seen in *Celsa Steel UK* technical reports. The out of plane deformation in this case, where diameter varied by 0.8 mm, was 1.46 mm, 100 mm from the bend. This effect could be magnified when several bends are performed to create complex rebar shapes.

6.2 Future Work and suggestions

The mechanisms of cooling in a rebar coil are not fully understood. Models of temperature evolution and the effect of grain growth and precipitation on mechanical properties have been previously created and verified for coils of flat steel products with various compositions [62–64]. Similar models have not been developed for round bars and rebar, where multiple rows make up each layer of the coil. This model could provide valuable information on how rebar coils can be cooled uniformly. The model can be verified by comparing it to footage from a thermal imaging camera of a rebar coil as it cools.

This study has analysed and compared the microstructure and materials properties in samples from coils that displayed various processing characteristics, but the development of the microstructure along an entire coil has not been investigated. Since reports of tensile tests along coils have been used to show clear changes within coils in this study, differential coil cooling has been proposed to cause this. Further work is suggested in understanding the variation in mechanical properties in the coil. For example, taking samples at set distances along a coil for SEM analysis would provide further evidence of whether the tensile variation is due to cooling differences across the coil causing microstructural variations. To increase the understanding of microstructure in rebar with the processing characteristics tested in this study, the microstructure of more samples displaying these characteristics should be studied and compared. These samples must be taken from the exact point the characteristic occurs.

The dimensional variations found in rebar have been shown to cause out of plane deflection during bending of a round bar without ribs. The exact amount of out of plane deflection may be different in practise, but the model proves that out of plane bending is affected by dimensional accuracy. To verify the accuracy of the model, experimental validation is required. This could involve measuring the dimensions of rebar samples and their out of plane deflection after bending. Also, key parameters, such as rebar-to-machine friction coefficient and the bending machine's material properties should be measured to refine the model. Furthermore, the influence of including ribs in the model could be tested and, if necessary, rebar ribs could be included in the model geometry.

Further properties can be tested using the FEA model of a bending process to test their effect on bending. For example, the differences in strength seen along a coil and between different coils from Celsa's coil cut up reports in chapter three. Different tensile strength properties could be applied to the model and the ending forces and deformation would be recorded.

6.3 Industrial Implications

Data collected in the study can be used by the steel making company, *Celsa Steel UK*, to advise its customers on how to use this material when processing. The data collected on mechanical properties, hardness through the thickness, microstructure, and dimensional accuracy and its effect on bending can be used to suggest the causes and solutions for some inconsistent behaviours that processors experience. In particular, if out of plane deformation is seen during bending, the dimensions around the rebar should be checked.

Significant changes in tensile strength were shown along coils which are likely to cause processing and tolerance issues. The temperature evolution of coils as they cool should be investigated to understand whether cooling patterns emulate the tensile strength patterns found in this study. Depending on the results of cooling measurements, methods of achieving uniform coil cooling may then be investigated. These include stacking coils during cooling, the use of a thermostat or insulating sleeve, optimising coiling and finishing temperatures, and a variable quenchant flow rate. Comparing manufacturing process parameters of coils that process well and coils which have processing issues could indicate influential parameters that should be controlled.

The microstructure of reinforcing steel for use in concrete structures produced by *Celsa Steel UK* has been characterised. Grain size, inclusions and texture are now understood through SEM imaging. Composition defined in the EAF process was found to accurately match the composition measured using EDS. The processing characteristics tested, which were out of plane bending and differences between coils pulled through a drive roller together, showed no significant differences in microstructure compared to a control sample. However more samples from different coils displaying each of these characteristics should be tested to increase reliability.

Dimensions across the cross section of rebar in *Celsa Steel UK* technical reports were found to vary and exceed the tolerance limits. These variations in cross section dimensions have been shown to cause out of plane bending in an FEA bending model. The tolerance limits showed enough of out of plane deflection to cause certain large shape structures that are commonly produced to be defective. The effects of deflection are particularly significant for shapes with large dimensions and multiple bends, which compound the deflection. Therefore, the acceptable dimensional tolerance may need to be reduced to create rebar that can be processed accurately.

Additionally, the dimensional accuracy of rebar produced should be increased. Inaccuracy of cross-sectional dimensions is expected to be caused by limitations in the rolling process. Therefore, investigation into the current rolling practises is recommended to identify areas requiring improvement to increase geometrical accuracy. This could involve more accurate rolling guides, more rolling stages, adjusting rolling speed, or a feedback loop to adjust rolling guides as the steel is being rolled. *Celsa Steel UK* have recently invested in new dimensional gauges to monitor rebar geometry during rolling to better control dimensional accuracy.

Chapter 7 References

[1] WorldSteel Association. World Steel in Figures 2019. 2019.

[2] Wente EF, Wondris EF, Nutting J. Steel. Encyclopedia Brittanica 2019.

[3] Callister WD, Rethwisch DG. Materials Science and Engineering 9th Edition. 2014. https://doi.org/10.1016/j.str.2011.03.005.

[4] Dossett JL, Boyer HE. Practical Heat Treating. 2006.

[5] Cottrell A. An Introduction to Metallurgy. 2nd ed. The Institute of Materials; 1995.

[6] Olson GB, Feinberg ZD. Kinetics of Martensite Transformations in Steels. Phase Transformations in Steels 2012;2:59–82. https://doi.org/10.1533/9780857096111.1.59.

[7] Porter DA, Easterling KE, Sherif MY. Phase Transformations in Metals and Alloys. 3rd ed. CRC Press; 2009.

[8] Brog JP, Chanez CL, Crochet A, Fromm KM. Polymorphism, What it is and How to Identify it: A Systematic Review. RSC Advances 2013;3:16905–31. https://doi.org/10.1039/c3ra41559g.

[9] Bhadeshia H, Honeycombe R. Formation of Martensite. 4th ed. Elsevier Ltd; 2017. https://doi.org/10.1016/b978-0-08-100270-4.00005-6.

[10] Concrete Reinforcing Steel Institute. Reinforcing Steel 2019.

[11] British Standards Institution. BS4449:2005: Steel for the Reinforcement of Concrete - Weldable Reinforcing Steel - Bar, Coil and Decoiled Product - Specification. 2005.

[12] Annexes N. The CARES Guide to Reinforcing Steels Properties of Tensile Test on Reinforcing Bar. UK CARES; n.d.

[13] Maffei B, Salvatore W, Valentini R. Dual-phase Steel Rebars for High-ductile R.C. Structures, Part 1: Microstructural and Mechanical Characterization of Steel Rebars. Engineering Structures 2007;29:3325–32. https://doi.org/10.1016/j.engstruct.2007.09.002.

[14] Caprili S, Salvatore W, Valentini R, Ascanio C, Luvarà G. A New Generation of High-ductile Dual-Phase Steel Reinforcing Bars. Construction and Building Materials 2018;179:66–79. https://doi.org/10.1016/j.conbuildmat.2018.05.181.

[15] Nair SAO, Pillai RG. Microstructural and Corrosion Characteristics of Quenched and Self-Tempered (QST) Steel Reinforcing Bars. Construction and Building Materials 2020;231:117109. https://doi.org/10.1016/j.conbuildmat.2019.117109.

[16] Thomas G. The Physical Metallurgy and Alloy Design of Dual Phase Steels 1983.

[17] Stewart JL, Jiang H, Krause S, Chawla N. Influence of Thermal Aging on the Microstructure and Mechanical Behavior of Dual-phase, Precipitation-Hardened, Powder Metallurgy Stainless Steels. Metallurgical and Materials Transactions A: Physical Metallurgy and Materials Science 2012;43:124–35. https://doi.org/10.1007/s11661-011-0844-3.

[18] Iacoviello F, di Bartolomeo O, di Cocco V, Piacente V. Damaging Micromechanisms in Ferritic-Pearlitic Ductile Cast Irons. Materials Science and Engineering A 2007;478:181–6. https://doi.org/10.1016/j.msea.2007.05.110.

[19] Kabir MS, Islam MM, Bepari MMA. Impact Toughness of Concrete Reinforcement Bars Produced by the THERMEX Process and Ordinary Rolling Process. Ijitee 2014;4:53–9.

[20] Celsa Group. Celsamax 2008.

[21] Pantazopoulos G, Pressas I, Vazdirvanidis A. Fatigue Failure Analysis of a Ø14 B500C Steel Rebar: Metallurgical Evaluation and Numerical Simulation. Engineering Failure Analysis 2019;101:180–92. https://doi.org/10.1016/j.engfailanal.2019.03.016.

[22] Mouritz A. Strengthening of Metal Alloys. Introduction to Aerospace Materials, Woodhead Publishing in Materials; 2012, p. 57–90. https://doi.org/10.1533/9780857095152.57.

[23] Morito S, Huang X, Furuhara T, Maki T, Hansen N. The Morphology and Crystallography of Lath Martensite in Alloy Steels. Acta Materialia 2006;54:5323–31. https://doi.org/10.1016/j.actamat.2006.07.009.

[24] Morito S, Saito H, Maki T, Furuhara T. Effect of PAGS on Crystallography and Morphology of Lath Martensite in Low Carbon Steels. ISIJ International 2004;45:91–4.

[25] Canale LCF, Vatavuk J, Totten GE. Introduction to Steel Heat Treatment. vol. 12. Elsevier; 2014. https://doi.org/10.1016/B978-0-08-096532-1.01202-4.

[26] Krauss G. Quench and Tempered Martensitic Steels: Microstructures and Performance. vol. 12. Elsevier; 2014. https://doi.org/10.1016/B978-0-08-096532-1.01212-7.

[27] Randle V. Macrotexture and Microtexture Techniques. Encyclopedia of Materials: Science and Technology 2000.

[28] Sharma K. Introduction to IC Technology. 2016.

[29] Vlad CM, Bunge HJ. Proceedings on Sixth International Conference on Textures of Materials 1981:649.

[30] Silva CE, Vasconcellos AL. The Effects of Non-metallic Inclusions on Properties Relevant to the Performance of Steel in Structural and Mechanical Applications. Journal of Materials Research and Technology 2019;8:2408–22. https://doi.org/10.1016/j.jmrt.2019.01.009.

[31] Li Z ming, Li X, Yang L, Shen Z yan, Wang B lei, Zhao S li, et al. Effect of Coiling and Annealing Temperatures on Yield Point Behavior of Low-carbon Steel. Journal of Iron and Steel Research International 2020;27:325–33. https://doi.org/10.1007/s42243-019-00342-7.

[32] Millman DS. Quality Steel from the EAF. Steel Times 2000. https://doi.org/10.1016/j.jaci.2012.05.050.

[33] Ciocan A, Potecasu F. Scrap Quality and Metallurgical Effects Associated with Copper and Tin As Tramp Elements in the Casting Steels 2010:22–7.

[34] Łabaj J, Oleksiak B, Siwiec G. Study of Copper Removal From Liquid Iron. Metalurgija 2011;50:265–8.

[35] Kostetsky Y, Troyansky A, Samborsky M. Removal of Copper from Carbon-iron Melts. Donetsk State Technical University 2000.

[36] European Financial Services. EU-27 Steel Scrap Specification 2007:9.

[37] Yang Y, Raipala K, Holappa L. Ironmaking. vol. 3. Elsevier Ltd.; 2014. https://doi.org/10.1016/B978-0-08-096988-6.00017-1.

[38] Sarna SK. Sulphur in Steels. Ispatguru 2014.

[39] Sims CE, Dahle FB. Effect of Aluminium on the Properties of Medium Carbon Cast Steel. American Foundry Society Transactions 1938.

[40] You D, Michelic SK, Wieser G, Bernhard C. Modelling of Manganese Sulfide Formation During the Solidification of Steel. Journal of Materials Science 2017;52:1797–812. https://doi.org/10.1007/s10853-016-0470-y.

[41] Wu M, Fang W, Chen RM, Jiang B, Wang HB, Liu YZ, et al. Mechanical Anisotropy and Local Ductility in Transverse Tensile Deformation in Hot Rolled Steels: The Role of MnS Inclusions. Materials Science and Engineering A 2019;744:324–34. https://doi.org/10.1016/j.msea.2018.12.026.

[42] Geerdes M, Toxopeus H, Vliet C van der. Modern Blast Furnace Ironmaking - An Introduction. IOS Press, Amsterdam 2009.

[43] Kawasaki Steel 21st Century Foundation, JFE 21st Century Foundation. An Introduction to Iron and Steel Processing 2003.

[44] E. T. Turkdogan. Fundamentals of Steel Making. 2010. https://doi.org/10.1017/CBO9781107415324.004.

[45] American Iron and Steel Institute. Technology Roadmap Research Program for the Steel Industry. 2010.

[46] Francis LF. Starting Materials. 2016. https://doi.org/10.1016/b978-0-12-385132-1.00002-1.

[47] Save GrafTech. Redefining the Board. 2014.

[48] Björkman B, Samuelsson C. Recycling of Steel. Handbook of Recycling 2014:65–83. https://doi.org/10.1016/B978-0-12-396459-5.00006-4.

[49] Li Y, Xu W, Zhu T, Qi F, Xu T, Wang Z. CO2 emissions from BF-BOF and EAF steelmaking based on Material Flow Analysis. Advanced Materials Research 2012;518–523:5012–5. https://doi.org/10.4028/www.scientific.net/AMR.518-523.5012.

[50] U.S. Environmental Protection Agency, National Center for Environmental Assessment. Coke oven emissions; CASRN NA. 2002.

[51] Mayyas M, Nekouei RK, Sahajwalla V. Valorization of Lignin Biomass as a Carbon Feedstock in Steel Industry: Iron Oxide Reduction, Steel Carburizing and Slag Foaming. Journal of Cleaner Production 2019;219:971–80. https://doi.org/10.1016/j.jclepro.2019.02.114.

[52] Khanna R, Li K, Wang Z, Sun M, Zhang J, Mukherjee PS. Biochars in Iron and Steel Industries. Elsevier Inc.; 2019. https://doi.org/10.1016/B978-0-12-814893-8.00011-0.

[53] Dankwah JR, Koshy P, O'Kane P, Sahajwalla V. Reduction of FeO in EAF Steelmaking Slag by Blends of Metallurgical Coke and End-of-life Tyre. Steel Research International 2012;83:766–74. https://doi.org/10.1002/srin.201200019.

[54] Devasahayam S, Bhaskar Raju G, Mustansar Hussain C. Utilization and Recycling of End of Life Plastics for Sustainable and Clean Industrial Processes Including the Iron and Steel Industry. Materials Science for Energy Technologies 2019;2:634–46. https://doi.org/10.1016/j.mset.2019.08.002.

[55] Kushnir D, Hansen T, Vogl V, Åhman M. Adopting Hydrogen Direct Reduction for the Swedish Steel Industry: A technological Innovation System (TIS) Study. Journal of Cleaner Production 2019;242:118–85. https://doi.org/10.1016/j.jclepro.2019.118185.

[56] Samarasekera I v. Encyclopedia of Materials: Science and Technology (Second Edition). 2001.

[57] Spuzic S, Strafford KN, Subramanian C, Savage G. Wear of Hot Rolling Mill rolls: an Overview. WEAR 1994;176:261–71. https://doi.org/10.1016/0043-1648(94)90155-4.

[58] Osadchii VYa, Getiya IG, Levshunov MA, Frolochkin V v., Biryukov VT, Moglievkin FD, et al. Roll Pass Design and Wear of Mandrrels of Piercing Mills with Mushroomshped Rolls. Metallurgy All-Union Correspondence Mechanical Engineering Institute 1971:320–2.

[59] Pooyutovskii Yu, Getiya IG, Kolesnikov YaE, Rezinskov SA, Ermakov V v., Borisenko GS, et al. Roll Pass Design and Wear of the Work Rolls of The Piercing Mill of the Pilger Rolling Mill. Metallurgy All-Union Correspondence Mechanical Engineering Institute 1975:617–9.

[60] Steinboeck RA, Kugi A. Steering Control of Metal Strips using a Pivoted Guide. International Federation of Automatic Control 2015;28:137–42. https://doi.org/10.1016/j.ifacol.2015.10.092.

[61] Mackenzie DS, Lambert D. Effect of Quenching Variables on Distortion and Residual Stresses. 2003.

[62] Jacolot R, Huin D, Marmulev A, Mathey E. Hot Rolled Coil Property Heterogeneities due to Coil Cooling: Impact and Prediction. Key Engineering Materials 2014;622–623:919–28. https://doi.org/10.4028/www.scientific.net/KEM.622-623.919.

[63] Buessler P, Maugis P, Bouaziz O, Schmitt JH. Integrated Process-Metallurgy Modelling: Example of Precipitation During Coil Cooling. Iron and Steelmaker (I and SM) 2003;30:33–9.

[64] Park S-J, Hong B-H, Baik SC, OH KH. Finite Element Analysis of Hot Rolled Coil Cooling. Iron and Steel Institute of Japan International 1998;38:1262–9.

[65] Li H, Li T, Li C, Wang Z, Wang G. Improvement of Longitudinal Performance Uniformity of Hot-Rolled Coils for Cold-rolled DP980 Steel. MDPI Metals 2020;10. https://doi.org/10.3390/met10030382.

[66] Chashchin V v., Popov ES, Kuklev A v., Toropov SS, Kapitanov VA, Manyurov SB. Improving the Controlled Cooling of Hot-rolled Steel Coils. Steel in Translation 2010;40:839–43. https://doi.org/10.3103/S0967091210090160.

[67] Chashchin V v. Controlled Cooling of Coils of High-carbon and Alloy Structural Steel. Steel in Translation 2010;40:153–6. https://doi.org/10.3103/S0967091210020129.

[68] Patel JK, Wilshire B. The Challenge to Produce Consistent Mechanical Properties in Nb-HSLA Strip Steels. Journal of Materials Processing Technology 2002;120:316–21. https://doi.org/10.1016/S0924-0136(01)01130-X.

[69] Chashchin VV, Toropov SS, Popov ES. Method of Outer Surface Heat Insulation of Black Strip Roll and Facility for its Realisation. 2345858, 2009.

[70] Oxford Instruments. Aztec 4.2 User Manual. 2019.

[71] Bruker. Quantax EBSD 2019.

[72] Markforged. H13 Tool Steel. 2018.

[73] Weber R, Manning K, White M. College Physics. 4th ed. The pennsylvania State university; 1965.